POLARIMETRIC MICROWAVE RADIOMETER CALIBRATION

by

Jinzheng Peng

A dissertation submitted in partial fulfillment
of the requirements for the degree of
Doctor of Philosophy
(Electrical Engineering)
in the University of Michigan
2008

Doctoral Committee:

Professor Christopher S. Ruf , Chair
Professor Anthony W. England
Professor Jeffrey A. Fessler
Associate Professor Mahta Moghaddam
Jeffrey R. Piepmeier, NASA/GSFC

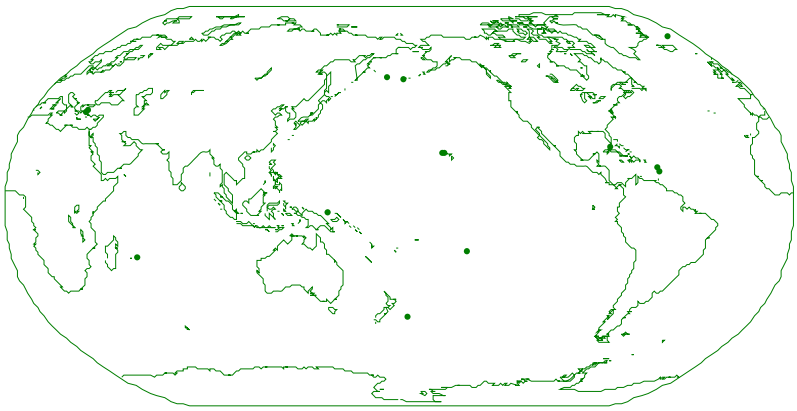

© Jinzheng Peng
All Rights Reserved
2008

Dedication

To my parents for their support and teaching,
my wife for her endurance and love,
and my daughter, Zixi.

Acknowledgements

First and foremost, I am indebted to my dissertation committee for their help and advice throughout this process. My gratitude is especially focused on my advisor, Dr. Christopher Ruf, who has steadfastly supported me during the course of this work in both financial and academic terms.

I would also like to express my sincere appreciation and affection to my friends and colleagues in the Remote Sensing Group for their friendship and support over the past years: Dr. Roger De Roo, Boon Lim, Sid Misra, Ying Hu, Hirofumi Kawakubo, John Puckett, Amanda Mims, Steven Gross, David Boprie and Bruce Block. I have shared with you enlightening discussions, gratifying experiments, and we have had many great times together.

Most importantly, I wish to express my deepest gratitude to my family. Your support, love, and faith alone kept me going in the hard times. A portion of this degree should be conferred to you. I can never adequately express my love and thanks for all your support.

Table of Contents

List of Figures

List of Tables

List of Appendices

Abstract

A polarimetric radiometer is a radiometer with the capability to measure the correlation information between vertically and horizontally polarized electric fields. To better understand and calibrate this type of radiometer, several research efforts have been undertaken.

1) All microwave radiometer measurements of brightness temperature (T_B) include an additive noise component. The variance and correlation statistics of the additive noise component of fully polarimetric radiometer measurements are derived from theoretical considerations and the resulting relationships are verified experimentally. It is found that the noise can be correlated among polarimetric channels and that the correlation statistics can vary as a function of the polarization state of the scene under observation.

2) A polarimetric radiometer calibration algorithm has been developed which makes use of the Correlated Noise Calibration Standard (CNCS) to aid in the characterization of microwave polarimetric radiometers and to characterize the non-ideal characteristics of the CNCS itself simultaneously. CNCS has been developed by the Space Physics Research Laboratory of the University of Michigan (SPRL). The calibration algorithm has been verified using the DetMit L-band radiometer. The

precision of the calibration is estimated by Monte Carlo simulations. A CNCS forward model has been developed to describe the non-ideal characteristics of the CNCS. Impedance-mismatches between the CNCS and radiometer under test are also considered in the calibration.

3) The calibration technique is demonstrated by applying it to the Engineering Model (EM) of the NASA Aquarius radiometer. CNCS is used to calibrate the Aquarius radiometer – specifically to retrieve its channel phase imbalance and the thermal emission characteristics of transmission line between its antenna and receiver. The impact of errors in calibration of the radiometer channel phase imbalance on Sea Surface Salinity (SSS) retrievals by Aquarius is also analyzed.

4) The CNCS has also been used to calibrate the Breadboard Model (BM) of the L-band NASA Juno radiometer. In order to cover the broad TB dynamic range of the Juno radiometer, a special linearization process has been developed for the CNCS. The method combines multiple Arbitrary Waveform Generator gaussian noise signals with different values of variance to construct the necessary range of TB levels. The resulting CNCS output signal can simulate the expected TB profile for Juno while in orbit around Jupiter, in particular simulating the strong synchrotron emission signal.

Chapter 1

Introduction

1.1 Microwave Remote Sensing Overview

Remote sensing is the science and technology of acquiring information about a target (the earth surface, atmosphere, etc.) of interest without physical or intimate contact with it. This is done by using a sensor to gather reflected or emitted energy/radiation and processing, analyzing, and applying that information to an object that is otherwise inaccessible. It can provide important coverage, mapping and classification of the targets in a fast and cost-efficient manner.

Remote sensing can be subdivided into 2 basic types—active and passive—depending on if the sensor carries the energy source for illumination. The active remote sensing sensor emits radiation which is directed toward the target to be investigated, and detects the radiation scattered from the target. It has the ability to take measurements anytime, but a fairly large amount of energy is required to sufficiently illuminate targets. This is its main disadvantage especially for space-borne sensors. The passive remote sensing sensor, on the other hand, doesn't use an illumination source and measures energy that is naturally available. The energy is either emitted from or reflected by the target to be investigated, but the amount of energy must be large enough to be detected.

As a matter of convention, remote sensing can also be subdivided into visible/optical remote sensing, infrared remote sensing, microwave remote sensing, etc. by the spectrum of the energy that the sensor receives. The visible/optical region of the spectrum ranges from blue light with a wavelength of about 0.4 μm to red light with a wavelength of about 0.75 μm. Due to its very short wavelength, the spatial resolution of a visible/optical remote sensing sensor can be very high. One of its limitations is that even though visible radiation is able to propagate through a clean (cloudless, no dust, etc.) and dry atmosphere with very little attenuation, it will be significantly attenuated if the atmosphere is not clean and dry. A unique property of visible radiation is that it can penetrate water more deeply than infrared and microwave radiation. Due to these properties, visible/optical remote sensing focuses on missions such as air quality, clouds, aerosols, water vapor, marine ecology, etc.

In contrast to visible/optical radiation, infrared radiation can't be detected directly by the human eye, but is able to be detected photographically or electronically. The infrared regions of the spectrum of interest for remote sensing are the near-infrared region, with wavelength from about 0.75 μm to about 1.5 μm, and the thermal-infrared region, with wavelength from 3 μm to about 100 μm. Radiation in the near-infrared region for remote sensing purposes is very similar to radiation in the visible portion. However, radiation in the thermal-infrared region is quite different. It is emitted from the target in the form of heat. Due to this mechanism, thermal remote sensing can distinguish between different targets if their temperatures are different.

In contrast to the above two types of remote sensing, microwave remote sensing is of more recent interest. It uses reflected or emitted energy in the microwave region,

which ranges from about one millimeter to a few tens of centimeters, to identify, measure and analyze the characteristics of the target of interest in almost all weather conditions. For example, low frequency microwaves can penetrate clouds, which cover the earth ~70% of the time [1]. They can also penetrate rain to some extent, rain as well [2]. Microwave radiation is also independent of the sun as a source of illumination. In addition, lower frequency microwaves are able to penetrate significantly into the ground and vegetation [3]. Furthermore, microwave remote sensing can provide unique information such as wind speed and direction above the sea surface which is extracted from sea surface radiation, polarization, backscattering etc [4, 5]. These are advantages that are not possible with visible and/or infrared remote sensing.

All types of remote sensing systems include four basic components to extract information about the target of interest from a distance. These components are the energy source, the target, the transmission path and the sensor. For a passive microwave remote sensing system, which this work focuses on, the energy source is the target itself. Useful information is obtained from the radiation that is emitted by the target and received by the radiometer.

1.2 Electromagnetic Wave Radiation

1.2.1 Blackbody Radiation

Any object emits radiation at all possible frequency if its physical temperature is above zero Kelvin. For any given frequency, there is an upper bound on the intensity of radiation. The upper bound is reached only when the object is a blackbody, which is defined as a perfect radiation absorber, in which case it is also a perfect emitter according

Kirchhoff's law [3]. The upper bound on the radiated intensity is given by Planck's law as [6]

$$B_{bb,f} = \frac{2hf^3}{c^2\left(e^{\frac{hf}{kT_{phy}}} - 1\right)} \tag{1.2.1}$$

where $B_{bb,f}$: radiation intensity of a blackbody, $W \cdot m^{-2} \cdot sr^{-1} \cdot Hz^{-1}$

f: frequency, Hz

h: Planck's constant, 6.626×10^{-34} J

c: speed of light, 3×10^8 $m \cdot s^{-1}$

k: Boltzmann's constant, 1.381×10^{-23} $J \cdot K^{-1}$

T_{phy}: physical temperature of the blackbody, Kelvin.

In the microwave region, the wavelength is sufficiently long that $hf / kT_{phy} << 1$, in which case the Planck expression can be simplified to

$$B_{bb,f} = \frac{2f^2 kT_{phy}}{c^2} = \frac{2kT_{phy}}{\lambda^2} \tag{1.2.2}$$

where λ is wavelength. This is known as the Rayleigh-Jeans law or Rayleigh-Jeans approximation [3]. For a blackbody at a physical temperature of 300 K, the difference between the radiation intensity derived from Planck's expression and that from the Rayleigh-Jeans approximation is less than 1% provided the frequency is less than 117 GHz [3].

1.2.2 Graybody Emissivity

A blackbody is an idealized body which corresponds to the theoretical maximum possible radiation intensity from any real object. Real objects, which are usually referred

to as gray bodies, are not a blackbody and so have less radiation than a blackbody would at the same physical temperature. In addition, unlike a blackbody which radiates uniformly in all directions, their radiation in general depends on direction. The ratio of the radiation of a real object to that of a blackbody with the same physical temperature as the real object is defined as its emissivity $\varepsilon(\theta,\phi)$:

$$\varepsilon_f(\theta,\phi) = \frac{B_f(\theta,\phi)}{B_{bb,f}} \tag{1.2.3}$$

where θ and ϕ determine the angle of propagation of the radiation from the object.

The brightness temperature of an object is defined as

$$T_{B,f}(\theta,\phi) = \varepsilon_f(\theta,\phi) \cdot T_{phy} \tag{1.2.4}$$

The brightness temperature and emissivity are frequency dependent. For sufficiently narrow bandwidth radiation, the emissivity and brightness temperature can be regarded as constant over the bandwidth, so that the subscript f can be ignored.

Since the radiation from a real object is always less that or equal to that from a blackbody with equal physical temperature, the emissivity is never greater than 1. Thus, the brightness temperature $T_B(\theta,\phi)$ of a object is always less than or equal to its physical temperature T_{phy}.

The brightness temperature, T_B, associated with a propagating electromagnetic wave is related to its electric field strength, $E(t)$, by

$$T_B = \frac{\lambda^2}{k\eta B}\left\langle |E(t)|^2 \right\rangle \tag{1.2.5}$$

where η : intrinsic impedance of the electromagnetic wave, in ohms;

λ: wavelength of the electromagnetic wave, in m;

B: bandwidth of the electromagnetic wave, in Hz

$\langle\cdot\rangle$: denote 'statistical expectation or time average'.

1.2.3 Polarization

Polarization is a property of a transverse electromagnetic wave which describes the shape and locus of the tip of the electric field vector $\overline{E}$ (in the plane perpendicular to the wave's direction of travel) at a fixed point in space as a function of time. A transverse plane wave traveling in the r direction can be decomposed into θ- and ϕ-components (or a vertically polarized component, v, and a horizontally polarized component, h) in the spherical coordinate system described by Figure 1.1 and can be written as

$$\overline{E}(r) = \left(\hat{v}E_v + \hat{h}E_h\right)e^{-jk_r r} \tag{1.2.6}$$

where E_v and E_h are defined as

$$E_v = E_{v0}e^{j\varphi_v} \tag{1.2.7a}$$

$$E_h = E_{h0}e^{j\varphi_h} \tag{1.2.7b}$$

Assuming $\varphi = \varphi_v - \varphi_h$, Equation (1.2.6) can be written as

$$\overline{E}(r) = \left(\hat{v}E_{v0}e^{j\varphi} + \hat{h}E_{h0}\right)e^{j\varphi_h}e^{-jk_r r} \tag{1.2.8}$$

and

$$\begin{aligned}\overline{E}(r,t) &= \mathrm{Re}\left\{\left(\hat{v}E_{v0}e^{j\varphi} + \hat{h}E_{h0}\right)e^{j\varphi_h}e^{-jk_r r}e^{j\omega t}\right\} \\ &= \hat{v}E_{v0}\cos\left(\omega t - k_r r + \varphi_h + \varphi\right) + \hat{h}E_{h0}\cos\left(\omega t - k_r r + \varphi_h\right)\end{aligned} \tag{1.2.9}$$

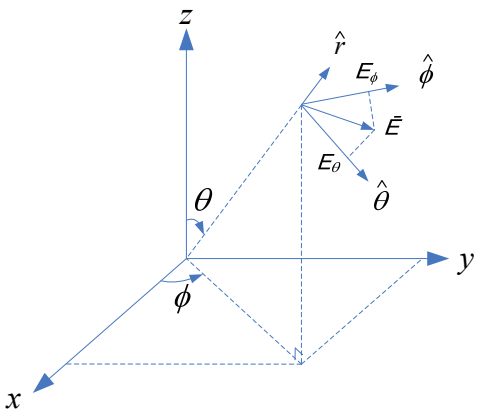

Figure 1.1 The electric field $\bar{E}$ in the spherical coordinate system and the rectangular coordinate system. E_θ and E_ϕ are its θ- and ϕ-components in the spherical coordinate system respectively. The unit vectors $\hat{r}$, $\hat{\theta}$ and $\hat{\phi}$ are perpendicular to each other and they satisfy the relation $\hat{r} = \hat{\theta} \times \hat{\phi}$

The general expression reduces to several special cases of interest.

Case I: $E_{v0} = 0$ (or $E_{h0} = 0$)

This is known as a linearly polarized wave and its electric field vector moves along the θ- or ϕ- axis. It is referred to as a vertically or horizontally polarized wave.

Case II: $E_{v0} = E_{h0}$ and $\varphi = 0^\circ$ (or 180°)

$$\bar{E}(z) = \left(\hat{v} + \hat{h}\right) E_{v0} e^{j\varphi_h} e^{-jk_r r} \tag{1.2.10a}$$

or

$$\bar{E}(z) = \left(-\hat{v} + \hat{h}\right) E_{v0} e^{j\varphi_h} e^{-jk_r r} \tag{1.2.10b}$$

This is also a linearly polarized wave, but its electric field vector moves at 45 degrees with respect to the θ-axis. It is referred to as a +45° or -45° slant linearly polarized wave.

Case III: $E_{v0} = E_{h0}$ and $\varphi = 90^\circ$ (or -90°)

$$\overline{E}(z) = \left(j\hat{v} + \hat{h}\right)E_{v0}e^{j\varphi_h}e^{-jk_r r} \tag{1.2.11a}$$

or

$$\overline{E}(z) = \left(-j\hat{v} + \hat{h}\right)E_{v0}e^{j\varphi_h}e^{-jk_r r} \tag{1.2.11b}$$

In this case the trace of the electric field vector is a circle and the wave is defined to be right- or left-hand circularly polarized.

$$\begin{aligned}\overline{E}(r,t) &= \mathrm{Re}\left\{\left(\hat{v}E_{v0}e^{j\varphi} + \hat{h}E_{h0}\right)e^{j\varphi_h}e^{-jk_r r}e^{j\omega t}\right\} \\ &= \hat{v}E_{v0}\cos\left(\omega t - k_r r + \varphi_h + \varphi\right) + \hat{h}E_{h0}\cos\left(\omega t - k_r r + \varphi_h\right)\end{aligned} \tag{1.2.12}$$

Any polarization state can be decomposed into its vertically and horizontally polarized components, so it is convenient to consider each of the components independently.

When a wave propagates from one medium to another with different dielectric properties, a part of it gets reflected by the boundary and another part gets transmitted across the boundary into the other medium, as described by Figure 1.2 and Figure 1.3. The reflectivity for vertically and horizontally polarized waves is given by [7]

$$\Gamma_h = \left|\frac{\eta_2\cos\theta_1 - \eta_1\cos\theta_2}{\eta_2\cos\theta_1 + \eta_1\cos\theta_2}\right|^2 \tag{1.2.13a}$$

$$\Gamma_v = \left|\frac{\eta_1\cos\theta_1 - \eta_2\cos\theta_2}{\eta_1\cos\theta_1 + \eta_2\cos\theta_2}\right|^2 \tag{1.2.13b}$$

where $\eta_x = \sqrt{\mu_x / \varepsilon_x}$: the intrinsic impedance of medium x = 1 or 2;

θ_1: the angle of incidence;

θ_2: the angle of transmission;

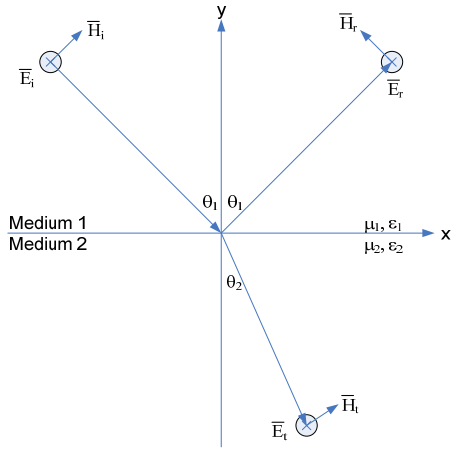

Figure 1.2 Reflection and transmission of horizontally polarized waves at a plane boundary

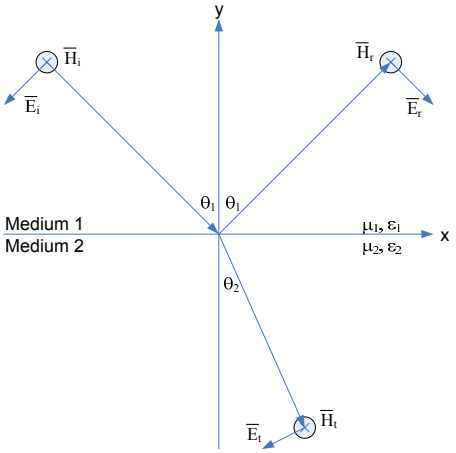

Figure 1.3 Reflection and transmission of vertically polarized waves at a plane boundary

The angle of incidence, θ_1, and the angle of transmission, θ_2, satisfy Snell's law [8], or

$$k_1 \sin\theta_1 = k_2 \sin\theta_2 \tag{1.2.14}$$

where $k_x = \omega\sqrt{\mu_x \varepsilon_x}$ is the spatial frequency of medium $x = 1$ or 2.

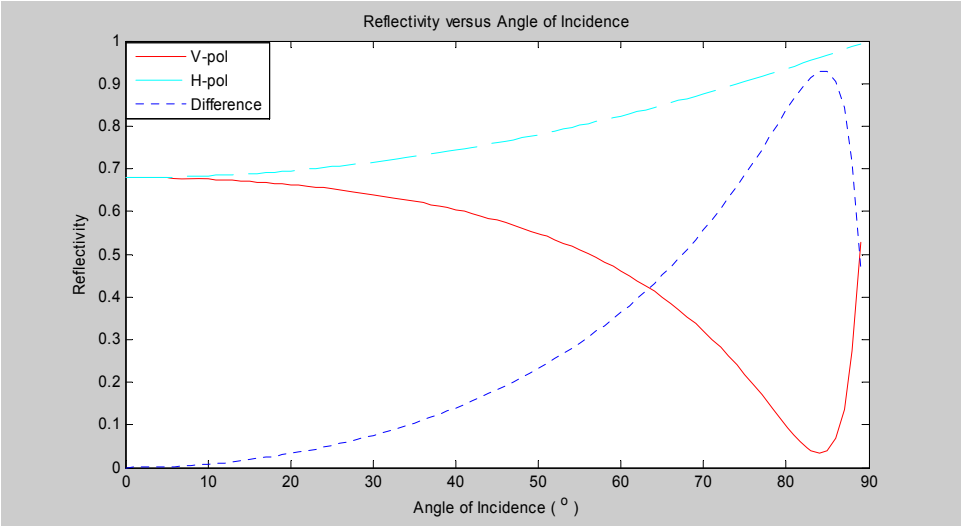

Figure 1.4 Reflectivity of the sea surface with $\varepsilon_r = 70.8 - j62.3$

The reflectivity of the two linearly polarized waves is in general different. Figure 1.4 shows their reflectivity versus the angle of incidence (or radiation angle) for sea water with dielectric constant $\varepsilon_r = 70.8 - j62.3$. This dielectric constant is obtained by using the Stogryn ocean dielectric model [9] with frequency = 1.413 GHz, sea surface temperature = 20°C and sea surface salinity = 32.54 psu. A specular surface [3] is assumed. It can be observed that the reflectivity of the vertically polarized signal increases as the angle of incidence increases up to 80°; whereas the reflectivity of the horizontally polarized signal has the opposite tendency. The difference between the reflectivity of the vertically and horizontally polarized signals increases as the angle of incidence increases up to 80°. This clearly shows that the reflectivity is polarization dependent.

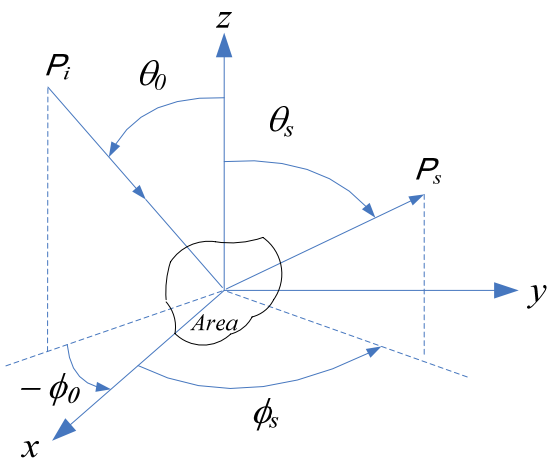

Figure 1.5 Geometry of incident and scattered radiation

The reflectivity at a boundary is closely related to the emissivity of a medium. A rough surface can be characterized by the bistatic scattering cross-section per unit area σ°. Peake developed an expression for the polarized emissivity of a surface observed from the direction (θ_0, ϕ_0) shown in Figure 1.5 in terms of σ° [10]:

$$\varepsilon(\theta_0,\phi_0;p_0)=1-\frac{1}{4\pi\cos\theta_0}\int\left[\sigma^0(\theta_0,\phi_0;\theta_s,\phi_s;p_0,p_0)+\sigma^0(\theta_0,\phi_0;\theta_s,\phi_s;p_0,p_s)\right]d\Omega_s \tag{1.2.15}$$

where (θ_0, ϕ_0): the direction from which the wave is incident upon the surface;

(θ_s, ϕ_s): the direction in which the wave is scattered;

p_s or p_o: v or h denote vertical or horizontal polarization.

In Equation (1.2.15), $\sigma^0(\theta_0,\phi_0;\theta_s,\phi_s;p_0,p_s)$ relates the magnitude of the power scattered in the direction (θ_s, ϕ_s) with polarization p_s to the power incident upon the surface from the direction (θ_0, ϕ_0) with polarization p_o. If p_s and p_o are the same, σ° is called the vertically or horizontally polarized scattering coefficient, respectively, and if

they are different, it is known as the cross-polarized scattering coefficient. For a specular surface, the cross-polarized scattering coefficient is zero, while the like-polarized scattering coefficient is nonzero only in the specular direction. In this case, the emissivity of the specular surface is given by

$$\varepsilon(\theta, p) = 1 - \Gamma(\theta, p) \tag{1.2.16}$$

where p (=v, h) stands for its polarization state. For this reason, the emissivity is also polarization dependent.

1.2.4 Stokes parameters

In general, a polarized wave has an elliptical polarization state that is commonly described with the Poincaré sphere in terms of its total intensity, ellipticity and orientation angle [8]. To facilitate the discussion of the polarization state of an electromagnetic wave, the Stokes parameters —a set of 4 values (I, Q, U, V)— were introduced as a mathematically convenient alternative by Sir George Stokes [11]. These four parameters are related to the horizontally and vertically polarized components of electric field by

$$\begin{bmatrix} I \\ Q \\ U \\ V \end{bmatrix} = \frac{1}{\eta} \begin{bmatrix} \left\langle |E_v|^2 \right\rangle + \left\langle |E_h|^2 \right\rangle \\ \left\langle |E_v|^2 \right\rangle - \left\langle |E_h|^2 \right\rangle \\ 2\,\mathrm{Re}\left\langle E_v E_h^* \right\rangle \\ 2\,\mathrm{Im}\left\langle E_v E_h^* \right\rangle \end{bmatrix} \tag{1.2.17}$$

where E_v: the vertically polarized component of electric field

E_h: the horizontally polarized component of electric field

The units of the Stokes parameters are W/m^2. The first Stokes parameter (I) gives the total radiation power density, and the second Stokes parameter (Q) represents the power density difference between the two linearly polarized components. The third and

fourth Stokes parameters (U and V) describe the correlation between these two components.

For microwave remote sensing, modified Stokes parameters are often used. Under the Rayleigh-Jeans approximation, the modified Stokes parameters in brightness temperature are given by [12]

$$\begin{pmatrix} T_v \\ T_h \\ T_3 \\ T_4 \end{pmatrix} = \frac{\lambda^2}{k\eta B} \begin{pmatrix} \left\langle |E_v|^2 \right\rangle \\ \left\langle |E_h|^2 \right\rangle \\ 2\,\mathrm{Re}\left\langle E_v E_h^* \right\rangle \\ 2\,\mathrm{Im}\left\langle E_v E_h^* \right\rangle \end{pmatrix} \tag{1.2.18}$$

where T_v, T_h, T_3 and T_4 are, respectively, the vertically and horizontally polarized and the third and fourth Stokes parameters.

It is convenient and useful to describe the radiation of an object, for example radiation from a windy ocean surface, using the modified Stokes parameters. The ocean surface emissivity (or brightness temperature) is not only polarization dependent, but also wind speed and direction dependent. Increasing wind speed will increase the foam coverage on the sea surface, thus substantially increasing the sea surface emissivity [13, 14]. Previous ocean surface emission models and experiments have determined that the vertical and horizontal ocean surface emissivity is an even function of the relative wind direction while the 3rd and 4th Stokes emissivity is an odd function of the relative wind direction [15-18]. The 3rd Stokes parameter from the ocean surface can be as high as 2 Kelvin at 10.7 GHz, as measured by the WindSat spaceborne radiometer [5].

1.3 Electromagnetic Wave Propagation through the Atmosphere

The earth's atmosphere is composed of about 78% nitrogen, 21% oxygen, 1% argon, traces of other gases and a variable amount of water vapor. Among these components, oxygen and water vapor play the most important role in microwave remote sensing. The density of oxygen decreases almost exactly exponentially with increasing height. In contrast, water vapor density variations with height tend to be much more irregular and are strongly dependent on time of day, season, geographic location and atmospheric activity.

When an electromagnetic wave propagates through the earth atmosphere, it is absorbed and scattered by the atmosphere. At the same time, the atmosphere emits energy which will become part of the energy received by a remote sensing sensor. The degree of absorption and emission by the atmosphere depends on multiple factors including frequency, geographic location, etc.

Another effect of the atmosphere on a propagating EM wave is that it will change the polarization state of the EM wave when it propagates through the ionosphere. The ionosphere is the uppermost part of the atmosphere, beginning at about 80 kilometers, as shown in Figure 1.6. The ionosphere is full of charged particles. Under the effect of the earth magnetic field, propagating linearly polarized field components are rotated by an angle Ω due to Faraday rotation [19]

$$\Omega = 1.355 \times 10^4 f^{-2} N_f \langle B_0 \cos\alpha \sec\chi \rangle \tag{1.3.1}$$

where Ω is in degrees

f: EM wave frequency, GHz;

N_f: ionospheric total electron content (TEC) in TEC units, or 10^{16} electrons/m^2;

B_0: earth magnetic field, Tesla;

α: angle between the magnetic field and wave propagation direction;

χ: angle between the wave propagation direction and the vertical to the surface.

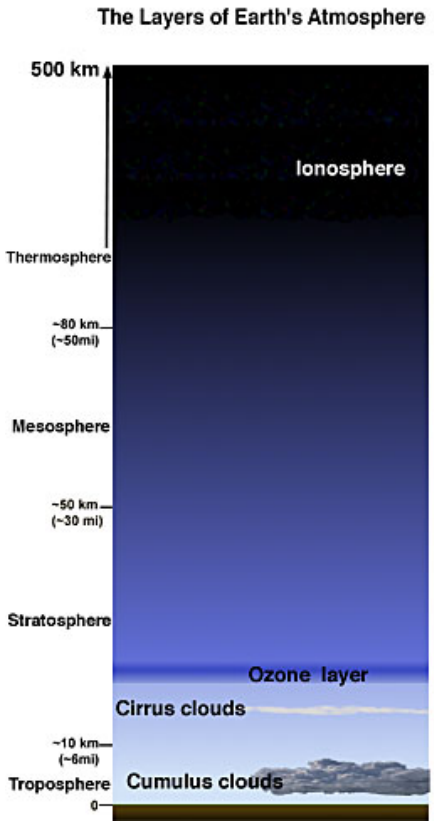

Figure 1.6 The layers of the earth's atmosphere [20]

Without considering the attenuation and emission of the ionosphere, the resulting Stokes parameters will become [19]

$$\begin{pmatrix} T_v' \\ T_h' \\ T_3' \\ T_4' \end{pmatrix} = \begin{pmatrix} T_v - \Delta T_B \\ T_h + \Delta T_B \\ -(T_v - T_h)\sin 2\Omega + T_3 \cos 2\Omega \\ T_4 \end{pmatrix} \tag{1.3.2}$$

where

$$\Delta T_B = (T_v - T_h)\sin^2\Omega - \frac{T_3}{2}\sin 2\Omega \qquad (1.3.3)$$

1.4 Real Aperture Radiometer

A radiometer is a device used to measure the radiant power of electromagnetic radiation. For a microwave radiometer, it usually consist of an antenna and a receiver, as shown schematically below

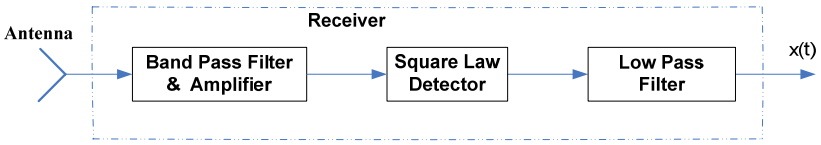

Figure 1.7 Radiometer block diagram

An antenna may be defined as a transducer between a guided wave propagating in a transmission line and an electromagnetic wave propagating in an unbounded medium (usually free space), or vice verse [7]. A microwave radiometer antenna receives electromagnetic energy in the microwave range radiated by the object under observation, and then sends it to the receiver. The strength of the signal at the receiver input port is very weak and is typically at or below the level of the receiver thermal noise. To detect the strength of the received signal, high gain amplification is required after the bandpass filter which is used to select the desired observation signal band. A square-law detector is followed to extract the strength of the signal and a low-pass filter is used to filter out the high frequency components. The bandwidth of the low-pass filter determines the integration time of the measurement. The DC component of the output from the low pass filter is proportional to the antenna brightness according to

$$\begin{aligned} V_0 &= g\left(T'_A + T_R\right) \\ &= g\left\{\xi T_A + \left(1-\xi\right)T_{A,phy} + T_R\right\} \end{aligned} \tag{1.4.1}$$

where g: Gain of the receiver

T'_A: antenna temperature at antenna termination;

T_A: antenna radiometric temperature;

ξ: antenna radiation efficiency;

$T_{A,phy}$: physical temperature of the antenna;

T_R: receiver equivalent noise temperature.

With a well-calibrated radiometer, the strength of the signal received by the radiometer antenna can be determined and the antenna radiometric temperature can be recovered from the raw measurement according to

$$T_A = \frac{V_0}{\xi g} - \frac{\left(1-\xi\right)T_{A,phy} + T_R}{\xi} \tag{1.4.2}$$

For this kind of radiometer, the precision of the measurement is given by [21]

$$\Delta T = \frac{T_{sys}}{\sqrt{Bt}} = \frac{T'_A + T_R}{\sqrt{Bt}} \tag{1.4.3}$$

where T'_A: antenna temperature;

T_{sys}: equivalent system noise temperature of the receiver;

B: receiver bandwidth;

t: integration time of the radiometer.

The square-law detector and low pass filter in Figure 1.7 can be replaced with a digital self-correlation (sample, square and accumulate) operation. The sampling can be made at the RF band directly [22-24], or at the IF band with an additional mixer and local oscillator in the receiver.

Early microwave radiometers were usually total power designs used to detect the radiation power, such as the SMMR radiometer [25] which was the first modern earth science microwave radiometer in space. It measured dual-polarized microwave radiation from the earth's atmosphere and surface at 5 frequency bands. At each frequency band, the 2 polarized channels are used to measure the emission strength at *v*- and *h*-polarization individually. The receivers estimate the variance of the signal by performing a time average of the square of the signal. The two resulting components of T_B are designated T_v and T_h for vertical and horizontal polarization, respectively. This kind of radiometer is usually called a dual-polarimetric radiometer and consists of 2 total power radiometers.

Beyond the total power radiometer which just measures the received signal strength, there are 3 kinds of correlation radiometers: auto-correlation, interferometric and polarimetric. An auto-correlation radiometer measures the correlation between a signal and a time delayed version of itself, or autocorrelation. The autocorrelation function of a given signal *s(t)* is defined as

$$R(\tau) = \int_{-\infty}^{+\infty} s(t)s^*(t-\tau)dt \tag{1.4.4}$$

where * denotes the complex conjugate and τ is time separation.

The Fourier Transform of the autocorrelation function is the power spectrum, so an auto-correlation radiometer can measure brightness temperature spectrum within the receiving bandwidth [26]. A total power radiometer can be regarded as the special case of an auto-correlation radiometer with time separation τ=0. Both the interferometric and polarimetric radiometers are cross-correlation radiometers which measure the correlation between signals in 2 different channels. Their receivers have the same structure, while

their antennas are different. For an interferometric radiometer, two spatially separated but otherwise identical antennas are used to receive signals with the same polarization. On the other hand, a polarimetric radiometer can detect signals with different polarizations (vertical, horizontal, ±45° slant linear, and circular polarization) with only one antenna in general. But it could have multiple antennas, such as WindSat which has 3 antennas/feeds at each of the frequency bands 10.7, 18.7 and 37 GHz [27]: one antenna to receive *v*- and *h*-polarization signals; one antenna to receive the ±45° slant linear polarization signals; and the third antenna to receive the left- and right-hand polarization signals.

A fully polarimetric radiometer measures the strength and polarization state of thermally radiated electric fields, as described by the modified Stokes parameters. The third and fourth Stokes parameters characterize the correlation between the vertically and horizontally polarized electric field components, and can be used to retrieve other geophysical quantities than a conventional dual-polarimetric radiometer can, such as ocean wind direction [18] and Faraday rotation [19].

With only one antenna present, there are two common types of fully polarimetric radiometers which have been used to measure all four Stokes parameters, based on either coherent or incoherent detection [28]. A coherent detection radiometer measures the complex covariance of the vertical and horizontal polarization components of the signal directly [29]. The covariance can be measured by an analog complex-multiplier or by digitizing the vertical and horizontal polarization components of the signal and then multiplying and averaging (*i.e.* correlating) them in a digital signal processor if digital-correlation technology is used. The resulting components of T_B are designated T_3 and T_4 for the real and imaginary components of correlation, respectively. In comparison to a

coherent detection radiometer, an incoherent detection radiometer measures the variance of certain polarimetric components of the signal — most often the $\pm 45^{o}$ slant linear and left and right hand circular polarizations — in addition to the vertical and horizontal polarizations. The additional components of T_B are designated T_P, T_M, T_L and T_R for $+45^{o}$ and -45^{o} slant linear and left and right hand circular polarization, respectively. The variance, and hence the T_B, of each component can be estimated using the same squaring and time averaging signal processing steps as are used in the non-polarimetric case. The additional polarization components of the thermal emission signal can be generated in a number of ways. The most common approach uses hybrid combiners which add together the vertically and horizontally polarized components with relative phase differences of 0^{o}, $\pm 90^{o}$, and 180^{o} [16, 30, 31].

If the vertically and horizontally polarized components of the electric field radiated by thermal emission are designated as E_v and E_h, respectively, then the polarimetric components of T_B can be expressed as

$$T_v = c\left\langle |\, E_v \,|^2 \right\rangle \quad \text{and} \quad T_h = c\left\langle |\, E_h \,|^2 \right\rangle \tag{1.4.5a}$$

$$T_P = c\left\langle |\, \frac{E_v + E_h}{\sqrt{2}} \,|^2 \right\rangle \quad \text{and} \quad T_M = c\left\langle |\, \frac{E_v - E_h}{\sqrt{2}} \,|^2 \right\rangle \tag{1.4.5b}$$

$$T_L = c\left\langle |\, \frac{E_h - jE_v}{\sqrt{2}} \,|^2 \right\rangle \quad \text{and} \quad T_R = c\left\langle |\, \frac{E_h + jE_v}{\sqrt{2}} \,|^2 \right\rangle \tag{1.4.5c}$$

$$T_3 = 2c\,\mathrm{Re}\left\{\left\langle |\, E_v E_h^{*} \,| \right\rangle\right\} \quad \text{and} \quad T_4 = 2c\,\mathrm{Im}\left\{\left\langle |\, E_v E_h^{*} \,| \right\rangle\right\} \tag{1.4.5d}$$

where T_P, T_M, T_L and T_R correspond to $+45^{o}$ and -45^{o} slant linear and left and right hand circular polarization, respectively. Relationships between the various components follow from Equation (1.4.5) as [28, 29]

$$T_P = \frac{T_v + T_h + T_3}{2} \quad \text{and} \quad T_M = \frac{T_v + T_h - T_3}{2} \tag{1.4.6a}$$

$$T_L = \frac{T_v + T_h + T_4}{2} \quad \text{and} \quad T_R = \frac{T_v + T_h - T_4}{2} \tag{1.4.6b}$$

$$T_3 = T_P - T_M \quad \text{or} \quad T_3 = 2T_P - T_v - T_h \quad \text{or} \quad T_3 = T_v + T_h - 2T_M \tag{1.4.6c}$$

$$T_4 = T_L - T_R \quad \text{or} \quad T_4 = 2T_L - T_v - T_h \quad \text{or} \quad T_4 = T_v + T_h - 2T_R \tag{1.4.6d}$$

Here, a spherical coordinate system is assumed. If a rectangular coordinate system is used, the expression for T_4 will be different [28]. See Appendix 1 for a detailed derivation.

Equations (1.4.6c) and (1.4.6d) together represent the algorithms by which the 3rd and 4th Stokes parameters are typically derived with an incoherent detection fully polarimetric radiometer. Note that, in each case, there are three options to choose from. The second and third options require one less receiver to implement than the first one and so would seem to be the more cost effective approaches. However, in practice the first option is used almost exclusively because it is much better able to reject common mode calibration biases that are present in the incoherent detection channels. The other two options might be used as backup approaches in case of a radiometer hardware failure. The performance of the three options is evaluated and compared below.

The T_B of the signal received by a microwave radiometer is usually lower than 323 Kelvin because most microwave radiometers are for observing the earth and the physical temperature of the earth and atmosphere is lower than 50°C. The microwave radiometer is designed to be linear over its dynamic range, with a low boundary of 2.7 Kelvin usually. For planetary remote sensing, the input brightness temperature might be as high as 20,000 Kelvin. In this case, the linearity of the radiometer becomes an

important issue if the received signal is to be accurately measured over its full dynamic range.

1.5 Error in the Measurement

A microwave radiometer measurement of brightness temperature is an estimate of the variance of a random thermal emission signal collected by the radiometer antenna. During propagation, the emission signal is contaminated by other sources including the radiometer itself. The uncertainty of these non-target sources will cause measurement error.

To meet the accuracy requirements of most remote sensing experiments, a thorough understanding of the measurement error sources is required, and the effects caused by them need to be studied. For the Aquarius space-borne SSS mission, the error sources in general include measurement sensitivity, sea surface roughness and temperature, earth atmosphere attenuation and emission, Faraday rotation, solar and galactic radiation, non-ideal radiometer antenna, non-linearity of the radiometer receiver, and receiver gain variation. Some of the error sources, such as the radiometer antenna and receiver, are stable and their effects can be calibrated out. Some error sources are inherent, such as the measurement sensitivity. Most of the error sources are variable functions of time.

1) *Measurement Sensitivity*

The sensitivity of T_B to SSS is a function of frequency, polarization and incident angle. Higher sensitivity will result in higher precision for a given level of measurement noise. In general, vertically polarized T_B is more sensitive to SSS than horizontally

polarized T_B, and sensitivity increases with increasing incidence angle from 0° to 60° for vertical polarization while it decreases for horizontal polarization. The ocean surface emissivity using the Klein-Swift dielectric constant model (KS model) [32] vs. both SSS and incidence angle for each polarization is shown in Figure 1.8.

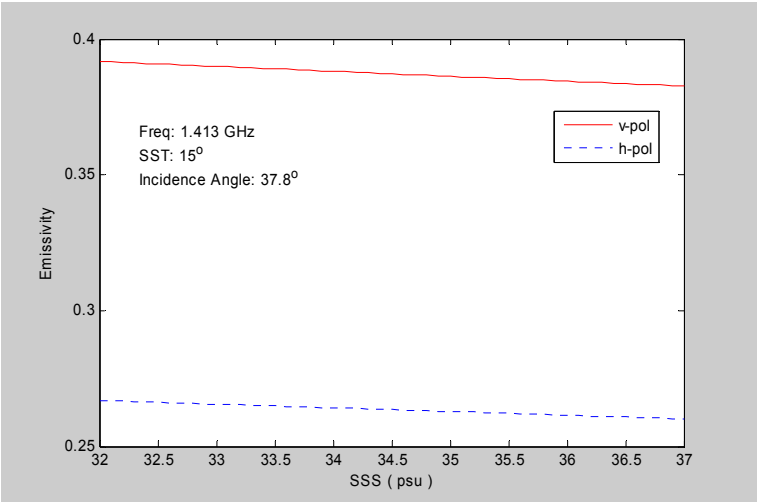

(a)

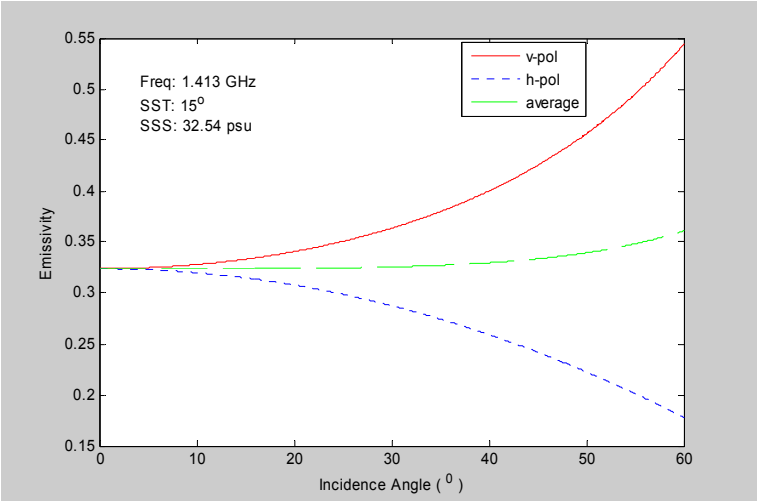

(b)

Figure 1.8 Ocean surface emissivity for *v*- & *h*-polarization. (a) Emissivity vs. SSS. (b) Emissivity vs. incidence angle

The effect of the salinity on thermal emission is higher at lower frequency and becomes negligible at frequencies above 4 GHz [33]. This is why a low frequency is used for the current Aquarius mission. But lower frequencies are affected more by Faraday rotation. These properties need to be weighed against one another when selecting a suitable observing frequency.

2) *Sea Surface Roughness*

Sea surface roughness is induced by near surface wind speed. With increasing wind speed, the roughness of the sea surface increases and finally the sea surface becomes a Lambertian surface [3]. Foam is a co-product of the wind. When wind is blowing over the sea surface, foam is produced and its fractional coverage of the surface increases with wind speed.

Because foam consists of part water and part air, it has dielectric properties intermediate between them and it can be regarded as an "impedance matching transformer" between sea water and the air. The emission from the foam-covered sea surface is stronger than that from a foam-free sea surface.

Experimental evidence shows that sea surface brightness temperature increases by a few tenths of Kelvin for an increase in wind speed of 1 m/s at L-band [34]. This increase will cause an error of about 1 psu (practical salinity unit) of left uncorrected. The exact sensitivity depends on water temperature and salinity. The sea surface roughness must be corrected for accurate salinity retrieval.

3) *Sea Surface Temperature (SST)*

The sensitivity of the brightness temperature to SST is illustrated in Figure 1.9 for vertical and horizontal polarization at the three incidence angles used by the Aquarius

radiometer. A global average value of 32.54 psu for the salinity for the ocean and the Stogryn ocean dielectric model [9] are used. From the figure, it can be seen that a change of 1 psu corresponds to a change in the brightness temperature of 0.25 K in cold water. So the uncertainty of SST must be corrected.

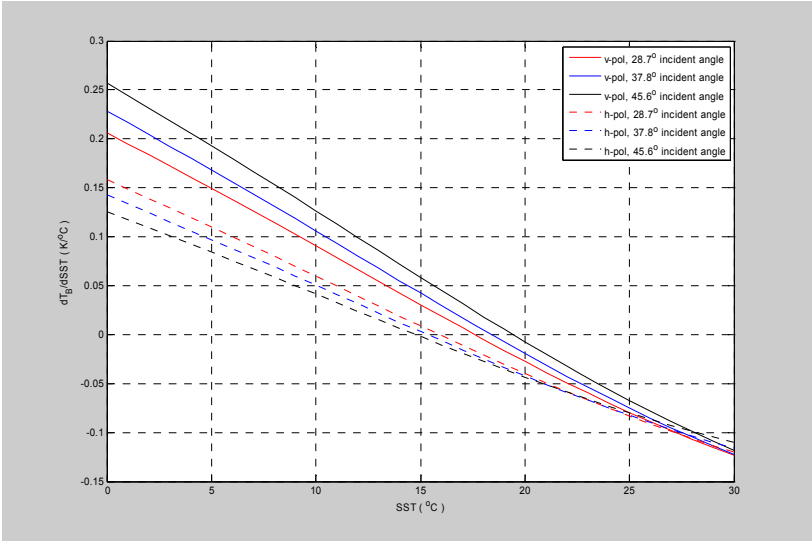

Figure 1.9 The sensitivity of the brightness temperature to the SST

4) *Earth Atmosphere*

When an electromagnetic wave propagates through the earth's atmosphere, the wave will be attenuated by the lossy atmosphere, and extra emission from the atmosphere will be added to the electromagnetic wave and received by the radiometer antenna. At L-band, the atmospheric upwelling and down-welling brightness can be, respectively, modeled using [35]:

$$T_{B,UP} = (1 - e^{-\tau_{atmos}})(SST + 258.15) \tag{1.5.1a}$$

$$T_{B,DOWN} = (1 - e^{-\tau_{atmos}})(SST + 263.15) \tag{1.5.1b}$$

where SST is in units of degrees Celsius;

τ_{atmos} is the line-of sight opacity through the atmosphere in units of Nepers and is given by [35]

$$\tau_{atmos} = (0.009364 + 0.000024127V)\sec(\theta_{inc}) \tag{1.5.2}$$

where θ_{inc} is the incidence angle;

V is the zenith-integrated water vapor burden present in the atmospheric column in units of centimeters. Its global distribution is generally dependent on latitude. Assuming that it varies over the range [0, 7] cm, the variation of received brightness temperature could be 0.1 Kelvin which corresponds to about 0.2 psu uncertainty for the Aquarius radiometer due to the lossy atmosphere.

5) *Faraday Rotation*

With Faraday rotation present, the two linearly polarized field components will be rotated by an angle Ω. If uncorrected, the error in the brightness temperature of each linearly polarized component will be

$$\Delta T_B = (T_v - T_h)\sin^2\Omega - \frac{T_3}{2}\sin 2\Omega \tag{1.5.3}$$

The effect of Faraday rotation at L-band has been discussed in [19, 34, 36-40]. At L-band, the Faraday rotation angle can exceed 10°. For the Aquarius radiometer, the error in T_B can be 0.6 Kelvin for the two linearly polarized components. The effects of Faraday rotation must be properly accounted for in the Aquarius mission. A correction method for the vertically and horizontally polarized sea surface brightness temperatures has been proposed in [19] and an extended error analysis of the brightness temperature estimation is presented in [41].

6) *Solar and Galactic Radiation*

The sun is a strong radiation source with intensity between 0.1 million Kelvin and 10 million Kelvin at L-band [34]. Its radiation enters a radiometer in two ways: directly and reflected by the earth and then received. The effect of solar radiation depends on antenna gain, the geometry of the sun and the antenna, and the earth surface properties.

Galactic radiation enters the radiometer through reflection by the earth surface and through leakage into the antenna's sidelobe, although the latter path is negligibly small and can be ignored. Of these radiation sources, the moon, with a T_B of ~ 200 Kelvin [11], has the biggest contribution because it has the biggest angular extent. The effect of other bodies in our solar system can be ignored. The total background radiation is 2.7 - 6 Kelvin at L-band [35].

7) *Non-ideal Radiometer Antenna*

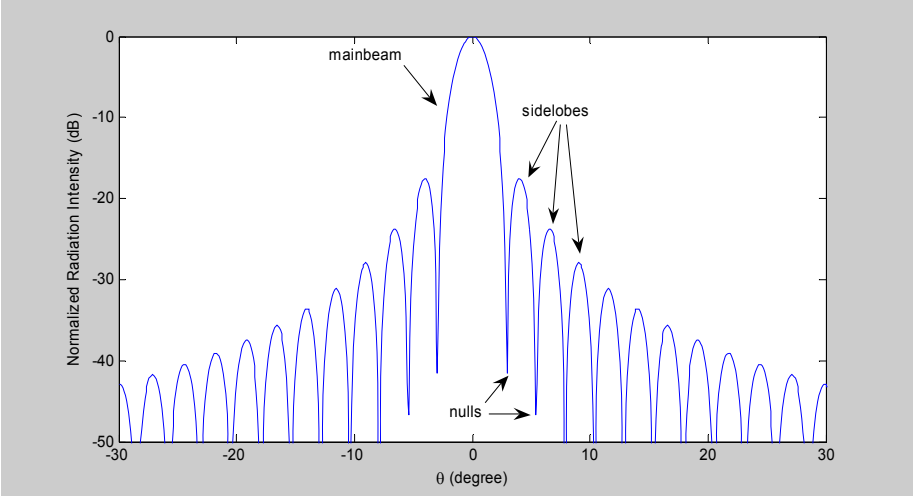

Figure 1.10 Normalized antenna radiation pattern of a uniformly illuminated circular aperture with frequency f=1.413 GHz and aperture radius 2.5 meters

A radiometer antenna receives electromagnetic energy. A real antenna receives/radiates the energy non-uniformly in direction. The directional dependence of

radiation from the antenna is described by its antenna radiation pattern. An example is shown in Figure 1.10. The narrow angular range within which most of the energy is radiated through is called the mainbeam. In addition to the mainbeam, the pattern in Figure 1.10 exhibits several sidelobes in which the sensitivity to incident radiation is generally much less than that in the mainbeam. A local minimum in the radiation pattern is called a null. Because most antennas are reciprocal devices, their radiation patterns are identical to their receiving patterns.

Due to the fact that an antenna's sidelobe level cannot be zero, the energy from all direction radiated toward the antenna might be received by the antenna. Although the receiving ability is not equal in all direction for a practical antenna, the antenna could cause error if it is not correctly characterized due to the following facts:

a) The main-beam solid angle for a practical radiometer antenna is relatively small;

b) The brightness temperatures of the non-target radiation sources in the sidelobe are usually not weak and they are variable;

c) The sidelobes are not flat. Its radiation ability is varied with radiation angle. For example, its radiation is very small around the null points but not small at the peak of the first sidelobe in Figure 1.10. The first sidelobe level is only -17.5 dB relative to the main lobe.

8) *Non-linearity of the radiometer receiver*

A radiometer receiver consists of isolator, filters, amplifier, attenuator, mixer, diode detector, etc in general. In those components, the last gain stage and the diode detector usually determine the non-linearity of a radiometer.

At the input of the last gain stage, the signal strength is no longer weak and it might be beyond the linear range of the last amplifier. Thus any increase in input power will not be matched by a proportional increase in output, and non-linearity will occur.

The diode detector is a square-law detector which detects the input power. Ideally, the output of the detector is proportional to the square of its input voltage, or

$$V_{out} = c \cdot V_{in}^2 \tag{1.5.3}$$

where V_{in} and V_{out} are the input and output voltages respectively, and c is the detection coefficient. In reality, the detector coefficient is a function of the input voltage instead of a constant. That will lead to measurement error if the radiometer receiver has not been characterized carefully in its dynamic range.

9) *Receiver gain variation*

In a radiometer, amplifiers are used to amplify the received thermal signal, whose strength is usually below the thermal noise floor of the radiometer itself. To make the received weak signal detectable, high gain is required by the receiver. These amplifiers are temperature sensitive components, and their stability plays a critical role in a radiometer's performance.

For example, assume a total power radiometer is characterized by the following parameters: 1) the bandwidth of the radiometer is 20 MHz; 2) the receiver noise temperature is 300 Kelvin; 3) the minimum brightness temperature at the antenna terminal is 70 Kelvin; 4) the radiometer output power requirement is 0 dBm (minimum). In this case, the gain of the receiver needs to be 75 dB. For such a high gain receiver, the effects of gain uncertainty need to be considered.

For a total power radiometer, the noise uncertainty ΔT and the gain uncertainty ΔT_G can be considered to be uncorrelated because that they are caused by unrelated physical mechanisms. The total RMS uncertainty is given by [3]

$$\begin{aligned} \Delta T_{total} &= \sqrt{(\Delta T)^2 + (\Delta T_G)^2} \\ &= T_{sys}\sqrt{\frac{1}{B\tau} + \left(\frac{\Delta G_S}{G_S}\right)^2} \end{aligned} \tag{1.5.4}$$

where G_S is the average system power gain;

ΔG_S is the effective (rms) value of the detected power gain variation.

Still using the above example with integration time τ = 0.1s and gain uncertainty $\Delta G_S / G_S$ = 1% (or 0.04 dB), the contribution to the total RMS uncertainty is 0.26 K from the noise uncertainty and 3.70 K from the gain uncertainty.

To reduce the effects of receiver gain variation, the receiver is usually housed in a temperature regulated chamber. With modern state-of-the-art temperature regulated systems, the temperature of the internal components in a radiometer can be maintained to a stability of 0.001 K on one-day timescales [42].

10) *Finite Integration Time and Bandwidth*

A microwave radiometer measurement of brightness temperature (T_B) is an estimate of the variance of a random thermal emission signal derived from samples of the signal. Because the number of samples is always finite, the estimate is itself a random signal. The standard deviation of the estimate is given by the "radiometer uncertainty equation" $\Delta T = KT_{sys}/\sqrt{B\tau}$, where K is an instrument specific constant, T_{sys} is the system noise temperature of the radiometer, B is its pre-detection bandwidth, and τ is the integration time of the measurement [43]. The "ΔT" of a radiometer measurement is of

fundamental importance and often determines the precision with which geophysical parameters of interest can be estimated from measurements of T_B. In most cases, geophysical parameter retrievals are derived from two or more radiometer measurements made at different polarizations and/or frequencies. The uncertainty in the retrieval due to ΔT noise will depend on the variance of the noise and on the covariance between the different measurements.

1.6 Radiometer Calibration

A microwave radiometer is a highly sensitive device. In its measurements, there are unwanted components. Some components are external in origin and others come from the radiometer itself. If the unwanted components are not properly accounted for, errors in TB calibration result. Therefore, the characteristics of the radiometer must be well understood. The antenna performance needs to be known; the receiver gain and equivalent noise temperature must be characterized, etc. All of these can be done by careful and complete radiometer calibration.

There are in general two ways to calibrate a total power radiometer, determined by the calibration sources it uses: either external or internal. For external calibration, the antenna usually points to a known hot reference (the Amazon forest [44], or microwave absorbing material [45]) and a cold reference (usually cold sky with brightness temperature 2.7 Kelvin, or ocean [46, 47]) periodically. This calibration is usually called end-to-end calibration. For internal calibration, the antenna and the receiver are calibrated separately and then integrated together. The antenna is pre-calibrated before integration and temperature sensors are used to monitor it physical temperature after integration all

the time. The receiver in Figure 1.11 is calibrated by using two internal noise sources with different noise level to trace the gain variation/drift. One is usually a matched load whose brightness temperature is its physical temperature, and the other is a noise source of known TB.

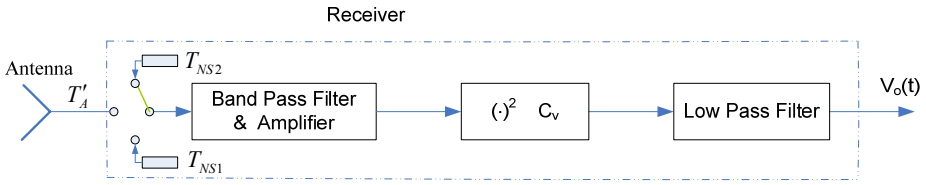

Figure 1.11 Total power radiometer calibration

Then the radiometer receiver can be calibrated using a conventional two-point temperature calibration method, and the gain, g, and offset, O, of the receiver can be obtained by

$$g = \frac{V_{o,1} - V_{o,2}}{T_{NS1} - T_{NS2}} \tag{1.6.1a}$$

$$O = V_{o,1} - gT_{ND,1} \tag{1.6.1b}$$

where $V_{o,1}$, $V_{o,2}$: measurements with the receiver switched to the noise source 1 and 2, respectively;

T_{NS1}, T_{NS2}: brightness temperature of noise sources 1 and 2, respectively.

In this way, the receiver is characterized. When combined with an antenna of known characteristics, the radiometer can be calibrated. External calibration uses a similar approach to calibrate the whole radiometer. In practice, the two kinds of calibration can work together to check each other.

Compared to a conventional total-power radiometer, the calibration of a polarimetric radiometer is more challenging, not only because there are more receiver channels, but also due to the fact that additional parameters of the radiometer, such as channel phase imbalance, need to be measured. As a result, the calibration source of a polarimetric radiometer needs to generate additional controllable and repeatable correlation between vertically and horizontally polarized test signals. Several calibration sources for this purpose have been implemented. For example, a polarized blackbody load has been developed that is capable of producing varying partially correlated calibration signals by varying the relative rotation between the load and the antenna of the radiometer under test [48]. This technique has been adopted by other research groups with an additional phase retardation plate to generate the fourth Stokes parameter [49, 50]. Both of these two practical issues are noteworthy but have some limitations. Very precise mechanical alignment is required in order to guarantee controllable and repeatable Stokes parameters. The requirement that two large black body loads should be in close but at significantly different physical temperatures will make the temperature control problem challenging. For these reasons, an alternative method has been developed using a programmable digital noise source to calibrate a polarimetric radiometer with the ability to calibrate interferometric and autocorrelation microwave radiometers [51]. The programmable noise source is able to produce a wide range of test signals which are used to characterize the radiometer under test (RUT). In particular, signals can be injected with independently controlled levels of 1^{st}, 2^{nd}, 3^{rd} and 4^{th} Stokes brightness temperatures by changing AWG output signal levels and varying the AWG Lookup Tables (LTs) that determine the complex correlation between *v*- and *h*-pol signals.

An X-Band version of the Correlated Noise Calibration Standard (CNCS) has been used previously to characterize and calibrate the correlating receivers in the NASA/U-Michigan airborne Lightweight Rainfall Radiometer [51, 52] and the NASA Goddard Airborne Earth Science Microwave Imaging Radiometer (AESMIR) [53]. A new and improved L-Band version has been completed recently. It is used to evaluate the performance of the Aquarius polarimetric radiometer (a low earth orbiting ocean salinity mission) [54] with a center frequency of 1.413 GHz. The 3rd Stokes in the Aquarius radiometer is used to estimate the degree of ionospheric Faraday rotation [19]. Because there is no 4th Stokes channel in the Aquarius radiometer, it's important to measure the phase imbalance between *v*- and *h*-pol channels and their susceptibility to the 4th Stokes parameter. This is because the input 4th Stokes parameter may be significant and it may vary as a function of surface wind speed [55]. In addition, the stability of its calibrated brightness temperature on time scales of days is particularly relevant.

As the calibration source of a polarimetric radiometer, the CNCS itself needs to be characterized. There are active components in the CNCS, such as Digital-to-Analog Converter (DAC), mixer, frequency source, etc. Not all of these active components are housed in temperature regulated box. In addition, the CNCS channel phase & gain imbalance is not easy to be measured by conventional approach, especially when the signal frequency is high. All of these non-ideal properties of the CNCS need to be precisely determined simultaneously with a polarimetric radiometer calibration.

Throughout the foregoing discussion it was assumed that the receiver and its calibration sources (internal source such as noise diodes, or external source such as the CNCS) are perfectly matched to each other. In practice, this is difficult to be satisfied. The

effect of mismatched components on noise-temperature calibrations can be serious even when the system components appear to be relatively well matched (typical voltage reflection coefficients of less than 0.05) [56].

For a total power radiometer, the impedance mismatching has two effects. First, the effective brightness temperature entering the radiometer receiver from the calibration noise source is reduced; Second, it changes the equivalent receiver brightness temperature propagating the radiometer output. For a fully polarimetric radiometer receiver, the effects of the impedance-mismatching are more complicated because the limited isolation between the two channels of a calibration source will cause extra and unwanted Stokes parameter.

One correction to the CNCS & RUT forward models is necessary if the impedance match between it and the CNCS differs from the match with the antenna that would be connected in place of the CNCS during normal data taking. The impedance mismatch between the CNCS and RUT receiver has two potential effects – it can change the apparent brightness temperature of the CNCS active cold load and it can alter a number of the elements of the RUT's polarimetric gain matrix and offset vector, relative to what they would be when connected to an antenna with a different impedance match. Corrections for both of these effects need to be considered. The impact of impedance mismatches between a radiometer receiver and its antenna on the digital counts measured by the radiometer has been addressed previously by Corbella *et al*. [57-59]. Their approach is adopted here, generalizing the input impedance mismatch to include that with the CNCS as well as the antenna.

Beyond the radiometer gain matrix measurement, linearity is important issue for radiometer calibration. In a radiometer, the square law detector which works at a diode's square law range is the key component to determine the non-linearity of a radiometer. In [60], three approaches are described to characterize the power linearity of microwave detectors for radiometric application. Two of them use sine waves instead of noise signal as the test signal. For a radiometer, the other components besides the square law detector may induce nonlinearity as well. So it's necessary to characterize the nonlinearity of a radiometer receiver as a whole. Several methods have been implemented. In [61], two calibration methods, the 3-point calibration method and the slop method, are described to check the linearity of a radiometer. But the two methods can't deal with a radiometer over wide TB range if the radiometer has an arbitrary transfer characteristic. In addition for the slope method, the accuracy of the variable attenuator is an error source that can't be ignored, as we know that 0.04 dB error on the accuracy of the attenuator will lead to 1% error, and impedance mismatch can cause extra error. In [62], radiometer linearity is measured by a constant noise deflection method which measures the ratio of the 2 local slopes of the radiometer transfer characteristic with one local slope as reference. A variable attenuator is used to adjust the antenna temperature between ~30 K to 4700 K [62]. The accuracy of the antenna temperature is determined by the accuracy of the variable attenuator. It is better to develop a technique to calibrate the (variable) attenuator in-circuit so that the linearity of the radiometer can be accurately characterized over its entire dynamic range.

1.7 Research Objectives and Dissertation Organization

A polarimetric radiometer is a radiometer with the capability to measure the correlation information between the vertically and horizontally polarized fields. To carefully understand and calibrate this type of radiometer, several research projects have been performed.

1) All microwave radiometer measurements of brightness temperature (T_B) include an additive noise component. The variance and correlation statistics of the additive noise component of fully polarimetric radiometer measurements are derived from theoretical considerations and the resulting relationships are verified experimentally. It is found that the noise can be correlated among polarimetric channels and the correlation statistics will vary as a function of the polarization state of the scene under observation.

2) A polarimetric radiometer calibration algorithm has been developed which makes use of the Correlated Noise Calibration Standard (CNCS) to aid in the characterization of microwave polarimetric radiometers and to characterize the non-ideal characteristics of the CNCS itself simultaneously. CNCS has been developed by the Space Physics Research Laboratory of the University of Michigan (SPRL). The calibration algorithm has been verified using the DetMit L-band radiometer. The precision of the calibration is estimated by Monte Carlo simulations. A CNCS forward model has been developed to describe the non-ideal characteristics of the CNCS. Impedance-mismatches between the CNCS and radiometer under test are also considered in the calibration.

3) The calibration technique is demonstrated by applying it to the Engineering Model (EM) of the NASA Aquarius radiometer. CNCS is used to calibrate the Aquarius radiometer – specifically to retrieve its channel phase imbalance and the thermal emission characteristics of transmission line between its antenna and receiver. The impact of errors in calibration of the radiometer channel phase imbalance on Sea Surface Salinity (SSS) retrievals by Aquarius is also analyzed.

4) The CNCS has also been used to calibrate the Breadboard Model (BM) of the L-band NASA Juno radiometer. In order to cover the broad TB dynamic range of the Juno radiometer, a special linearization process has been developed for the CNCS. The method combines multiple Arbitrary Waveform Generator Gaussian noise signals with different values of variance to construct the necessary range of TB levels. The resulting CNCS output signal can simulate the expected TB profile for Juno while in orbit around Jupiter, in particular simulating the strong synchrotron emission signal.

In the following sections, the "ΔT" noise present in measurements of T_3 and T_4 using the coherent detection approach as well as be each of the three incoherent detection approaches in Equation (1.4.6c and 1.4.6d) is derived in Chapter 2. Experimental confirmation of the derivations is also present by comparing the predicted and measured correlation between the measurements of T_v, T_h and T_3 by using a coherent detection radiometer. Chapter 3 introduces the CNCS and its modeling. The polarimetric radiometer calibration algorithm is developed and demonstrated by the DetMit radiometer. CNCS application on the Aquarius radiometers is described in Chapter 4. The analysis of the effect of the calibration error to the SSS retrieval is included in this chapter. CNCS linearization method over a large TB dynamic range is described in

chapter 5. Another CNCS application, to calibrate and characterize the breadboard model of the L-band Juno radiometer [24], is also included in this chapter. Original Contributions and future work are described in Chapter 6.

Chapter 2

Statistics of Radiometer Measurements

The Stokes parameters received by a polarimetric radiometer are estimated by the radiometer. Due to limited integration time, the radiometer measurements contain an AC component of their power spectra that accounts for measurement noise, and that noise can be correlated between channels. The variance and covariance statistics of the measurement noise are derived in this chapter.

There are two types of detection for a polarimetric radiometer: coherent and incoherent. A coherent detection radiometer measures the complex covariance of the vertical and horizontal polarization components of the signal directly, while an incoherent detection radiometer uses the power measurement and then forms the third and fourth Stokes parameters indirectly.

A polarimetric radiometer has multiple receiving channels. For simplicity, let us start with the simplest radiometer—the total power radiometer.

2.1 Noise Variance of a Total Power Radiometer

A total power radiometer consists of an antenna, an amplifier system, a detector and an integrator. It measures the input noise power only. The weak noise signal is

received by the antenna, amplified and filtered by the amplifier system that includes bandpass filter(s). The mean value of the output power from the amplifier system is measured by the detector and the integrator. In the absence of any imperfections, the sensitivity of the total power radiometer is given by ΔT. The simplified block diagram of a total power radiometer is shown below.

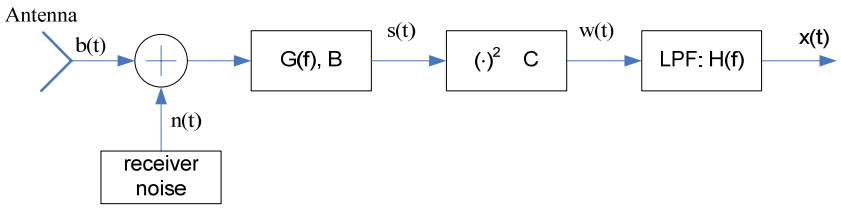

Figure 2.1 Block diagram of a total power radiometer

In Figure 2.1, *G(f)* is the power gain of the receiver with bandwidth *B*. *v(t)* is the amplified and filtered signals. The signal can be written as the sum of an external component, originating from the observation scene and received by the radiometer antenna, and an internal component, originating from noise in the receiver electronics, or

$$s(t) = \sqrt{G}\left[b(t) + n(t)\right] \tag{2.1.1}$$

where $b(t)$ is time varying noise voltages associated with the brightness temperature (see [63] for a detailed definition), and is a scaled versions of the incident electric field, with units of $K^{-1/2}$; $n(t)$ is the receiver noise voltage. Both *b(t)* and *n(t)* are modeled as additive, zero mean, band limited, Gaussian distributed, random variables, and they are uncorrelated. They are associated with the voltage by

$$T_A = \left\langle b^2(t) \right\rangle \tag{2.1.2a}$$

$$T_{rec} = \left\langle n^2(t) \right\rangle \tag{2.1.2b}$$

$$T_{sys} = \left\langle s^2(t) \right\rangle = \left\langle b^2(t) \right\rangle + \left\langle n^2(t) \right\rangle \tag{2.1.2c}$$

where $T_{sys} = T_A + T_{rec}$ is the system noise temperature. T_A is the antenna temperature and T_{rec} is the equivalent receiver noise temperature. $\langle \cdot \rangle$ denotes average.

The signal *s(t)* is a Gaussian distributed random variable, and it is characterized by statistical quantities such as mean, standard deviation, auto correlation, and power spectrum. The auto correlation characterizes the similarity between two measurements of a signal, *s(t)*, as a function of the time separation τ between them, or

$$R_{s,s}(\tau) = \left\langle s(t)s(t-\tau) \right\rangle \tag{2.1.3}$$

The auto correlation of the square law detector output is given by

$$\begin{aligned} R_{w,w}(\tau) &= \left\langle w(t)w(t-\tau) \right\rangle \\ &= c^2 \left\langle s(t)s(t)s(t-\tau)s(t-\tau) \right\rangle \end{aligned} \tag{2.1.4}$$

Because the signal *s(t)* is a zero mean, Gaussian distributed random variable, the identity $\langle abcd \rangle = \langle ab \rangle \langle cd \rangle + \langle ac \rangle \langle bd \rangle + \langle ad \rangle \langle bc \rangle$ can be used [1]. The auto correlation of the signal *w(t)* can be expressed as

$$R_{w,w}(\tau) = c^2 \left\{ R_{s,s}^2(0) + 2R_{s,s}^2(\tau) \right\} \tag{2.1.5}$$

The first term on the right side of Equation (2.1.5) is a constant, so it represents a dc power, while the second term represents an ac power which is the product of two time variables, $R_{s,s}(\tau)R_{s,s}(\tau)$ times $2c^2$. The product of two auto correlations is equal to the convolution of the Fourier transform of each auto correlation.

The Fourier transform of an auto correlation is a power spectral density function. Because s(t) is the summation of 2 independent, additive, zero mean, Gaussian distributed noise signals with the same bandwidth, it is also an additive, zero mean,

Gaussian distributed random signal, and its spectral power density can be regarded as flat within its bandwidth (which is relatively narrow compared with its center frequency). The power spectral density of s(t) and its auto convolution are illustrated in Figure 2.2

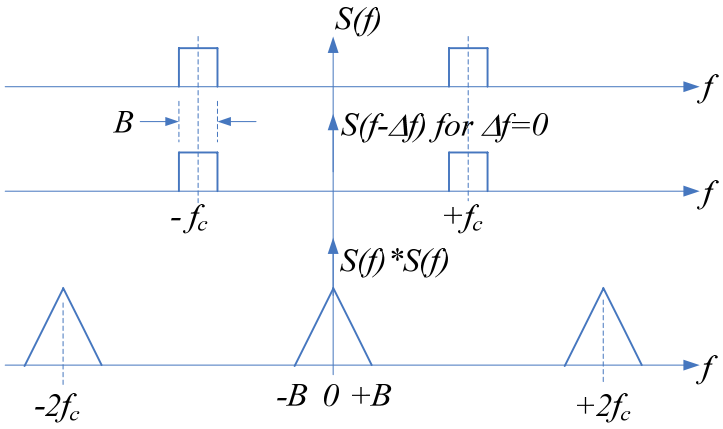

Figure 2.2 Convolution illustration

The Fourier transformation of Equation (2.1.5) is given by

$$W(f) = c^2 \left\{ \int S(f)df \right\}^2 \delta(f) + 2c^2 \{S(f) * S(f)\} \tag{2.1.6}$$

where the sign $*$ is used to indicate the convolution operation and

$$S(f) * S(f) = \int_{-\infty}^{+\infty} S(F)S(F-f)dF \tag{2.17}$$

W(f) is the power spectral density of the square law detector output. When it passes through the low pass filter, *H(f)*, the output is given by

$$\begin{aligned} X(f) &= W(f)H(f) \\ &= c^2 \left\{ \int S(f)df \right\}^2 \delta(f)H(0) + 2c^2 \{S(f) * S(f)\}H(f) \end{aligned} \tag{2.1.8}$$

Because the low pass filter has a relatively narrow passband, only the part of the convolution S(f)*S(f) near zero frequency affects the outcome. So Equation (2.1.8) can be written as

$$X(f) = c^2 \left\{ \int S(f) df \right\}^2 \delta(f) H(0) + 2c^2 \int S^2(f) df H(f) \tag{2.1.9}$$

The ratio of the ac component to dc component is given by

$$\begin{aligned} ratio &= \frac{2c^2 \int S^2(f) df \int H(f) df}{c^2 \left\{ \int S(f) df \right\}^2 H(0)} \\ &= \frac{2 \int G^2(f) df \int H(f) df}{\left\{ \int G(f) df \right\}^2 H(0)} \end{aligned} \tag{2.1.10}$$

Two bandwidths can be defined here. One is the noise bandwidth of the low pass filter, the other is the receiver bandwidth. They are respectively defined as [43]

$$B_n = \frac{\int H(f) df}{H(0)} \tag{2.11a}$$

$$B = \frac{\left\{ \int G(f) df \right\}^2}{\int G^2(f) df} \tag{2.11b}$$

The ratio of the ac to dc power in the radiometer receiver output is given by

$$\frac{\Delta X}{\langle X \rangle} = \sqrt{\frac{2B_n}{B}} \tag{2.1.12}$$

Since the square law detector is used in the radiometer, the radiometer output voltage is proportional to the input power or power density. The ratio of the corresponding input power density change in temperature is given by

$$\begin{aligned} \frac{\Delta T}{T_{sys}} &= \sqrt{\frac{2B_n}{B}} \\ &= \frac{1}{\sqrt{B\tau}} \end{aligned} \tag{2.1.13}$$

where ΔT is the minimum detectable temperature change;

$T_{sys} = T_A + T_{rec}$ is the receiver system noise temperature;

τ is the integration time.

2.2 Noise Covariance of an Incoherent Detection, Hybrid Combing Polarimetric Radiometer

An incoherent detection radiometer measures the variance of certain polarimetric components of the signal — most often the ±45° slant linear and left and right hand circular polarizations that are most commonly formed using hybrid combiner and 90° phase shifter — in addition to the vertical and horizontal polarizations, and then forms the third and fourth Stokes parameters indirectly.

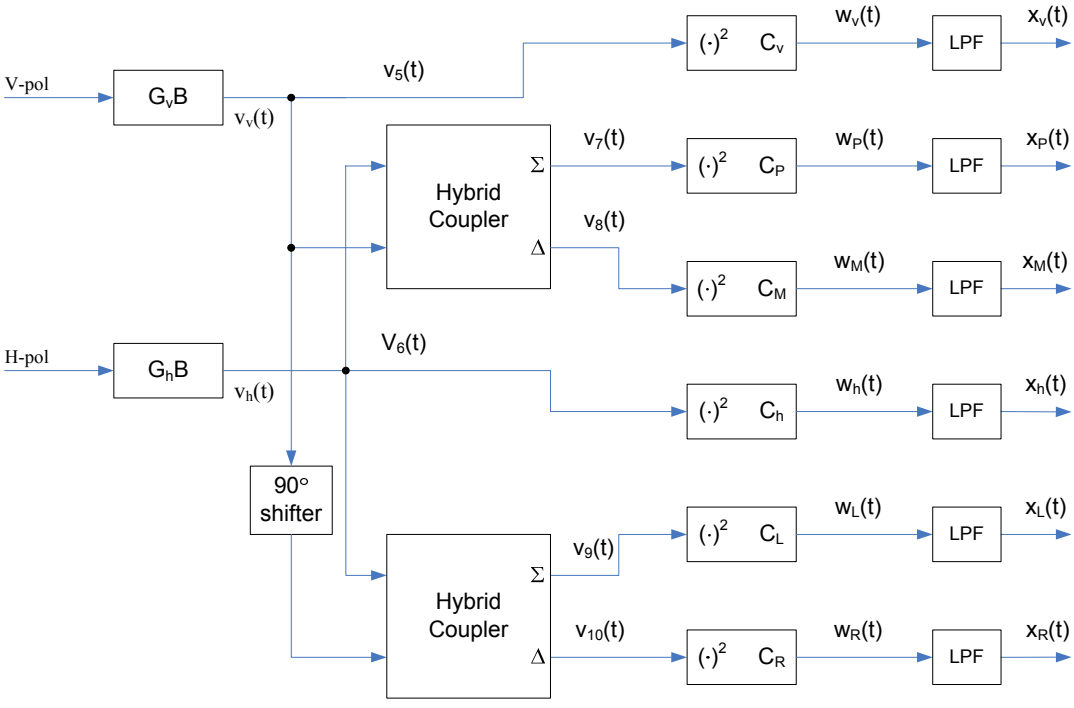

Figure 2.3 Signal flow diagram for a hybrid combining polarimetric microwave radiometer.

The signal flow through a hybrid combining polarimetric microwave radiometer is diagramed in Figure 2.3. In the figure, G_v and G_h represent the gains of the *v*-pol and *h*-pol channels respectively, B is their bandwidth (assumed equal), $v_v(t)$ and $v_h(t)$ are the amplified and filtered signals from the *v*-pol and *h*-pol channels respectively. These two signals can be written as the sum of an external component, originating from the observation scene, and an internal component, originating from noise in the receiver electronics, or

$$\begin{aligned} v_v(t) &= \sqrt{G_v}\left[b_v(t) + n_v(t)\right] \\ v_h(t) &= \sqrt{G_h}\left[b_h(t) + n_h(t)\right] \end{aligned} \tag{2.2.1}$$

where $b_v(t)$ and $b_h(t)$ are time varying noise voltages associated with the brightness temperature (see [63] for a detailed definition), and are scaled versions of the incident electric field, with units of $K^{-1/2}$; $n_v(t)$ and $n_h(t)$ are receiver noise voltages in the *v*- and *h*-pol channels. Both $b(t)$ and $n(t)$ are modeled as additive, zero mean, band limited, gaussian distributed, random variables. The auto and cross correlation relationships between the voltages associated with the brightness temperatures are given by [63]

$$\left\langle b_v(t) b_v(t-\tau) \right\rangle = T_v \cos(2\pi f_c \tau)\mathrm{sinc}(B\tau) \tag{2.2.2a}$$

$$\left\langle b_h(t) b_h(t-\tau) \right\rangle = T_h \cos(2\pi f_c \tau)\mathrm{sinc}(B\tau) \tag{2.2.2b}$$

$$\left\langle b_v(t) b_h(t-\tau) \right\rangle = \left\{ \frac{T_3}{2}\cos(2\pi f_c \tau) - \frac{T_4}{2}\sin(2\pi f_c \tau) \right\} \mathrm{sinc}(B\tau) \tag{2.2.2c}$$

where T_v and T_h are the *v*-pol and *h*-pol antenna temperatures, f_c is the center frequency of the signal, B is its bandwidth, and $\mathrm{sinc}(u)=\sin(\pi u)/(\pi u)$. The variance and covariance of the signals are found by evaluating these auto-correlations at $\tau=0$, or

$$\left\langle b_v^2(t)\right\rangle = T_v \tag{2.2.3a}$$

$$\left\langle b_h^2(t)\right\rangle = T_h \tag{2.2.3b}$$

$$\left\langle b_v(t)b_h(t)\right\rangle = \frac{T_3}{2} \tag{2.2.3c}$$

The variance of *n(t)* is similarly related to the receiver noise temperature by

$$\left\langle n_v^2(t)\right\rangle = T_{Rv} \tag{2.2.4a}$$

$$\left\langle n_h^2(t)\right\rangle = T_{Rh} \tag{2.2.4b}$$

where T_{Rv} and T_{Rh} are the noise temperatures of the *v*-pol and *h*-pol receivers. The receiver noise is uncorrelated between channels, so that

$$\left\langle n_v(t)n_h(t)\right\rangle = 0 \tag{2.2.5}$$

A hybrid combining polarimetric radiometer forms $\pm 45^o$ slant linearly, left- and right-hand circularly polarized channels from $v_v(t)$ and $v_h(t)$ by summing and differencing them in a hybrid coupler as shown in Figure 2.3. The signals $v_v(t)$ and $v_h(t)$ are first split into three channels equally, or

$$v_5(t) = v_v(t) \tag{2.2.6a}$$

$$v_6(t) = v_h(t) \tag{2.2.6b}$$

Here the constant $1/\sqrt{3}$ is ignored since it doesn't affect the relation among the radiometer outputs.

The hybrid coupler in Figure 2.3 adds and subtracts its two input signals to produce the slant linear polarization signals, or

$$v_7(t) = \frac{v_h(t) + v_v(t)}{\sqrt{2}} \tag{2.2.7a}$$

$$v_8(t) = \frac{v_h(t) - v_v(t)}{\sqrt{2}} \tag{2.2.7b}$$

One channel of the *v*-pol signal will pass through the 90° phase shifter in Figure 2.3, and then is combined with one channel of the *h*-pol signal from the other hybrid coupler to produce the circularly polarization signals, or

$$v_9(t) = \frac{v_h(t) + v_v(t - \frac{1}{4f_c})}{\sqrt{2}} \tag{2.2.7a}$$

$$v_{10}(t) = \frac{v_h(t) - v_v(t - \frac{1}{4f_c})}{\sqrt{2}} \tag{2.2.7b}$$

where f_c is the RF center frequency of the signal.

The output signals from the hybrid as well as the original signals are then passed through square law detectors. Their outputs are given by

$$w_v(t) = c_v v_v^2(t) \tag{2.2.8a}$$

$$w_P(t) = \frac{c_P}{2}\left[v_h(t) + v_v(t)\right]^2 \tag{2.2.8b}$$

$$w_M(t) = \frac{c_M}{2}\left[v_h(t) - v_v(t)\right]^2 \tag{2.2.8c}$$

$$w_h(t) = c_h v_h^2(t) \tag{2.2.8d}$$

$$w_L(t) = \frac{c_L}{2}\left[v_h(t) + v_v(t - \frac{1}{4f_c})\right]^2 \tag{2.2.8e}$$

$$w_R(t) = \frac{c_R}{2}\left[v_h(t) - v_v(t - \frac{1}{4f_c}) \right]^2 \tag{2.2.8f}$$

where c_x is the detector sensitivity for polarization channel x = *v, P, M, h, L* and *R*. Finally, the four signals are integrated and sampled. The integration process is modeled as an ideal low pass filters (LPF in Figure 2.3). The low pass filtered versions of the four polarization signals are, respectively, $x_v(t)$, $x_P(t)$, $x_M(t)$, $x_h(t)$, $x_L(t)$ and $x_R(t)$. The expected value of these signals (*i.e.* the DC component of their spectra) is proportional to the four associated brightness temperatures. The variance of the signals (*i.e.* the integral over the AC component of their spectra) represents the additive noise present in the measurements.

The auto correlations and cross correlations and the spectra and cross spectra of the four low pass filtered signals, $x_v(t)$, $x_P(t)$, $x_M(t)$, $x_h(t)$, $x_L(t)$ and $x_R(t)$, can be derived with using the identity $\langle abcd \rangle = \langle ab \rangle \langle cd \rangle + \langle ac \rangle \langle bd \rangle + \langle ad \rangle \langle bc \rangle$, which is valid for zero mean, gaussian distributed random variables [43]. From these, it is possible to compute their covariance and related statistics. The correlation coefficient between $x_v(t)$ and $x_P(t)$ can be expressed as

$$\rho_{v,P} = \frac{\left(T_{sys,v} + \frac{\sqrt{g}}{2} T_3 \right)^2 + \frac{g}{4} T_4^2}{T_{sys,v} \cdot \left(T_{sys,v} + g T_{sys,h} + \sqrt{g} T_3 \right)} \tag{2.2.9a}$$

where $g = G_2/G_1$ is the ratio of *v*-pol to *h*-pol channel gains. $T_{sys,v} = T_v + T_{Rv}$ and $T_{sys,h} = T_h + T_{Rh}$ are the equivalent system noise temperatures of the *v*- and *h*-pol channels, respectively. Similarly, for the correlation between other polarization pairs, we have

$$\rho_{v,M} = \frac{\left(T_{sys,v} - \frac{\sqrt{g}}{2}T_3\right)^2 + \frac{g}{4}T_4^2}{T_{sys,v}\cdot\left(T_{sys,v} + gT_{sys,h} - \sqrt{g}T_3\right)} \tag{2.2.9b}$$

$$\rho_{v,h} = \frac{T_3^2 + T_4^2}{4T_{sys,v}\cdot T_{sys,h}} \tag{2.2.9c}$$

$$\rho_{v,L} = \frac{\left(T_{sys,v} + \frac{\sqrt{g}}{2}T_4\right)^2 + \frac{g}{4}T_3^2}{T_{sys,v}\cdot\left(T_{sys,v} + gT_{sys,h} + \sqrt{g}T_4\right)} \tag{2.2.9d}$$

$$\rho_{v,R} = \frac{\left(T_{sys,v} - \frac{\sqrt{g}}{2}T_4\right)^2 + \frac{g}{4}T_3^2}{T_{sys,v}\cdot\left(T_{sys,v} + gT_{sys,h} - \sqrt{g}T_4\right)} \tag{2.2.9e}$$

$$\rho_{P,M} = \frac{\left(T_{sys,v} - gT_{sys,h}\right)^2 + gT_4^2}{\left(T_{sys,v} + gT_{sys,h} + \sqrt{g}T_3\right)\cdot\left(T_{sys,v} + gT_{sys,h} - \sqrt{g}T_3\right)} \tag{2.2.9f}$$

$$\rho_{P,h} = \frac{\left(gT_{sys,h} + \frac{\sqrt{g}}{2}T_3\right)^2 + \frac{g}{4}T_4^2}{gT_{sys,h}\cdot\left(T_{sys,v} + gT_{sys,h} + \sqrt{g}T_3\right)} \tag{2.2.9g}$$

$$\rho_{P,L} = \frac{\left[T_{sys,v} + \frac{\sqrt{g}}{2}\left(T_3 + T_4\right)\right]^2 + \left[gT_{sys,h} + \frac{\sqrt{g}}{2}\left(T_3 + T_4\right)\right]^2}{\left(T_{sys,v} + gT_{sys,h} + \sqrt{g}T_3\right)\cdot\left(T_{sys,v} + gT_{sys,h} + \sqrt{g}T_4\right)} \tag{2.2.9h}$$

$$\rho_{P,R} = \frac{\left[T_{sys,v} + \frac{\sqrt{g}}{2}\left(T_3 - T_4\right)\right]^2 + \left[gT_{sys,h} + \frac{\sqrt{g}}{2}\left(T_3 - T_4\right)\right]^2}{\left(T_{sys,v} + gT_{sys,h} + \sqrt{g}T_3\right)\cdot\left(T_{sys,v} + gT_{sys,h} - \sqrt{g}T_4\right)} \tag{2.2.9i}$$

$$\rho_{M,h} = \frac{\left(gT_{sys,h} - \frac{\sqrt{g}}{2}T_3\right)^2 + \frac{g}{4}T_4^2}{gT_{sys,h}\cdot\left(T_{sys,v} + gT_{sys,h} - \sqrt{g}T_3\right)} \tag{2.2.9j}$$

$$\rho_{M,L} = \frac{\left[T_{sys,v} - \frac{\sqrt{g}}{2}\left(T_3 - T_4\right)\right]^2 + \left[gT_{sys,h} - \frac{\sqrt{g}}{2}\left(T_3 - T_4\right)\right]^2}{\left(T_{sys,v} + gT_{sys,h} - \sqrt{g}T_3\right)\cdot\left(T_{sys,v} + gT_{sys,h} + \sqrt{g}T_4\right)} \tag{2.2.9k}$$

$$\rho_{M,R} = \frac{\left[T_{sys,v} - \frac{\sqrt{g}}{2}\left(T_3 + T_4\right)\right]^2 + \left[gT_{sys,h} - \frac{\sqrt{g}}{2}\left(T_3 + T_4\right)\right]^2}{\left(T_{sys,v} + gT_{sys,h} - \sqrt{g}T_3\right)\cdot\left(T_{sys,v} + gT_{sys,h} - \sqrt{g}T_4\right)} \tag{2.2.9l}$$

$$\rho_{h,L} = \frac{\left(gT_{sys,h} + \frac{\sqrt{g}}{2}T_4\right)^2 + \frac{g}{4}T_3^2}{gT_{sys,h}\cdot\left(T_{sys,v} + gT_{sys,h} + \sqrt{g}T_4\right)} \tag{2.2.9m}$$

$$\rho_{h,R} = \frac{\left(gT_{sys,h} - \frac{\sqrt{g}}{2}T_4\right)^2 + \frac{g}{4}T_3^2}{gT_{sys,h}\cdot\left(T_{sys,v} + gT_{sys,h} - \sqrt{g}T_4\right)} \tag{2.2.9n}$$

$$\rho_{L,R} = \frac{\left(T_{sys,v} - gT_{sys,h}\right)^2 + gT_3^2}{\left(T_{sys,v} + gT_{sys,h} + \sqrt{g}T_4\right)\cdot\left(T_{sys,v} + gT_{sys,h} - \sqrt{g}T_4\right)} \tag{2.2.9o}$$

Note that the correlation coefficients are independent of bandwidth, B, and integration time, τ.

The ΔT of each channel is given by

$$\Delta T_v = \frac{T_{sys,v}}{\sqrt{B\tau}} = \frac{T_v + T_{Rv}}{\sqrt{B\tau}} \tag{2.2.10a}$$

$$\begin{aligned}\Delta T_P &= \frac{T_{sys,P}}{\sqrt{B\tau}} \\ &= \frac{1}{\sqrt{B\tau}}\cdot\frac{T_{sys,v} + gT_{sys,h} + \sqrt{g}T_3}{2\sqrt{g}}\end{aligned} \tag{2.2.10b}$$

$$\begin{aligned}\Delta T_M &= \frac{T_{sys,M}}{\sqrt{B\tau}} \\ &= \frac{1}{\sqrt{B\tau}}\cdot\frac{T_{sys,v} + gT_{sys,h} - \sqrt{g}T_3}{2\sqrt{g}}\end{aligned} \tag{2.2.10c}$$

$$\Delta T_h = \frac{T_{sys,h}}{\sqrt{B\tau}} = \frac{T_h + T_{Rh}}{\sqrt{B\tau}} \tag{2.2.10d}$$

$$\begin{aligned} \Delta T_L &= \frac{T_{sys,L}}{\sqrt{B\tau}} \\ &= \frac{1}{\sqrt{B\tau}} \cdot \frac{T_{sys,v} + gT_{sys,h} + \sqrt{g}T_4}{2\sqrt{g}} \end{aligned} \tag{2.2.10e}$$

$$\begin{aligned} \Delta T_R &= \frac{T_{sys,R}}{\sqrt{B\tau}} \\ &= \frac{1}{\sqrt{B\tau}} \cdot \frac{T_{sys,v} + gT_{sys,h} - \sqrt{g}T_4}{2\sqrt{g}} \end{aligned} \tag{2.2.10f}$$

2.3 Noise Covariance of a Coherent Detection, Correlating Polarimetric Radiometer

In comparison to an incoherent detection radiometer, a coherent detection radiometer measures the complex covariance of the vertical and horizontal polarization components of the signal directly. The covariance can be measured by an analog complex-multiplier or by digitizing the vertical and horizontal polarization components of the signal and then multiplying and averaging (*i.e.* correlating) them in a digital signal processor if digital-correlation technology is used. The resulting components of T_B are designated T_3 and T_4 for the real and imaginary components of correlation, respectively.

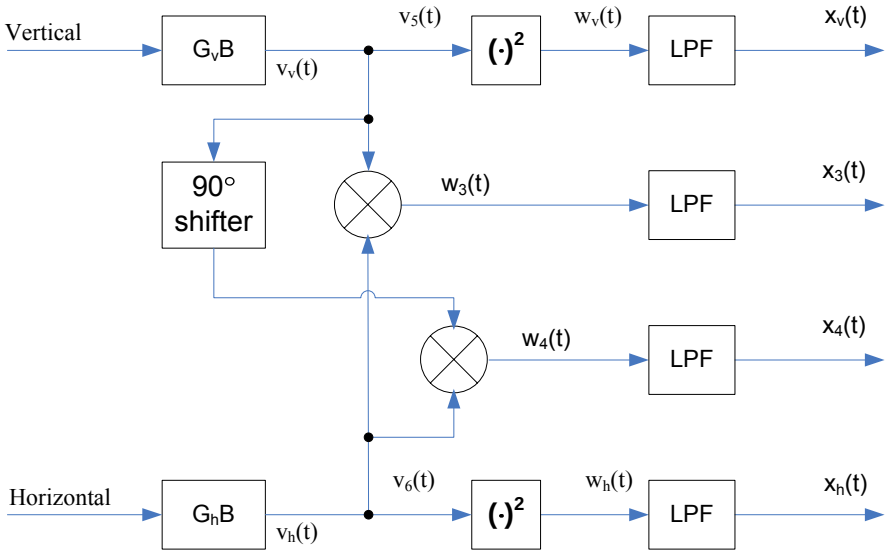

Figure 2.4 Signal flow diagram for a correlating polarimetric microwave radiometer.

The signal flow through a coherent detection, correlating polarimetric radiometer is shown in Figure 2.4. The signals $v_v(t) \sim v_6(t)$, $n_v(t)$, $n_h(t)$, $b_v(t)$, $b_h(t)$ and their correlation statistics are identical to those associated with the hybrid combining radiometer analysis given in Section 2.1, as are the two low pass filtered signals, $x_v(t)$ and

$x_h(t)$, for the vertically and horizontally polarized channels. The signals in the cross-correlating channels of the radiometer, prior to low pass filtering, are given by

$$w_3(t) = v_v(t) \cdot v_h(t) \tag{2. 3.1a}$$

$$w_4(t) = v_v(t - \frac{1}{4f_c}) \cdot v_h(t) \tag{2.3.1b}$$

After the low pass filter, the correlating channel signals become $x_3(t)$ and $x_4(t)$ respectively. The procedure followed to derive the covariance relationships between the three low pass filtered signals is similar to that for the hybrid combining radiometer. The correlation coefficient between the outputs $x_v(t)$, $x_3(t)$, $x_4(t)$ and $x_h(t)$ can be expressed as follows

$$\begin{aligned} \rho_{v,3} &= \frac{R_{v,3}^{AC}(t)}{\sqrt{R_{v,v}^{AC}(t)} \cdot \sqrt{R_{3,3}^{AC}(t)}} \\ &= \frac{\sqrt{2}T_3}{\sqrt{4T_{sys,v}T_{sys,h} + \left(T_3^2 - T_4^2\right)}} \end{aligned} \tag{2.3.2a}$$

Similarly for the other channel pairs, we have

$$\rho_{v,4} = \frac{\sqrt{2}T_4}{\sqrt{4T_{sys,v}T_{sys,h} - \left(T_3^2 - T_4^2\right)}} \tag{2. 3.2b}$$

$$\rho_{v,h} = \frac{T_3^2 + T_4^2}{4T_{sys,v}T_{sys,h}} \tag{2. 3.2c}$$

$$\rho_{3,4} = \frac{2T_3T_4}{\sqrt{16T_{sys,v}^2T_{sys,h}^2 - \left(T_3^2 - T_4^2\right)^2}} \tag{2. 3.2d}$$

$$\rho_{3,h} = \frac{\sqrt{2}T_3}{\sqrt{4T_{sys,v}T_{sys,h} + \left(T_3^2 - T_4^2\right)}} \tag{2. 3.2e}$$

$$\rho_{4,h} = \frac{\sqrt{2}T_4}{\sqrt{4T_{sys,v}T_{sys,h} - \left(T_3^2 - T_4^2\right)}} \tag{2. 3.2f}$$

The NEΔT of each channel is given by

$$\Delta T_v = \frac{T_{va} + T_{R1}}{\sqrt{B\tau}} \tag{2.3.3a}$$

$$\Delta T_3 = \sqrt{\frac{4T_{sys,v}T_{sys,h} + \left(T_3^2 - T_4^2\right)}{2B\tau}} \tag{2.3.3b}$$

$$\Delta T_4 = \sqrt{\frac{4T_{sys,v}T_{sys,h} - \left(T_3^2 - T_4^2\right)}{2B\tau}} \tag{2.3.3c}$$

$$\Delta T_h = \frac{T_{ha} + T_{R2}}{\sqrt{B\tau}} \tag{2.3.3d}$$

2.4 Application – the Third and Fourth Stokes TBs with a Hybrid Combing Radiometer

The third and fourth Stokes brightness temperature can be obtained from the measurements made by a hybrid combining polarimetric radiometer. The method is given by

$$\begin{aligned} T_3 &= (2n+1)(T_v + T_h) - 2nT_P - 2(n+1)T_M \\ &= \begin{bmatrix} 2n+1 & 2n+1 & -2n & -2(n+1) & 0 & 0 \end{bmatrix} \cdot \begin{bmatrix} T_v & T_h & T_P & T_M & T_L & T_R \end{bmatrix}^t \end{aligned} \tag{2.4.1a}$$

$$\begin{aligned} T_4 &= (2n+1)(T_v + T_h) - 2nT_L - 2(n+1)T_R \\ &= \begin{bmatrix} 2n+1 & 2n+1 & 0 & 0 & -2n & -2(n+1) \end{bmatrix} \cdot \begin{bmatrix} T_v & T_h & T_P & T_M & T_L & T_R \end{bmatrix}^t \end{aligned} \tag{2.4.1b}$$

where n is any real number and T_v, T_h, T_P, T_M, T_L and T_R are the measured brightness temperatures. The three methods in [29] to obtained the third and fourth Stokes

brightness temperature are special cases of Equation (2.4.1) with n = -0.5, 0 and -1 respectively.

The variance of T_3 (or T_4) can be obtained using the error propagator

$$\Lambda_{T3/4} = A \cdot \Lambda_T \cdot A^t \tag{2. 4.2}$$

where A, the 1×6 matrix satisfying $T_{3/4} = A \cdot T$, is given in (2.4.1) for each method and where $T = \begin{bmatrix} T_v & T_h & T_P & T_M & T_L & T_R \end{bmatrix}^t$ is the random vector with covariance matrix Λ_T. Λ_T, the covariance matrix for the signals $x_v(t)$, $x_h(t)$, $x_P(t)$, $x_M(t)$, $x_L(t)$ and $x_R(t)$, can be expressed as

$$\Lambda_T = \begin{bmatrix} R^{AC}_{v,v}(0) & R^{AC}_{v,h}(0) & R^{AC}_{v,P}(0) & R^{AC}_{v,M}(0) & R^{AC}_{v,L}(0) & R^{AC}_{v,R}(0) \\ R^{AC}_{h,v}(0) & R^{AC}_{h,h}(0) & R^{AC}_{h,P}(0) & R^{AC}_{h,M}(0) & R^{AC}_{h,L}(0) & R^{AC}_{h,R}(0) \\ R^{AC}_{P,v}(0) & R^{AC}_{P,h}(0) & R^{AC}_{P,P}(0) & R^{AC}_{P,M}(0) & R^{AC}_{P,L}(0) & R^{AC}_{P,R}(0) \\ R^{AC}_{M,v}(0) & R^{AC}_{M,h}(0) & R^{AC}_{M,P}(0) & R^{AC}_{M,M}(0) & R^{AC}_{M,L}(0) & R^{AC}_{M,R}(0) \\ R^{AC}_{L,v}(0) & R^{AC}_{L,h}(0) & R^{AC}_{L,P}(0) & R^{AC}_{L,M}(0) & R^{AC}_{L,L}(0) & R^{AC}_{L,R}(0) \\ R^{AC}_{R,v}(0) & R^{AC}_{R,h}(0) & R^{AC}_{R,P}(0) & R^{AC}_{R,M}(0) & R^{AC}_{R,L}(0) & R^{AC}_{R,R}(0) \end{bmatrix} \tag{2.4.3}$$

where $R^{AC}_{X,Y}(0)$ denotes the variance of *X(t)* if *X(t)=Y(t)* or the covariance of *X(t)* and *Y(t)* if *X(t)≠Y(t)*. Detail expressions for these variance and covariance elements are shown in [64]. If these expressions are substituted into (2.4.3), the covariance matrix can be obtained. The covariance for the third Stokes brightness temperature is given by

$$\Lambda_{T3} = A \cdot \Lambda_T \cdot A^t = \frac{G_v^2}{B\tau}\left(\alpha n^2 + \beta n + \gamma\right) \tag{2.4.4}$$

where

$$
\begin{aligned}
\alpha = {} & T_{sys,v}^2\left(4c_v^2 + c_P^2 + c_M^2 - 4c_vc_P - 4c_vc_M + 2c_Pc_M\right) \\
& + g^2T_{sys,h}^2\left(4c_h^2 + c_P^2 + c_M^2 - 4c_hc_P - 4c_hc_M + 2c_Pc_M\right) \\
& + gT_{sys,v}T_{sys,h}2\left(c_M - c_P\right)^2 \\
& + \sqrt{g}T_{sys,v}T_3\left\{2\left(c_v - c_P\right)^2 - 2\left(c_v - c_M\right)^2\right\} \\
& + \sqrt{g}gT_{sys,h}T_3\left\{2\left(c_h - c_P\right)^2 - 2\left(c_h - c_M\right)^2\right\} \\
& + gT_3^2\left(4c_vc_h - 2c_vc_P - 2c_Pc_h - 2c_vc_M - 2c_Mc_h + 2c_P^2 + 2c_M^2\right) \\
& + gT_4^2\left(4c_vc_h - 2c_vc_P - 2c_Pc_h - 2c_vc_M - 2c_Mc_h + 4c_Pc_M\right)
\end{aligned}
\tag{2.4.5a}
$$

$$
\begin{aligned}
\beta = {} & T_{sys,v}^2\left(4c_v^2 + 2c_M^2 - 2c_vc_P - 6c_vc_M + 2c_Pc_M\right) \\
& + g^2T_{sys,h}^2\left(4c_h^2 + 2c_M^2 - 2c_hc_P - 6c_hc_M + 2c_Pc_M\right) \\
& + gT_{sys,v}T_{sys,h}4\left(c_M - c_P\right)c_M \\
& + \sqrt{g}T_{sys,v}T_3\left\{2\left(c_v - c_P\right)c_v - 2\left(c_v - c_M\right)\left(c_v - 2c_M\right)\right\} \\
& + \sqrt{g}gT_{sys,h}T_3\left\{2\left(c_h - c_P\right)c_h - 2\left(c_h - c_M\right)\left(c_h - 2c_M\right)\right\} \\
& + \frac{g}{2}T_3^2\left(4c_vc_h - c_vc_P - c_Pc_h - 3c_vc_M - 3c_Mc_h + 4c_M^2\right) \\
& + \frac{g}{2}T_4^2\left(4c_vc_h - c_vc_P - c_Pc_h - 3c_vc_M - 3c_Mc_h + 4c_Pc_M\right)
\end{aligned}
\tag{2.4.5b}
$$

$$
\begin{aligned}
\gamma = {} & T_{sys,v}^2\left(c_v - c_M\right)^2 + g^2T_{sys,h}^2\left(c_h - c_M\right)^2 + gT_{sys,v}T_{sys,h}2c_M^2 \\
& + \frac{\sqrt{g}}{2}T_{sys,v}T_3\left\{c_v^2 - \left(c_v - 2c_M\right)^2\right\} + \frac{\sqrt{g}g}{2}T_{sys,h}T_3\left\{c_h^2 - \left(c_h - 2c_M\right)^2\right\} \\
& + \frac{g}{2}T_3^2\left\{c_vc_h - c_vc_M - c_Mc_h + 2c_M^2\right\} + \frac{g}{2}T_4^2\left\{c_vc_h - c_vc_M - c_Mc_h\right\}
\end{aligned}
\tag{2.4.5c}
$$

Replacing c_P, c_M, T_3 and T_4 with c_L, c_R, T_4 and T_3 respectively, the covariance for the fourth Stokes brightness temperature can be obtained.

For the third Stokes parameter's covariance, if the detector sensitivities c_v, c_P, c_M and c_h are the same (*i.e.* if c_v=c_P=c_M=c_h), the variance will be independent of the value of n. In other words, the variance of each version of T_3 in [29] is also the same. This might, at first glance, seem counterintuitive. For example, if the additive noise in measurements of T_v, T_h, T_P and T_M had been uncorrelated, the variance of $T_{3.1}$ (= $T_P - T_M$) would have

been double that of either T_P or T_M whereas the variance of both $T_{3.2}$ (= $2T_P - T_v - T_h$) and $T_{3.3}$ (= $-2T_M + T_v + T_h$) would have been four times that amount. In fact, the partial correlation between the additive noise in T_v, T_h, T_P and T_M precisely compensates so that the variances for all methods are equal. For the case of c_v=c_P=c_M=c_h=1 which can be implemented using a digital correlator module, such as [65], the standard deviation of the additive noise in T_3 is independent of n and it is given by

$$\Delta T_3 = \sqrt{\frac{4T_{sys,v}T_{sys,h} + \left(T_3^2 - T_4^2\right)}{2B\tau}} \tag{2.4.6a}$$

The same result applies for T_4. For the case of c_v=c_L=c_R=c_h=1, the standard deviation of the additive noise in T_4 is independent of n as well and it is given by

$$\Delta T_4 = \sqrt{\frac{4T_{sys,v}T_{sys,h} - \left(T_3^2 - T_4^2\right)}{2B\tau}} \tag{2.4.6b}$$

2.5 Experimental Verification of Covariance Relationship

Some of the noise correlation statistics derived above have been evaluated experimentally. The DetMit radiometer [66] was used which has separate vertical and horizontal linear polarization input channels, followed by standard amplification, down conversion and square law detection stages for the two channels plus a third channel that digitizes the two signals, multiplies them together, and averages the product. Thus, this is a correlating polarimetric radiometer, of the type described in Section 2.3, which can measures T_v, T_h and T_3. Signals entering the *v*- and *h*-pol input ports of the radiometer were generated using the CNCS. CNCS is a programmable polarimetric calibration target that is capable of generating pairs of thermal noise signals with precisely adjustable

and repeatable relative correlation statistics [51, 67, 68]. The dynamic range of brightness temperatures that can be generated is approximately 90 K to 350 K for T_v and T_h and –550 K to +550K for T_3 and T_4. For purposes of this experiment, stable 90 K and 310 K T_Bs were generated at both *v*- and *h*-pol as calibration references for the radiometer. The calibration signals were uncorrelated (T_3=T_4 =0). Interleaved between the calibration signals were signals for which $T_v = T_h$ = 400 K and the partial correlation between T_v and T_h was adjusted so that T_3 varied between 0 K and 550 K in ten uniformly spaced steps. Because the radiometer does not measure T_4, the quadrature component of the correlation between *v*- and *h*-pol signals was set to zero.

For each value of T_3, an extended time series of measurements of T_v, T_h and T_3 was recorded simultaneously. From these measurements, correlation coefficients between the additive noise in each channel can be derived. This process was repeated three times as a means of determining the standard error and repeatability of the estimates of the correlation coefficient statistic. The results are shown in Figure 2.5a-c, which respectively plot the average and standard deviation of the correlation between the noise in T_v and T_3, T_h and T_3, and T_v and T_h as a function of T_3. The correlation values that are predicted by theory are also plotted for comparison. The predicted and measured correlations in Figure 2.5a and Figure 2.5b agree closely, with correlation rising monotonically as a function of T_3. This behavior is what produced the similar values for the ΔT of T_3 noted in Section 2.3, regardless of which of the three methods was used to derive it from hybrid combining radiometer measurements. In Figure 2.5c, both the predicted and measured correlation between noise in T_v and T_h is quite low but can be seen to increase at the higher values of T_3. However, even at the high value of T_3 such as

300 K, the very small level of correlation would in most practical applications not be a concern.

The reason that the measured correlations are lower than the theoretical predictions is probably due to glitches in the measurement data. The glitches are generated from so called pseudo-random test signal. In the experiment, the thermal noise signals are simulated by repeatedly outputting the CNCS Lookup Table data that is random digital counts. The size of the CNCS Lookup Table data is 262144 samples, and the output speed is 1.25 Giga-samples while data sample frequency of the radiometer under test is 110 MHz. 36 ms' data are averaged and then output for analysis. Under the condition of such high sample frequency, the sequence of the random digital counts doesn't act as 'random' anymore and so glitches appear in the measurements. The glitches in *v*-pol and *h*-pol channels are appeared independently so the actual measured correlation is lower.

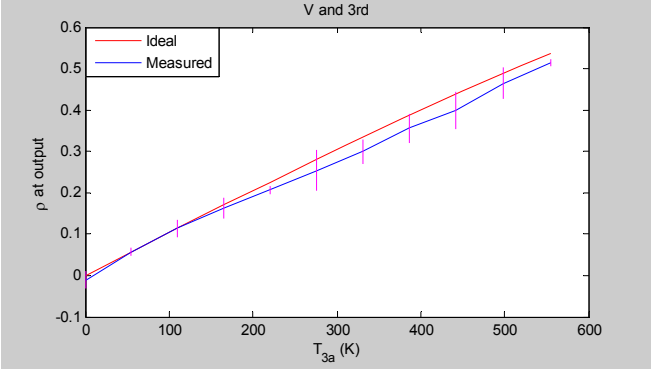

(a)

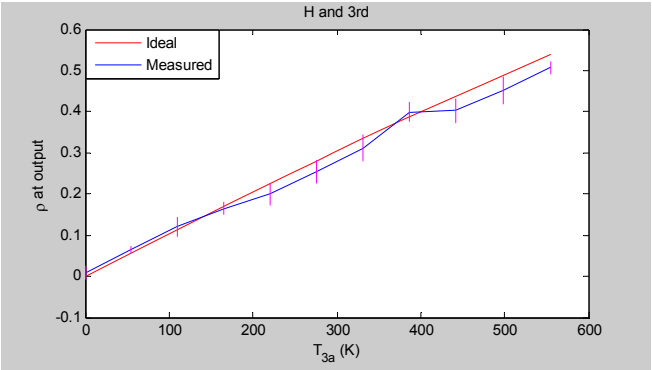

(b)

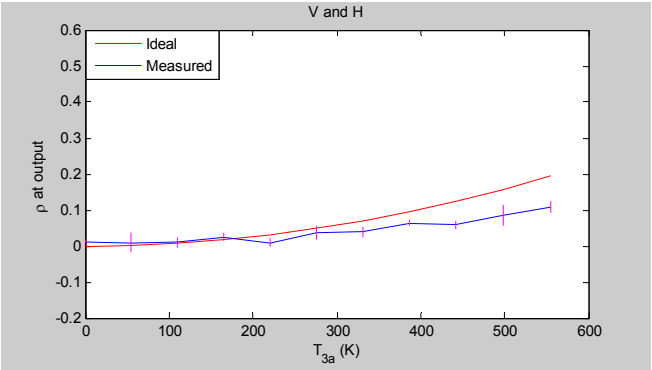

(c)

Figure 2.5 Correlation between the additive noise in (a) T_v and T_3, (b) T_h and T_3 and (c) T_v and T_h as a function of T_3. T_4 = 0 in each case. The theoretical values for the correlation are derived in Sections 2.2 and 2.3. The experimental values shown are averages over three independent trials. The error bars represent the standard deviation of the three trials.

2.6 Summary

The variance and correlation statistics of the additive noise component of fully polarimetric radiometer measurements with coherent or incoherent detection are derived from theoretical considerations and the resulting relationships are verified experimentally. It is found that the noise can be correlated among polarimetric channels and the correlation statistics will vary as a function of the polarization state of the scene under observation.

The precisions obtained from the two detections are compared. Analysis shows that if the square law detectors are the same and well known in the radiometer with incoherent detection, the precisions obtained from the two detection approaches will be the same, and the precisions are the same for the multiple methods to obtain the third (or fourth) Stokes brightness temperature from the measurements made by a hybrid combining polarimetric radiometer.

2.7 Original Contributions and Publication

The original contributions concerning the statistics of fully polarimetric radiometer measurements include

1) Noise covariance derivation for both the coherent and incoherent detection radiometer measurements;
2) Precision comparison between the two detection radiometers;
3) Precision comparison among the multiple options for the incoherent detection radiometer;
4) Experimental verification of the noise statistics of fully polarimetric radiometer measurements.
5) Derivation to show the differences in expressions of the 4th Stokes parameter in different coordinate systems for the incoherent detection approach. See Appendix 1.

One associated publication has been accepted:

1) J. Peng, and C. S. Ruf, "Covariance Statistics of Polarimetric Brightness Temperature Measurements," IEEE Trans. Geosci. Remote Sens., *in press*, accepted Mar 2008.

Chapter 3

Correlated Noise Calibration Standard (CNCS) Inversion Algorithm

The CNCS is developed for calibrating polarimetric radiometers. In order to accurately calibrate the radiometer, it is necessary to identify and quantify the non-ideal characteristics of the CNCS itself. To achieve that, parameterized forward models for both the CNCS and radiometer have been developed. A calibration algorithm estimates the parameters of the cascaded forward model from the radiometer measurements while the CNCS settings are varied over a suitable range. Simulations and demonstrations show that the calibration test set is efficient, and that the calibration algorithm can calibrate a fully polarimetric radiometer (receiver only) with high accuracy.

3.1 CNCS Overview

An X-Band version of the CNCS has been used previously to characterize the correlating receivers in the NASA/U-Michigan airborne Lightweight Rainfall Radiometer [52]. A new and improved L-band version [69-71] is to aid in the characterization of the Aquarius radiometers. A functional block diagram of the CNCS is shown in Figure 3.1 and a photo is shown in Figure 3.2. The system consists of a commercial Arbitrary Waveform Generator (AWG), a pair of frequency upconversion modulators with integral

calibration reference sources (referred to as the "RF Heads"), and a local oscillator which provides coherent LO signals for the two channels through a power divider.

The AWG is an Agilent model N6030A with fixed 1.25 GS/sec internal sample clock. It has two independent output channels with maximum analog bandwidths 500 MHz. The correlation between the pair of signals is determined by the values loaded into the look up tables of the AWG [51]. The values are converted into analog signals by a pair of 15-bit digital-to-analog converters (DACs) that are synchronously triggered by the internal sample clock. The strength of the analog signal exiting the DACs is adjusted by amplifiers with 3.3 dB of gain control. AWG signals can also be commanded on and off.

The AWG signals are coherently upconverted by the RF Head to the operating frequency of the Radiometer Under Test (RUT). The RF Head includes an ambient reference load and an active cold load (ColdFET) to correct for variations in AWG output power. They are housed in a thermally controlled environment with a typical temperature stability of 0.05^{o}C RMS over time scales of tens of minutes. The temperatures of the ambient and cold loads are continuously monitored to allow for temperature dependent corrections to their brightness temperatures. The ColdFET, which is a backward installed LNA [72], provides uncorrelated noise backgrounds for the output signal of each channel. To increase the electrical isolation between parts, isolators and attenuators are inserted in several places, as noted in Figure 3.1. A bandpass filter is also used in each RF Head to reduce unwanted RF and IF signal leakage between channels. This eliminates any significant cross-talk between the *v*- and *h*-pol channels and ensures that the degree of partial correlation between channels is due solely to the AWG programming.

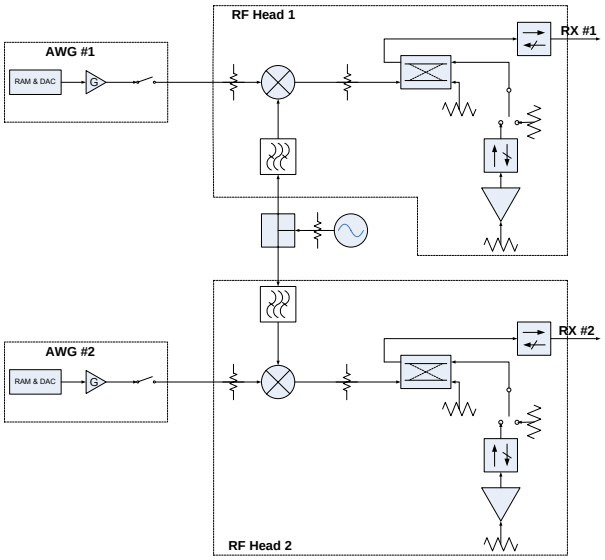

Figure 3.1 Functional block diagram of the CNCS

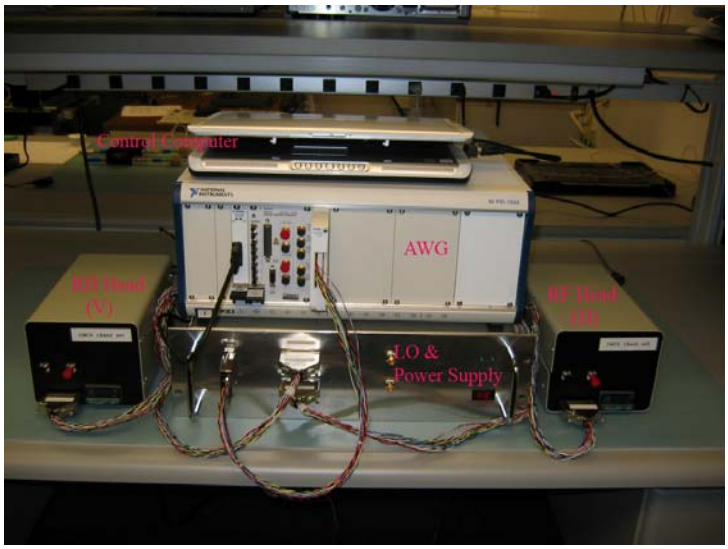

Figure 3.2 Photo of the L-band CNCS

3.2 CNCS Forward Model

The CNCS consists of several active components and numerous passive interconnects. There is a digital-to-analog converter and an amplifier inside the commercial AWG, and a mixer installed in the temperature controlled RF Head. These

components can be temperature sensitive and cause drifts in the strength of the CNCS output signals. In addition, the correlation between CNCS signals is related to the phase imbalance between its channels. All of these non-ideal properties could lead to calibration errors if not properly accounted for. To achieve this goal, a parameterized forward mode for radiative transfer through the CNCS is developed to represent the relationship between its user-controlled settings and the signals that it injects into the RUT. The strength of the signal generated by the AWG is controlled in two ways. The relative signal level over time is determined by the numerical values that are loaded into its software look up table. The look up table defines a normalized version of the signal. The absolute signal strength is determined by an AWG voltage gain setting, G. The gain setting can be varied in software from 0.17 to 0.25. This amounts to a variation in the AWG output power of 3.3 dB. Variations in the AWG output power have been verified, using a high precision power meter, to be linearly related to G^2 to better than 99.986%.

Signals generated by the CNCS contain one component generated by the AWG and a second component originating from either an ambient matched load or an active cold load. The brightness temperature of the AWG signal, referenced to the output of the RF Head, can be expressed as

$$T_{awg} = k\left(G^2 T_n + O_{awg}\right) \tag{3.2.1}$$

where k is scale factor used to represent gain imbalance between the two CNCS channels. G is the voltage gain of the AWG channel. T_n = 4480 Kelvin is the nominal brightness temperature generated by the AWG, and O_{awg} is a possible offset brightness temperature.

The total brightness temperature of each individual CNCS channel is the sum of the AWG component plus that of either the ambient load or active cold load. If the two

CNCS channels are used as inputs to the vertical and horizontal polarization channels of a fully polarimetric radiometer, then the quadrature components of correlation between them will represent the third and fourth Stokes parameters. Decorrelation between the two CNCS channels due to differences in the phase of the transfer functions is assumed to be negligible when used to calibrate the L-Band radiometers under test considered here because the radiometers' RF bandwidths are considerably narrower than that of the signal path through the RF Heads of the CNCS. It should be noted that this simplifying assumption may not be the case when calibrating a radiometer with a much wider bandwidth.

The complete CNCS forward model is given by

$$\begin{aligned} T_v &= k_v(G_v^2 T_n + O_{awg,v}) + T_{y,v} \\ T_h &= k_h(G_h^2 T_n + O_{awg,h}) + T_{y,h} \\ T_3 &= 2 \cdot \sqrt{k_v(G_v^2 T_n + O_{awg,v}) \cdot k_h(G_h^2 T_n + O_{awg,h})} \cdot \rho \cos(\theta + \Delta) \\ T_4 &= 2 \cdot \sqrt{k_v(G_v^2 T_n + O_{awg,v}) \cdot k_h(G_h^2 T_n + O_{awg,h})} \cdot \rho \sin(\theta + \Delta) \end{aligned} \tag{3.2.2}$$

k_v and k_h may differ to account for possible gain imbalances between the vertical and horizontal channels, G_v and G_h are the voltage gains of the respective AWG channels, $O_{awg,v}$ and $O_{awg,h}$ are the offsets of the AWG channels, ρ and θ are the magnitude and phase of the correlation coefficient between the two channels, Δ is the electrical path length imbalance between the two CNCS channels (resulting in a phase offset in the correlation, where a positive value for Δ means that the electrical path length of the *h*-pol channel is longer than that of the *v*-pol channel), and *y* = *ambient* or *cold* designates the background reference load selected in the RF Head. User-determined parameters of the CNCS forward model include the AWG gain settings (G_v, G_h), and the complex correlation coefficient (ρ, θ). The non-ideal parameters of the forward model, which need

to be determined as part of the calibration procedure, are the gain imbalances (k_v, k_h), the AWG channel offsets ($O_{awg,v}$, $O_{awg,h}$), and the inter-channel phase imbalance, Δ.

3.3 Polarimetric Radiometer Forward Model

The forward model for a fully polarimetric radiometer describes the relationship between the raw data recorded by the radiometer and the input Stokes parameters in brightness temperature. The model accounts for the net cascaded gain of individual polarization channels, unwanted but unavoidable cross-coupling between the channels, and measurement offsets that are not due to the input Stokes parameters (*e.g.* from internally generated receiver noise and detector biases).

Calibration of a radiometer consists of determining each parameter in its forward model. What forward model to use depends on the particular radiometer type. Examples of forward models appropriate for several coherent and incoherent detection radiometer architectures are considered here for illustrative purposes.

For a fully polarimetric radiometer that uses incoherent detection, the forward model is given by

$$\begin{pmatrix} C_v \\ C_h \\ C_P \\ C_M \\ C_L \\ C_R \end{pmatrix} = \begin{pmatrix} G_{vv} & G_{vh} & G_{v3} & G_{v4} \\ G_{hv} & G_{hh} & G_{h3} & G_{h4} \\ G_{Pv} & G_{Ph} & G_{P3} & G_{P4} \\ G_{Mv} & G_{Mh} & G_{M3} & G_{M4} \\ G_{Lv} & G_{Lh} & G_{L3} & G_{L4} \\ G_{Rv} & G_{Rh} & G_{R3} & G_{R4} \end{pmatrix} \cdot \begin{pmatrix} T_v \\ T_h \\ T_3 \\ T_4 \end{pmatrix} + \begin{pmatrix} O_v \\ O_h \\ O_P \\ O_M \\ O_L \\ O_R \end{pmatrix} \tag{3.3.1}$$

where C_x for $x = v, h, P, M, L$ and R are the raw radiometer measurement "counts" for each of its six polarimetric channels, T_y for $y = v, h, 3$ and 4 are the input Stokes parameters, G_{xy} are the gain matrix elements that relate input signals to output

measurements, and O_x are offsets in the measurements that are not related to the input signals.

The 30 unknown parameters that need to be determined in this forward model are G_{xy} and O_x. For the Aquarius radiometer, since there are no left- and right-hand circular polarization channels, the appropriate forward model is a simplified version of (3) that omits C_x, O_x, and G_{xy} for $x = L$ and R and $y = v, h, P, M, L$ and R. In this case, there would only be 20 unknown parameters to be determined. Note that the input signal, T_4, cannot be omitted since it can still influence the measurements if there is any polarization leakage present.

The forward model for a fully polarimetric radiometer that uses coherent detection is given by [49]

$$\begin{pmatrix} C_v \\ C_h \\ C_3 \\ C_4 \end{pmatrix} = \begin{pmatrix} G_{vv} & G_{vh} & G_{v3} & G_{v4} \\ G_{hv} & G_{hh} & G_{h3} & G_{h4} \\ G_{3v} & G_{3h} & G_{33} & G_{34} \\ G_{4v} & G_{4h} & G_{43} & G_{44} \end{pmatrix} \begin{pmatrix} T_v \\ T_h \\ T_3 \\ T_4 \end{pmatrix} + \begin{pmatrix} O_v \\ O_h \\ O_3 \\ O_4 \end{pmatrix} \tag{3.3.2}$$

There are 20 unknown parameters (G_{xy} and O_x) to be determined in this case. If the radiometer uses coherent detection without a fourth Stokes channel (*i.e.* measures only the in-phase component of the correlation between *v*- and *h*-pol signals), then the forward model will be a simplified version of (3.3.2) in which C_4, G_{4y} and O_4 for $y = v$, h, 3 and 4 are omitted. In this case, there would be 15 unknown parameters to be determined. This last case applies to the benchtop radiometer that has been used to experimentally validate the performance of the new L-Band CNCS, the results of which are presented in Section 3.6, below.

3.4 Inversion Algorithm

The forward models for both the CNCS and radiometer can be combined together into a single composite forward model which relates the desired brightness temperatures that are programmed into the CNCS to the output digital counts that are measured by the RUT. In order to simultaneously retrieve both the gain matrix and offsets of the radiometer together with the CNCS forward model parameters, a suitable set of test data is required. The test data are generated by varying CNCS software settings (ρ, θ, G_v and G_h in Equation 3.2.2) and hardware switch positions (AWG signal either on or off, background TB source either ambient or cold load). The complete combination of CNCS settings that is used is listed in Table 3.1.

The test vectors t_1, t_4, t_7, t_{10} and t_{13} are signals from the AWG and are added onto the ColdFET. Those test vectors are linearly independent of each other and are varied with different strength, correlation coefficient magnitude and phase. Certain characteristics of the Stokes brightness temperature entering the RUT are a function of the 4 variables: 1) the strength of each channel; 2) the correlation coefficient magnitude; and 3) the phase), so 5 linearly independent test vectors are the minimum that is required. Because the CNCS is not ideal and the signal strength from the AWG is unknown, 2 additional test vectors with known but different brightness temperatures are required to calibrate the signal strength of the CNCS channels while it is being used to calibrate the RUT. The 2 additional test vectors are t_2 and t_3 (or t_5 and t_6, …. Here, t_2 is the same as t_5 and t_3 is the same as t_6, and so on.) .

There is some redundancy of information provided by this set of test vectors. However, the precision and reliability of the retrieved forward model parameters are both

improved by over constraining the system of equations from which they are derived, so the redundancy is retained.

Table 3.1 CNCS Calibration Test Set

Test Vector	ρ	θ	G_v	G_h	AWG signal	Background TB
t_1	0	0	0.17	0.17	on	cold
t_2	0	0	0.17	0.17	off	cold
t_3	0	0	0.17	0.17	off	ambient
t_4	0	0	0.25	0.17	on	cold
t_5	0	0	0.25	0.17	off	cold
t_6	0	0	0.25	0.17	off	ambient
t_7	0	0	0.17	0.25	on	cold
t_8	0	0	0.17	0.25	off	cold
t_9	0	0	0.17	0.25	off	ambient
t_{10}	1	0	0.25	0.25	on	cold
t_{11}	1	0	0.25	0.25	off	cold
t_{12}	1	0	0.25	0.25	off	ambient
t_{13}	1	45°	0.25	0.25	on	cold
t_{14}	1	45°	0.25	0.25	off	cold
t_{15}	1	45°	0.25	0.25	off	ambient

All elements of the radiometer gain matrix and measurement offset, and all parameters of the CNCS forward model except for its channel phase imbalance, Δ, can be satisfactorily estimated from the measurements using an over-constrained, nonlinear, iterative minimization method. The dependence of the channel phase imbalance on the test settings is not sufficiently unique, relative to the other parameters, to be retrievable by inversion of the complete forward model given a calibration dataset that can be generated automatically. (Many of the characterization tests that are enabled by the CNCS become extremely laborious if the calibration test set is not automatically generated.) The CNCS channel phase imbalance must be estimated by manually cross-

swapping the interconnecting cables between the CNCS and the radiometer under test. This is the one step in the calibration procedure that is not fully automated. Fortunately, the channel phase imbalance has, in practice, been found to be extremely stable over time and so not in need of frequent recalibration.

The complete set of unknown parameters in the composite forward model for both the CNCS and RUT can be combined together into a single unknown vector, $\overline{X}$, given by

$$\overline{X} = \{ k_v,\ k_h,\ O_{awg,v},\ O_{awg,h},\ \Delta,\ G_{mn} \text{ and } O_m \} \tag{3.4.1}$$

where *m = v, h, P, M, L, R* for an fully polarimetric incoherent detection radiometer, while *m = v, h, 3* and *4* for a fully polarimetric coherent detection radiometer, and *n = v, h*, *3* and *4* in either case. The individual elements of $\overline{X}$ are defined in Equation (3.3.1) and (3.3.2). All of the radiometer measurements made during the calibration test can be similarly combined into a measurements vector, $\overline{C}$, given by

$$\overline{C} = f(\overline{X}) \tag{3.4.2}$$

where each element of $\overline{C}$ is the measurement count for one of the six polarimetric radiometer channels at one of the fifteen CNCS settings listed in Table 3.1, and where *f* represents the complete forward model.

The estimation of $\overline{X}$ given $\overline{C}$ is performed by inverting Equation (3.4.2) using the iterative Newton-Raphson method. Specifically, a first guess at $\overline{X}$ is made, denoted by $\hat{\overline{X}}$. The Jacobian matrix, *J*, of partial derivatives of *f* with respect to elements of $\overline{X}$ evaluated at $\hat{\overline{X}}$ is next computed numerically. An updated estimate of $\hat{\overline{X}}$ is then made according to

$$\hat{\bar{X}}' = \hat{\bar{X}} + \left(J^T \cdot J\right)^{-1} \cdot J^T \cdot \left(\bar{C} - f(\hat{\bar{X}})\right) \tag{3.4.3}$$

where superscript *T* denotes transpose.

This process is iterated until changes in $\hat{\bar{X}}$ become vanishingly small and $\hat{\bar{X}}$ has converged to that value which minimizes the norm-squared difference between $\bar{C}$ and $f(\hat{\bar{X}})$. Determining the parameters of the RUT forward model is equivalent to calibrating it.

The CNCS channel phase imbalance, Δ, is determined by manually cross-swapping the interconnecting cables between the CNCS and the radiometer under test. When cross-swapped, CNCS output port V is connected to the radiometer input channel H, and CNCS output port H is connected to the radiometer input channel V. Cross-swapping changes the sign, but not the magnitude , of Δ in the CNCS forward model. In both the standard and cross-swapped position, their radiometer parameters that are retrieved should be the same since the radiometer itself has not changed. Some of the radiometer parameters (e.g. G_{vv} and G_{hh}) are not sensitive to either the radiometer or the CNCS phase imbalance. Other of the parameters (e.g. G_{P3} and G_{P4}, or G_{M3} and G_{M4}, etc in Equation (3.3.1), or G_{33} and G_{34}, etc in Equation (3.3.2)) are sensitive to the CNCS phase imbalance and so will vary with Δ. Using both the standard and cross-swapped measurements, the assumed value of Δ is varied incrementally over all possible values and, for each value, a new estimate of G_{xy} (*x*=*P*, *M*, *L*, *R*, *3* or *4*; *y*=*3* or *4*) is made using the Newton-Raphson method. In this way, a value of Δ is found for which the retrieved estimate of G_{xy} (*x*=*P*, *M*, *L*, *R*, *3* or *4*; *y*=*3* or *4*) is the same in both the normal and cross-swapped cable positions. Two possible solutions are obtained in this manner and the

ambiguity is resolved using a prior knowledge of the CNCS component characteristics or other verification.

Once the gain matrix is known, the phase imbalance of the radiometer can be obtained directly from G_{x3} and G_{x4} (x=*P*, *M*, *L*, *R*, *3* or *4*) by

$$\Delta\phi = \begin{cases} \sin^{-1}\left(\dfrac{G_{x4}}{\sqrt{G_{x3}^2 + G_{x4}^2}}\right) & if \quad G_{x3} \geq 0 \\ 180^0 - \sin^{-1}\left(\dfrac{G_{x4}}{\sqrt{G_{x3}^2 + G_{x4}^2}}\right) & if \quad G_{x3} < 0 \end{cases} \tag{3.4.4}$$

The phase imbalances of the radiometer might be 180° different using different polarization channels. This is because the 2 hybrid coupler outputs are 180° different.

3.4.1 Necessity of the Cable Swapping

The CNCS channel phase imbalance, Δ, can not be retrieved simultaneously with other unknown parameters, and this is shown below.

The radiometer outputs can be represented by the following equation which is a simplified version from the CNCS and radiometer forward models (3.2.2) and (3.3.1).

$$C_{x,m} = f_{x,m} + G_{x3}T_{cc,m}\cos(\theta_m + \Delta) + G_{x4}T_{cc,m}\sin(\theta_m + \Delta) \tag{3.4.5}$$

where $x = v, h, P, M, L$ and R stand for the radiometer polarization channel x;

m = 1, 2, …, or 15 is the index of test vector in Table 3.1;

$f_{x,m}$ is the sum of all the terms except the terms containing G_{x3} and/or G_{x4};

and

$$T_{cc} = 2 \cdot \sqrt{k_v(G_v^2 T_n + O_{awg,v}) \cdot k_h(G_h^2 T_n + O_{awg,h})} \cdot \rho \tag{3.4.6}$$

In the Jacobian matrix in Equation (3.4.3), the columns with partial derivatives of $C_{x,m}$ with respect to G_{x3} and G_{x4} are individually given by

$$\frac{\partial C_{x,m}}{\partial G_{x3}} = T_{cc,m}\cos(\theta_m + \Delta) I_{6\times 6} \tag{3.4.7a}$$

$$\frac{\partial C_{x,m}}{\partial G_{x4}} = T_{cc,m}\sin(\theta_m + \Delta) I_{6\times 6} \tag{3.4.7b}$$

The column with partial derivatives of $C_{x,m}$ with respect to the CNCS channel phase imbalance, Δ, is given by

$$\frac{\partial}{\partial \Delta}\begin{bmatrix} C_{v,m} \\ C_{h,m} \\ C_{P,m} \\ C_{M,m} \\ C_{L,m} \\ C_{R,m} \end{bmatrix} = -\begin{bmatrix} G_{v3} \\ G_{h3} \\ G_{P3} \\ G_{M3} \\ G_{L3} \\ G_{R3} \end{bmatrix} T_{cc,m}\sin(\theta_m + \Delta) + \begin{bmatrix} G_{v4} \\ G_{h4} \\ G_{P4} \\ G_{M4} \\ G_{L4} \\ G_{R4} \end{bmatrix} T_{cc,m}\cos(\theta_m + \Delta) \tag{3.4.8a}$$

or

$$\frac{\partial}{\partial \Delta}\begin{bmatrix} C_{v,m} \\ C_{h,m} \\ C_{P,m} \\ C_{M,m} \\ C_{L,m} \\ C_{R,m} \end{bmatrix} = -\left(\frac{\partial C_{x,m}}{\partial G_{x3}}\right)\begin{bmatrix} G_{v3} \\ G_{h3} \\ G_{P3} \\ G_{M3} \\ G_{L3} \\ G_{R3} \end{bmatrix} + \left(\frac{\partial C_{x,m}}{\partial G_{x4}}\right)\begin{bmatrix} G_{v4} \\ G_{h4} \\ G_{P4} \\ G_{M4} \\ G_{L4} \\ G_{R4} \end{bmatrix} \tag{3.4.8b}$$

Since the radiometer gain matrix elements are independent on the test vector, the column with partial derivatives of $C_{x,m}$ with respect to Δ is linearly dependent on the columns of $C_{x,m}$ with respect to G_{x3} and G_{x4}. That means the Jacobian matrix in Equation (3.4.3) is not fully ranked if the CNCS channel phase imbalance, Δ, is considered unknown during the pseudo-inversion.

3.4.2 Estimated Performance using a Simulation with the Regular Test Set

To evaluate the CNCS inversion algorithm, a Monte-Carlo simulation is conducted with variable integration time. The parameters of the CNCS and the RUT are listed in Table 3.2. The gain matrix used is for the NASA Goddard Airborne Earth Science Microwave Imaging Radiometer (AESMIR) calibrated by the X-band CNCS in 2004 [68] and the receiver noise temperatures have been calculated from those earlier measurements. The offsets in Equation (3.3.1) are assumed to be from the receiver noise temperature only.

Table 3.2 Parameters of the CNCS and the RUT used in Monte-Carlo simulation

Device	Name	Value
CNCS	Channel gain imbalance	1.083 (v) 0.980 (h)
	Channel offset	8.320 K (v) 6.843 K (h)
	Channel phase imbalance	-21.581°
	ColdFET	85.495 K (v) 89.989 K (h)
	Reference load	293 K (v & h)
RUT	Gain matrix (units: mV/K)	12.679 0 0 0 0 9.177 0 0 5.277 5.641 5.409 -0.015 5.626 6.015 -5.987 -0.016 6.156 5.923 -0.196 6.435 5.907 5.683 -0.188 -5.978
	Receiver noise temperature	556.337 K (v) 618.477 K (h)

The Monte-Carlo simulation process is shown in Figure 3.3. The values of the voltage gain control, G_v & G_h, of the CNCS channels, the correlation coefficient magnitude, ρ, and phase, θ, are varied to generate a complete Stokes brightness

temperature test set $\{T_x: x = v, h, 3 \& 4\}$ (see Table 3.1 for the values of G_v G_h, ρ and θ). The outputs from the radiometer model are noise-free. To simulate the true output of a radiometer, correlated noise is added to the outputs to simulate the radiometer measurements (see Radiometer Outputs in Figure 3.3). The correlated noise is calculated by using Equations (2.2.9), (2.4.3) and Equations in [51]. Using the inversion algorithm, retrieved CNCS and radiometer models are obtained.

At the beginning of the Monto-Carlo simulation, two tests are performed to investigate whether there is more than 1 solution for a given set of measurements. First the initial values of all unknown parameters except the CNCS channel phase imbalance are randomly selected over a physically reasonable range — for example, k_v can not be negative or the AWG brightness of *v*-pol channel will be negative. Results of 1000 such trials show that the retrieval results are independent of the initial assignment to the unknown parameters. Second, the value of an unknown parameter is varied over a physically possible range about its true value (as listed in Table 3.2) while the values of the other unknown parameters are held constant. The radiometer outputs with and without a varied parameter are compared and the RMS error is calculated. If there is a single minimum error solution for the CNCS and the radiometer parameters, then the RMS error as a function of the varied parameter should have a signal minimum and it should increase monotonically as the value of the parameter is varied away from its true value. This test is no tall-inclusive of all possible parameter values in the solution space, but it helps to increase the credibility that there are not multiple solutions. All of the 34 unknown parameters were varied individually in this way and the results indicate that there is only one minimum error solution.

To evaluate the performance of the retrieval, the simulated measurements (see Radiometer Outputs in Figure 3.3) and the retrieved radiometer model are used to estimate the Stokes brightness temperatures at the radiometer inputs. The estimated Stokes brightness temperatures are denoted as $\{T_x'$: $x = v, h, 3 \& 4\}$. They are compared with the input Stokes brightness temperatures $\{T_x$: $x = v, h, 3 \& 4\}$ and their RMS errors are shown in Figure 3.4. The integration time is defined as the dwell time of each CNCS status. Each simulation is repeated 1000 times.

The RMS errors in the Stokes brightness temperatures are calculated by

$$\delta_x = \sqrt{\frac{\sum_1^n \left(T_{x,n} - T'_{x,n}\right)^2}{n}} \qquad \text{for } x = v, h, 3 \& 4 \tag{3.4.9a}$$

where n is the number of the corresponding Stokes brightness temperature.

The 'avg' in Figure 3.4 is calculated by

$$\delta_{avg} = \sqrt{\frac{\sum_1^n \left(T_{v,n} - T'_{v,n}\right)^2 + \sum_1^n \left(T_{h,n} - T'_{h,n}\right)^2 + \sum_1^n \left(T_{3,n} - T'_{3,n}\right)^2 + \sum_1^n \left(T_{4,n} - T'_{4,n}\right)^2}{4n}} \tag{3.4.9b}$$

The CNCS channel phase imbalance is retrieved by cross-swapping the CNCS output cables. In both cases, the radiometer channel phase imbalances are assumed unchanged. In that case, the retrieved precision of the radiometer channel phase imbalance is that of the CNCS channel phase imbalance. The results are shown in Figure 3.5.

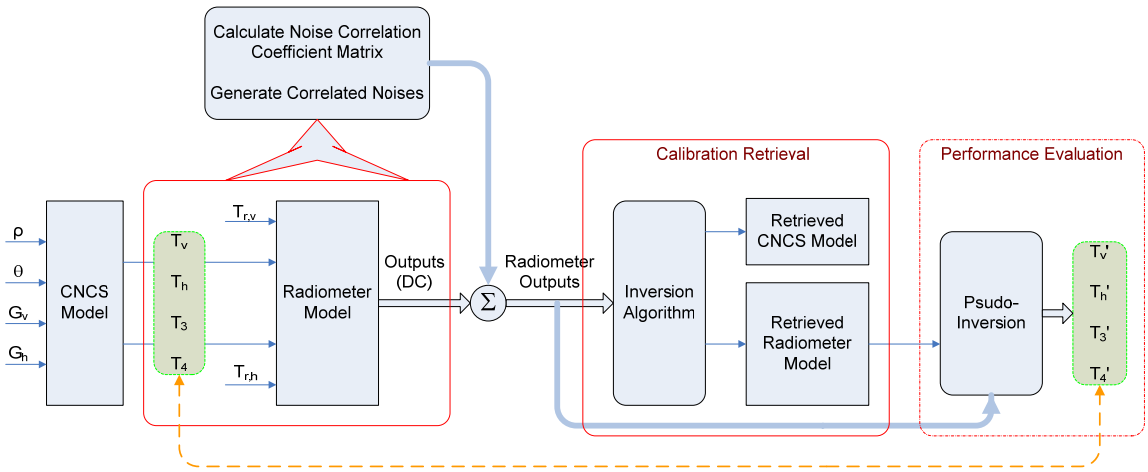

Figure 3.3 Simulation process for the performance evaluation of the inversion algorithm

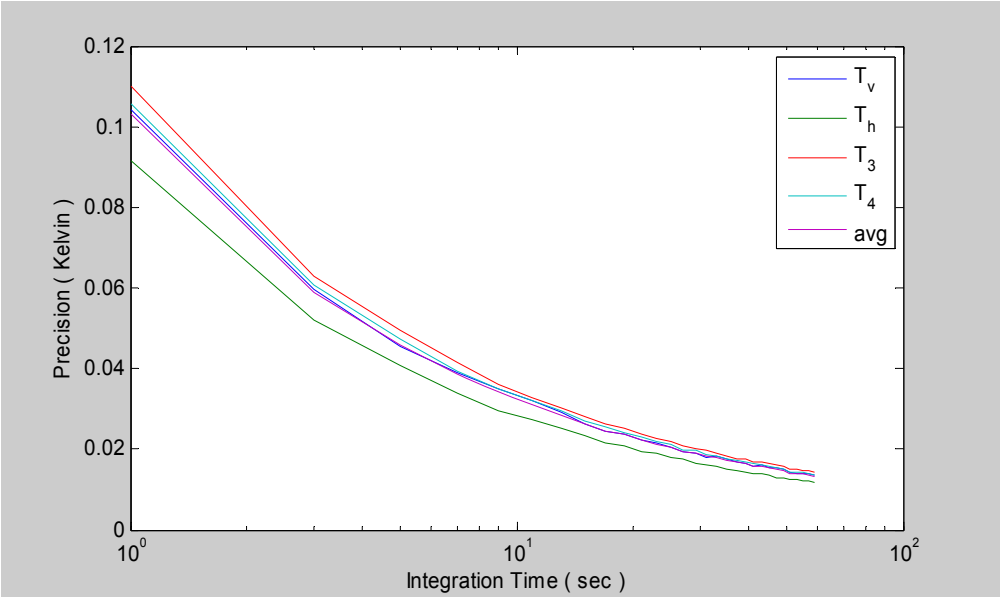

Figure 3.4 Performance evaluation of the inversion algorithm

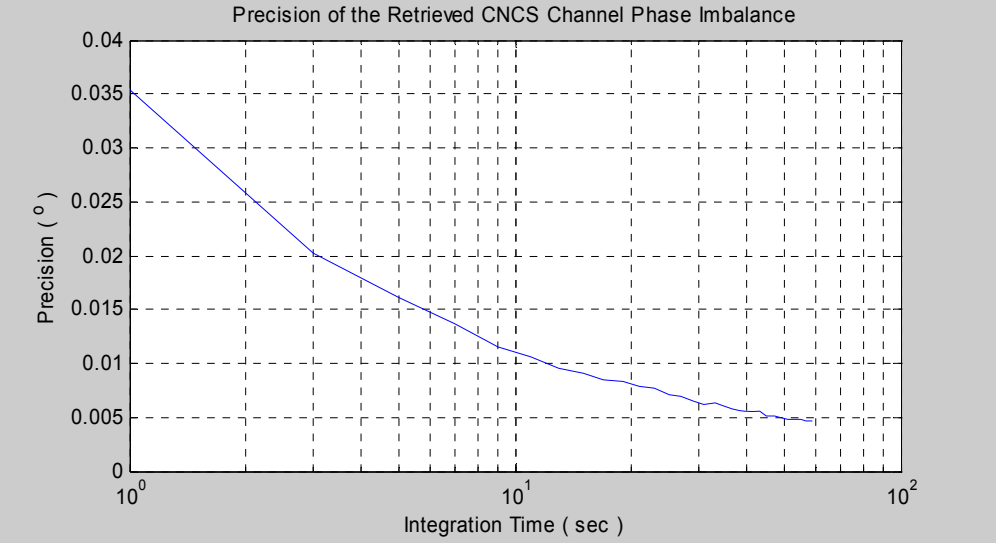

Figure 3.5 Precision of the Retrieved CNCS Channel Phase Imbalance

Another simulation is done to examine the correlation between the retrieved parameters to check if there are enough variations in the calibration data set to decouple the solutions for the parameters. Uncorrelated noise was added to the radiometer channel outputs and a Monte-Carlo simulation was conducted. The correlation coefficients between the retrieved parameters are shown in Table 3.3 (only the lower triangle is shown; the upper triangle is symmetric with respect to the diagonal), and the histogram of the correlation coefficients is shown in Figure 3.6. Most of the magnitudes of the correlation coefficients are less than 0.2 and none of them are totally correlated. Results show that the calibration data set is a complete data test.

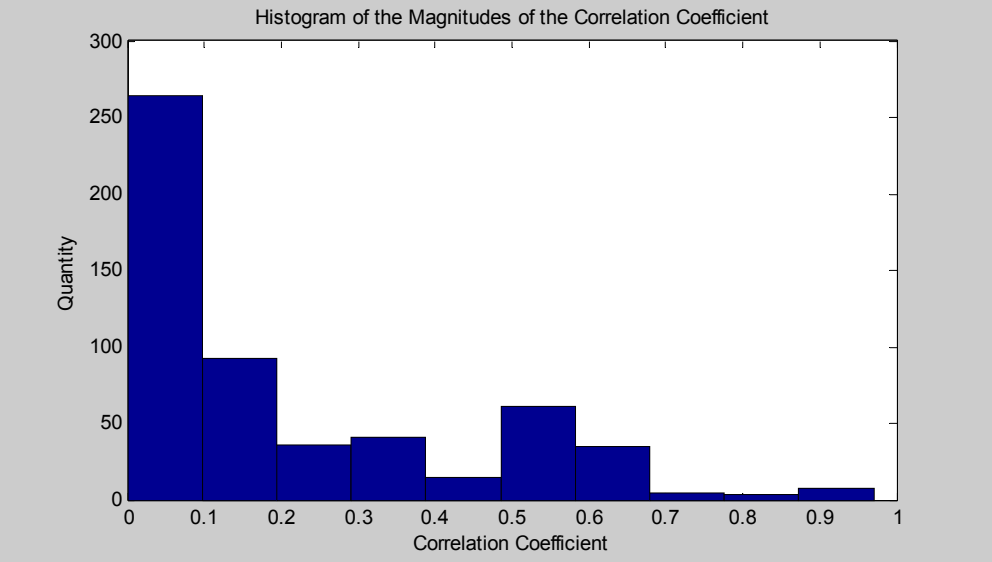

Figure 3.6 Histogram of the magnitudes of the correlation coefficients

Table 3.3 Correlation Coefficient between the Retrieved Parameters

	k_v	k_h	$O_{awg,v}$	$O_{awg,h}$	G_{vv}	G_{vh}	G_{v3}
k_v	1						
k_h	-0.50	1					
$O_{awg,v}$	-0.97	0.48	1				
$O_{awg,h}$	0.49	-0.97	-0.50	1			
G_{vv}	-0.79	0.37	0.75	-0.36	1		
G_{vh}	0.77	-0.37	-0.77	0.37	-0.95	1	
G_{v3}	-0.55	0.26	0.50	-0.23	0.38	-0.40	1
G_{v4}	-0.52	0.28	0.49	-0.27	0.38	-0.42	-0.13
O_v	0.05	0.02	-0.01	-0.04	-0.15	-0.13	0.04
G_{hv}	-0.38	0.78	0.38	-0.79	0.28	-0.29	0.19
G_{hh}	0.40	-0.80	-0.38	0.77	-0.29	0.29	-0.21
G_{h3}	0.29	-0.54	-0.26	0.50	-0.25	0.22	-0.14
G_{h4}	0.23	-0.53	-0.21	0.48	-0.17	0.16	-0.13
O_h	-0.13	0.22	0.13	-0.19	0.08	-0.08	0.08
G_{Pv}	-0.67	0.64	0.63	-0.64	0.51	-0.50	0.38
G_{Ph}	0.65	-0.65	-0.63	0.64	-0.50	0.49	-0.36
G_{P3}	-0.27	-0.27	0.25	0.24	0.23	-0.22	0.16
G_{P4}	-0.06	-0.12	0.06	0.10	0.05	-0.05	0.05
O_P	-0.05	0.09	0.07	-0.08	0.00	-0.02	-0.01
G_{Mv}	-0.67	0.66	0.65	-0.65	0.50	-0.48	0.36
G_{Mh}	0.64	-0.66	-0.63	0.64	-0.49	0.47	-0.35
G_{M3}	0.20	-0.05	-0.18	0.07	-0.15	0.15	-0.11
G_{M4}	-0.17	-0.14	0.16	0.13	0.14	-0.15	0.17
O_M	0.00	0.07	0.01	-0.06	0.01	-0.03	-0.02
G_{Lv}	-0.68	0.65	0.65	-0.65	0.53	-0.51	0.35
G_{Lh}	0.64	-0.67	-0.63	0.66	-0.49	0.48	-0.34
G_{L3}	-0.15	-0.10	0.15	0.09	0.11	-0.12	0.07
G_{L4}	-0.23	-0.26	0.20	0.23	0.19	-0.17	0.16
O_L	0.03	0.10	-0.02	-0.09	-0.04	0.03	-0.02
G_{Rv}	-0.66	0.65	0.64	-0.64	0.52	-0.51	0.39
G_{Rh}	0.64	-0.65	-0.62	0.64	-0.51	0.50	-0.38
G_{R3}	-0.18	-0.13	0.16	0.12	0.17	-0.15	0.13
G_{R4}	0.10	-0.01	-0.08	0.03	-0.08	0.06	-0.08
O_R	-0.04	0.09	0.03	-0.08	0.07	-0.05	0.04

Table 3.3(cont.) Correlation Coefficient between the Retrieved Parameters

	G_{v4}	O_v	G_{hv}	G_{hh}	G_{h3}	G_{h4}	O_h	G_{Pv}	G_{Ph}
G_{v4}	1								
O_v	0.09	1							
G_{hv}	0.23	0.05	1						
G_{hh}	-0.24	-0.05	-0.95	1					
G_{h3}	-0.16	0.05	-0.46	0.41	1				
G_{h4}	-0.12	-0.02	-0.43	0.40	-0.11	1			
O_h	0.07	0.00	0.11	-0.38	0.01	-0.04	1		
G_{Pv}	0.35	-0.02	0.50	-0.49	-0.35	-0.32	0.12	1	
G_{Ph}	-0.35	-0.01	-0.49	0.50	0.35	0.32	-0.13	-0.94	1
G_{P3}	0.12	-0.04	-0.16	0.19	0.12	0.19	-0.11	0.00	-0.02
G_{P4}	0.05	-0.02	-0.10	0.10	0.06	0.06	0.01	-0.07	0.01
O_P	0.03	0.05	0.05	-0.06	-0.02	-0.03	0.02	-0.06	-0.25
G_{Mv}	0.34	-0.04	0.54	-0.55	-0.36	-0.35	0.17	0.56	-0.56
G_{Mh}	-0.33	0.03	-0.53	0.55	0.36	0.35	-0.17	-0.54	0.55
G_{M3}	-0.10	0.00	-0.02	0.02	0.02	-0.03	-0.03	-0.14	0.14
G_{M4}	0.05	0.01	-0.11	0.11	0.06	0.11	0.02	0.06	-0.05
O_M	0.02	0.02	0.06	-0.06	-0.04	-0.03	0.01	0.05	-0.05
G_{Lv}	0.37	-0.04	0.52	-0.52	-0.37	-0.32	0.14	0.59	-0.58
G_{Lh}	-0.34	0.01	-0.53	0.54	0.38	0.36	-0.16	-0.57	0.56
G_{L3}	0.07	0.00	-0.10	0.09	0.07	0.08	-0.02	-0.01	0.00
G_{L4}	0.11	-0.03	-0.17	0.19	0.13	0.15	-0.04	0.06	-0.02
O_L	-0.03	0.04	0.08	-0.08	-0.03	-0.12	0.04	0.01	-0.01
G_{Rv}	0.31	0.02	0.53	-0.53	-0.35	-0.32	0.13	0.58	-0.57
G_{Rh}	-0.30	0.00	-0.52	0.52	0.36	0.32	-0.14	-0.57	0.56
G_{R3}	0.07	-0.06	-0.12	0.14	0.05	0.11	-0.03	0.05	-0.03
G_{R4}	-0.03	0.04	0.01	-0.02	-0.01	-0.04	0.01	-0.03	0.02
O_R	0.01	-0.05	0.05	-0.06	-0.04	-0.03	0.03	0.02	-0.02

Table 3.3(cont.) Correlation Coefficient between the Retrieved Parameters

	G_{P3}	G_{P4}	O_P	G_{Mv}	G_{Mh}	G_{M3}	G_{M4}	O_M	G_{Lv}
G_{P3}	1								
G_{P4}	-0.40	1							
O_P	0.04	0.13	1						
G_{Mv}	0.01	-0.02	0.08	1					
G_{Mh}	0.01	0.04	-0.10	-0.94	1				
G_{M3}	-0.08	-0.04	-0.04	-0.17	0.05	1			
G_{M4}	0.19	0.05	0.00	-0.05	-0.02	-0.50	1		
O_M	-0.02	-0.05	0.04	-0.04	-0.25	0.20	0.14	1	
G_{Lv}	0.05	-0.04	0.04	0.59	-0.56	-0.09	-0.01	0.01	1
G_{Lh}	0.00	0.05	-0.03	-0.59	0.57	0.06	0.05	-0.02	-0.94
G_{L3}	0.13	0.07	0.04	0.06	-0.06	-0.06	0.07	0.03	-0.01
G_{L4}	0.28	0.08	-0.09	-0.01	0.04	-0.08	0.17	-0.05	-0.01
O_L	-0.11	-0.03	-0.03	0.05	-0.06	0.05	-0.08	0.02	-0.07
G_{Rv}	0.00	-0.01	0.06	0.59	-0.57	-0.14	0.04	0.02	0.58
G_{Rh}	0.02	0.02	-0.05	-0.57	0.56	0.12	-0.03	-0.03	-0.57
G_{R3}	0.19	0.08	-0.05	0.01	0.01	-0.02	0.06	-0.01	0.05
G_{R4}	-0.07	-0.06	0.03	-0.07	0.04	0.02	0.01	0.03	-0.05
O_R	-0.03	-0.01	-0.01	0.05	-0.06	0.02	-0.04	0.02	0.07

Table 3.3(cont.) Correlation Coefficient between the Retrieved Parameters

	G_{Lh}	G_{L3}	G_{L4}	O_L	G_{Rv}	G_{Rh}	G_{R3}	G_{R4}	O_R
G_{Lh}	1								
G_{L3}	-0.03	1							
G_{L4}	0.00	-0.40	1						
O_L	-0.23	0.06	0.02	1					
G_{Rv}	-0.57	0.01	0.04	0.03	1				
G_{Rh}	0.57	0.00	-0.01	-0.04	-0.94	1			
G_{R3}	-0.03	0.09	0.15	-0.02	-0.02	-0.05	1		
G_{R4}	0.04	-0.03	-0.08	0.02	-0.11	0.00	-0.55	1	
O_R	-0.08	-0.01	-0.04	0.05	-0.02	-0.27	0.16	0.20	1

3.4.3 Performance by Simulation with Varied Test Set

The size of the calibration data set is varied to check the change in performance of the retrieval. Two simulations were conducted. The first uses a larger data set volume, and the second uses the minimum size of the calibration data set.

The first simulation attempts to find the benefit due to an increase in size of the test vector. Integration time is varied as well to check its effect on the retrieved parameter precision comparing with the precision with the increased volume of test vectors only. Simulation results find that the retrieved performance is more dependent on the integration time than on the addition of test vector elements. This might be due to that the additional test vector is not totally independent to the other test vectors. This simulation includes 3 tests with different test set and/or integration time.

Test 1 used a test set exactly the same as that in Table 3.1 with integration time 1s, the time to take one set of measurements is 15s; test sets of Test 2 & 3 are the same. They are formed by adding additional 3 test vectors to the first test set and the 3 additional test vectors are the same as the test vectors t_{13}, t_{14} and t_{15} in Table 3.1, except that their correlation coefficient phases are 90°. The additional test vectors are listed in Table 3.4. Integration time is 1s for test 2 and 0.833s for test 3. Then the time to take one set of measurements is 18s for test 2 and 15s for test 3. Monte-Carlo simulation was taken 1000 times for each case, and the result is shown in Table 3.5.

Table 3.4 Additional test vectors for Test 2 & 3

Test Vector	ρ	θ	G_v	G_h	AWG signal	Background TB
t_{16}	1	90°	0.25	0.25	on	cold
t_{17}	1	90°	0.25	0.25	off	cold
t_{18}	1	90°	0.25	0.25	off	ambient

Table 3.5 Performance comparison with different test set and integration time

	RMS error				
	T_v (K)	T_h (K)	T_3 (K)	T_4 (K)	avg (K)
Test 1	0.104	0.092	0.110	0.106	0.103
Test 2	0.104	0.091	0.109	0.116	0.105
Test 3	0.111	0.098	0.120	0.125	0.114

From Table 3.5, it can be found that the results of Test 1 and 2 are almost the same, but that of Test 3 is about 8.2% worse than the others and this result is matched with the factor $1/\sqrt{\tau}$.

Reducing the size of the test set in Table 3.1 has also been explored. The redundant test vectors t_x (x=5, 6, 8, 9, 11, 12, 14 & 15) are removed, and the remaining test vectors form a minimum test set. The simulation result is shown in Figure 3.7. The average precision of the estimated Stokes brightness temperatures are 30% worse than that of the regular test set. This is because the precision of the calibration reference plane which separate the CNCS and the RUT is determined by the precision of the brightness temperatures of both of the CNCS ColdFET and the CNCS reference load. Less integration time will lead to worse retrieval precision.

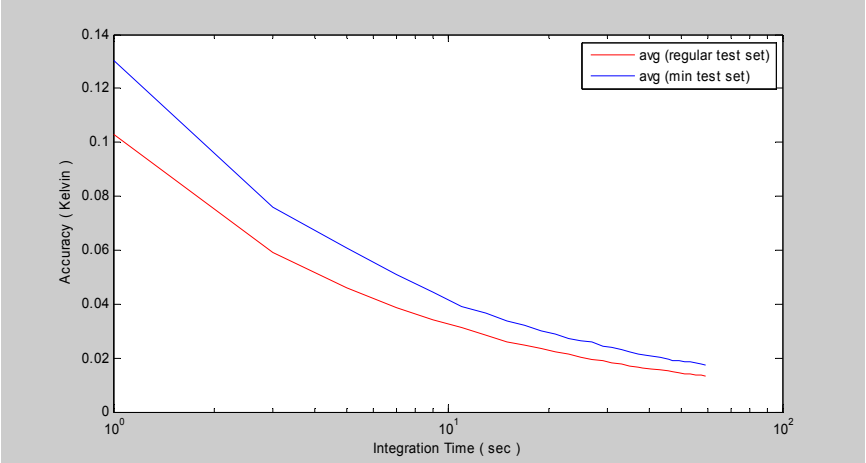

Figure 3.7 RMS uncertainty comparison between the estimated Stokes TBs with regular test set and that with minimum test set.

3.5 Antenna-Receiver Impedance Mismatching Correction

One correction to the CNCS & RUT forward model is necessary if the impedance match between it and the CNCS differs from the match with the antenna that would be connected in place of the CNCS during normal data taking. The impedance mismatch between the CNCS and RUT receiver has two potential effects – it can change the apparent brightness temperature of the CNCS active cold load and it can alter a number of the elements of the RUT's polarimetric gain matrix and offset vector, relative to what they would be when connected to an antenna with a different impedance match. Corrections for both of these effects are considered here. The impact of impedance mismatches between a radiometer receiver and its antenna on the digital counts measured by the radiometer has been addressed previously by Corbella *et al*. [57-59]. Their approach is adopted here, generalizing the input impedance mismatch to include that with the CNCS as well as the antenna. A detailed derivation of the corrections to the forward model parameters due to impedance mismatches is provided in the Appendix 4.

3.6 Calibration Procedure and Demonstration

A benchtop RUT, the DetMit radiometer, is introduced. The test procedures that were followed to calibrate the benchtop RUT with the CNCS, together with the resulting estimates of the parameters of the CNCS and RUT forward models and of their accuracy and precision, are described in this section.

3.6.1 L-band Correlating Polarimetric Radiometer

The DetMit radiometer was used to demonstrate the calibration methodology of the CNCS. Its system block diagram is shown in Figure 3.8. Input vertically and horizontally polarized signals are filtered and amplified, then coherently down-converted to an IF band. The IF signals are then processed by the Agilent Digital Detector (ADD) [73]. ADD digitizes the input signals and then implements digital signal processing operations to measure the Stokes parameters. The 1^{st} and 2^{nd} Stokes parameters are measured by their self-correlations of the input signals respectively while the third Stokes parameter is directly measured by their product. Matched loads connected to the input switches, together with a noise diode, are used for radiometer calibration. The noise diode's noise signal is divided by a Wilkinson power divider and coupled into the radiometer channels.

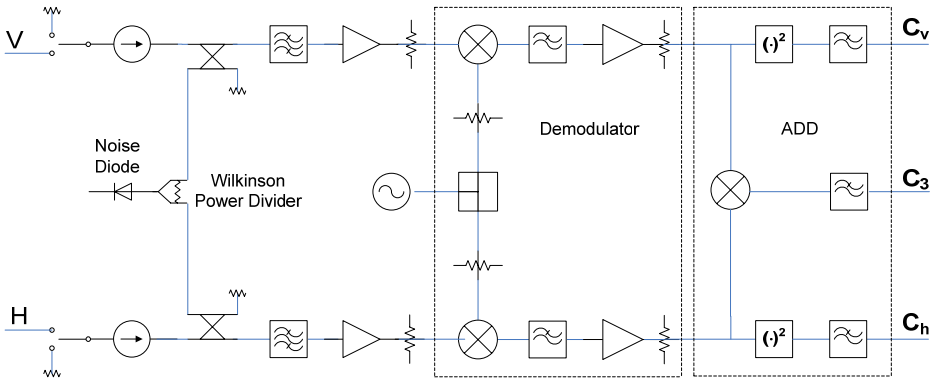

Figure 3.8 Simplified block diagram of the L-band radiometer

3.6.2 Radiometer Stability

The calibration test set consists of fifteen variations of the input signals generated by the CNCS (see Table 3.1). During the time over which the test set is generated, both the CNCS and radiometer forward models should not vary appreciably. The stability of the radiometer is determined from a long time series of measurements made while continuously observing the CNCS reference load (*i.e.* calibration test signal t_3 in Table 3.1) in its "total power" mode – without any calibration or corrections for gain variations. The Allan variance of the measurements is used to characterize the stability of the radiometer [74]. Figure 3.9 shows the derived Allan standard deviation of the radiometer measurements versus integration time for both the *v*-pol and *h*-pol channels. The minimum standard deviation occurs at an integration time of 30 seconds and 32 seconds for the *v*- and *h*-pol channels, respectively. Based on these results, a complete calibration data set should be completed in no more than 30 seconds. The results presented here are based on measurements made with a dwell time of 2 seconds on each of the fifteen calibration test settings.

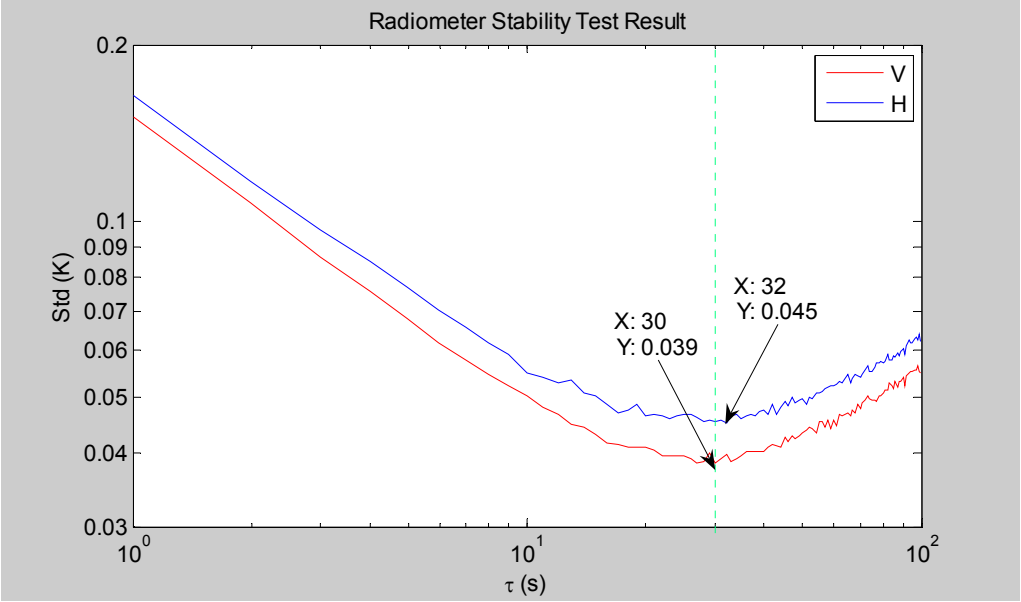

Figure 3.9 Allan standard deviation versus integration time of free running radiometer characterizes the inherent stability of the radiometer receiver.

3.6.3 CNCS Stability

CNCS stability is characterized using a similar Allan variance analysis, but with the radiometer observing a CNCS signal composed of an active cold load background to which an AWG signal is added that raises the brightness temperature to that of the ambient load. This choice is made under the assumption that the dominant source of drifting in the CNCS signal will be the stability of the AWG output signal strength. In order to remove the effects of drifts in radiometer gain, data are taken in a repeated cycle of the CNCS ambient load, cold load alone, and AWG + cold load (*i.e.* calibration test signals t_1, t_2 and t_3 in Table 3.1). Dwell time on each of these signals is 5 seconds. Adjacent ambient and cold load measurements are used to calibrate the radiometer for each AWG + cold load measurement in order to remove the effects of radiometer drift. Figure 3.10 shows the resulting Allan standard deviation of the calibrated AWG + cold

load time series versus integration time. The minimum standard deviations for both *v*- and *h*-pol channels occur at integration times of approximately 200 s. In the event that some other radiometers under test were more stable than the CNCS, 200 s would be the upper bound on the time during which a complete calibrate test set should be measured.

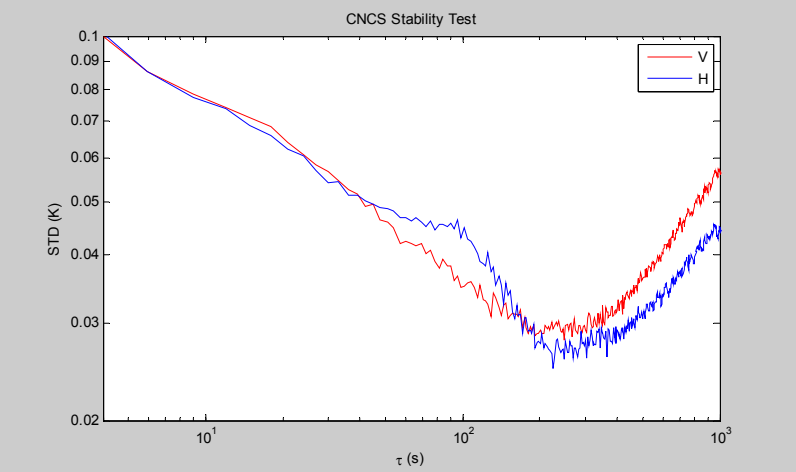

Figure 3.10 Allan standard deviation versus integration time of frequently recalibrated radiometer while viewing the CNCS AWG signal characterizes the inherent stability of the CNCS signal source.

3.6.4 CNCS ColdFET Calibration

The brightness temperature of the CNCS active cold loads was determined using ambient and LN_2 coaxial reference loads. The LN_2 load and temperature regulated coaxial cable is a precision Maury Microwave MT7118 system with ± 0.5 K uncertainty. Measurement of the LN_2 and ambient loads provides an absolute calibration of the radiometer under test. Subsequent measurement of the active load allows the calibration to be transferred to the active cold load. The brightness temperatures of the active cold loads are found in this way to be 87.6 K and 92.3 K for the *v*- and *h*-pol channels without correction for impedance mismatches, and 85.5 K and 90.0 K with the corrections

applied. This procedure has been repeated numerous times over periods of weeks and months and found to be repeatable at approximately the 1 K level. It should be noted that the brightness temperature of the active cold load should be recalibrated if a different RUT is used or if the passband characteristics of a RUT change significantly. This is because the brightness temperature of the reverse LNA at the heart of the active cold load is more frequency dependent than is a traditional LN_2 load and so the effective brightness temperature of the active cold load will be more dependent on the specific passband frequency response of a radiometer. In summary, the apparent brightness temperature of the CNCS active cold loads changes by 2.1 and 2.3 K for the *v*- and *h*-pol channels, respectively, due to the reflection of a small fraction of the RUT receiver noise temperature at the mismatched cold load interface. As a result of the high (~ 75 dB) isolation between *v*- and *h*-pol channels of the CNCS, elements of the RUT gain matrix require only insignificantly small corrections. However, the offset brightness temperatures, O_v and O_h in Equation (3.3.1) and (3.3.2), do require small but significant corrections.

3.6.5 CNCS Cable Cross-Swapping for Channel Phase Imbalance

The CNCS channel phase imbalance, Δ, is determined by manually cross-swapping the interconnecting cables between the CNCS and the radiometer under test. When cross-swapped, CNCS output port V is connected to radiometer input channel H, and CNCS output port H is connected to radiometer input channel V. Cross-swapping changes the sign, but not the magnitude, of Δ in the CNCS forward model. In both the standard and cross-swapped positions, the radiometer parameters that are retrieved should be the same since the radiometer itself has not changed. Some of the parameters (*e.g.* G_{vv}

and G_{hh}) are not sensitive to either the radiometer or the CNCS channel phase imbalance. Other parameters (*e.g.* G_{33}) are sensitive to the CNCS channel phase imbalance and so will vary depending on what value is assumed for Δ.

3.6.6 CNCS Forward Model Parameters Retrieval

The Newton-Raphson method is not able to estimate the CNCS channel phase imbalance, Δ, shown in Section 3.4.1 Necessity of the Cable Swapping with current CNCS configuration. It can, however, estimate all other of the CNCS and RUT forward model parameters if Δ is known. In order to solve for Δ, its assumed value is varied in step size of 0.001^{o} over all possible angles from 0 to 360^{o} and, for each value, all other CNCS and RUT parameters are estimated. This is repeated with both the standard and cross-swapped cable positions. The retrieved values of the RUT parameters should not be affected by the cable arrangement if the correct value for Δ is assumed. If, on the other hand, the wrong value for Δ is used, the retrieval of any phase sensitive parameters will be affected and their estimated values will not be the same for both the standard and cross-swapped cable positions. An example of this situation is shown in Figure 3.11. The retrieved value of the RUT forward model parameter G_{33} is shown as a function of the assumed value of Δ in both the standard and cross-swapped cable positions. (In the figure, G_{33} has been normalized by $(G_{vv}G_{hh})^{0.5}$ to reduce the effects of radiometer gain fluctuations that may have occurred during the test.) There are only two values of Δ for which the same value of G_{33} is retrieved. One of the two values is the correct one and the other is an ambiguity. The two values differ enough that the ambiguity can be easily resolved by comparing them to an approximate estimate of Δ based on network analyzer

measurements. The correct solution is $\Delta = -21.581°$. The negative value indicates that the electrical length of the *v*-pol channel is greater than that of the *h*-pol channel.

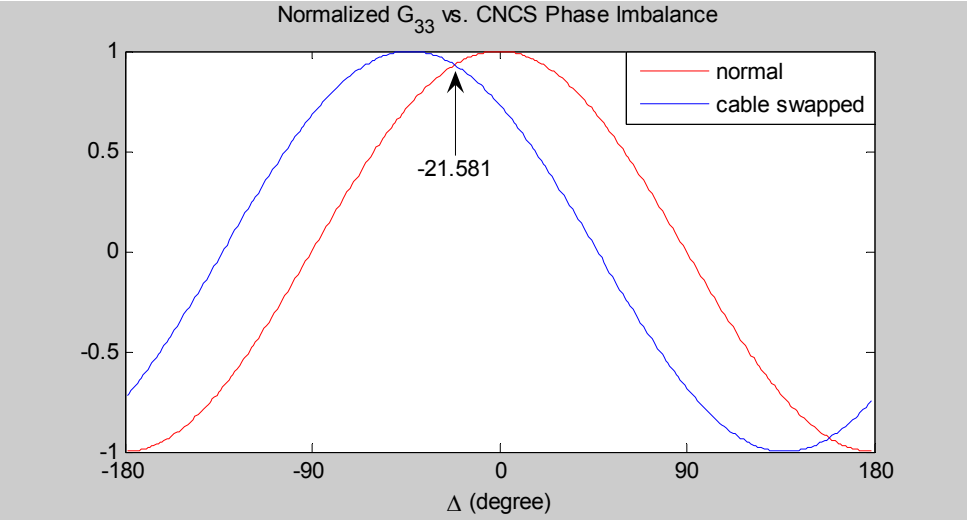

Figure 3.11 CNCS channel phase imbalance, Δ, is retrieved by swapping *v*- and *h*-pol interconnecting cables between the CNCS and radiometer under test. Only one unambiguous value of Δ produces the same estimate of the radiometer gain matrix element G_{33}.

Because normalized versions of G_{33} or G_{34} are used to derive the CNCS phase imbalance, cables do not need to be swapped within the time that G_{33} or G_{34} themselves are stable. This is confirmed by the fact that the channel phase imbalance has, in practice, been found to be extremely stable over time.

All other parameters of the CNCS forward model, beside the channel phase imbalance, are retrieved simultaneously with the parameters of the radiometer forward model during the Newton-Raphson process. Those parameters retrieved while the correct value for the CNCS channel phase imbalance is assumed are the correct ones. All parameters of the CNCS forward model are listed in Table 3.6. Monte Carlo simulation shows that the precision (*i.e.* RMS uncertainty) of the CNCS output is 0.18 K and 0.13 K

for the *v*- and *h*-pol channels, respectively. The precision of the CNCS channel phase imbalance is assumed to be the same as that of the radiometer phase imbalance, namely 0.020°.

Table 3.6. Retrieved CNCS Calibration Parameters

k_v (unitless)	k_h (unitless)	$O_{awg,v}$ (K)	$O_{awg,h}$ (K)	Δ (°)
1.083 ± 0.001	0.980 ± 0.001	8.320 ± 0.239	6.843 ± 0.238	-21.581

3.6.7 Radiometer Under Test Forward Model Parameters Retrieval

The retrieved polarimetric gain matrix and offsets of the RUT (as defined by (3.3.2)) are listed in

Table 3.7. The RMS errors in each parameter, as determined by a Monte Carlo simulation of the retrieval process, are also listed in the table. Only NEDT error is included in this simulation.

Table 3.7. Retrieved Radiometer Polarimetric Gain Matrix and Offset Vector

G_{xy} (Counts/K) and O_x (Counts)		***Input***				
		v-pol (Counts/K)	*h-pol* (Counts/K)	*3rd Stokes* (Counts/K)	*4th Stokes* (Counts/K)	*Offset* (Counts)
Output	*v-pol*	12.950 ± 0.010	-0.003 ± 0.010	0.009 ± 0.004	0.000 ± 0.004	3515.190 ± 0.520
	h-pol	-0.001 ± 0.008	11.779 ± 0.008	0.004 ± 0.003	-0.026 ± 0.003	3925.080 ± 0.441
	3rd Stokes	0.007 ± 0.003	0.010 ± 0.003	5.792 ± 0.003	2.269 ± 0.002	-31.810 ± 0.276

The accuracies of the estimated offsets are given in Counts. If the offsets are from the receiver noise temperatures, their equivalent accuracies in Kelvin will be 0.040 K,

0.037 K and 0.048 K, respectively, considering that their channel gains are 12.950, 11.779 and 5.792 Counts/K, respectively.

In order to evaluate the performance of the gain matrix elements retrieval, the simulated measurements and the retrieved radiometer gain matrix are used to estimate the Stokes TBs at the radiometer inputs. The simulated measurements are the product of the CNCS outputs and mean value of the Gain Matrix in

Table 3.7. CNCS outputs consist of the test vectors in Table 3.1 with CNCS model parameters in Table 3.6. Due to the fact that the radiometer has no 4th Stokes channel, the 4th Stokes TBs in the CNCS outputs are set to zero. The estimated 1st, 2nd and 3rd Stokes TBs at the radiometer inputs can be obtained from the measurements in Table 3.1. The average RMS error for all of them is 0.2 K.

Once the gain matrix is known, the radiometer channel phase imbalance can be obtained from G_{33} and G_{34} by

$$\Delta\phi = \begin{cases} \sin^{-1}\left(\dfrac{G_{34}}{\sqrt{G_{33}^2 + G_{34}^2}}\right) & if \quad G_{33} \geq 0 \\ 180^0 - \sin^{-1}\left(\dfrac{G_{34}}{\sqrt{G_{33}^2 + G_{34}^2}}\right) & if \quad G_{33} < 0 \end{cases} \tag{3.6.1}$$

The radiometer channel phase imbalance using (3.6.1) is 21.39°, with a positive imbalance indicating that the *v*-pol channel has a longer electrical length. This result was corroborated by injecting an in-phase sinusoidal test signal into both input channels of the radiometer and measuring the phase difference between them at the output ports of the demodulator to be 18.14°. The small discrepancy between the two values is likely due to the phase imbalance of the 3 dB splitter used to generate the test signal and to phase

imbalances in the digital back end of the radiometer, which were not included in the test using the sinusoidal signal.

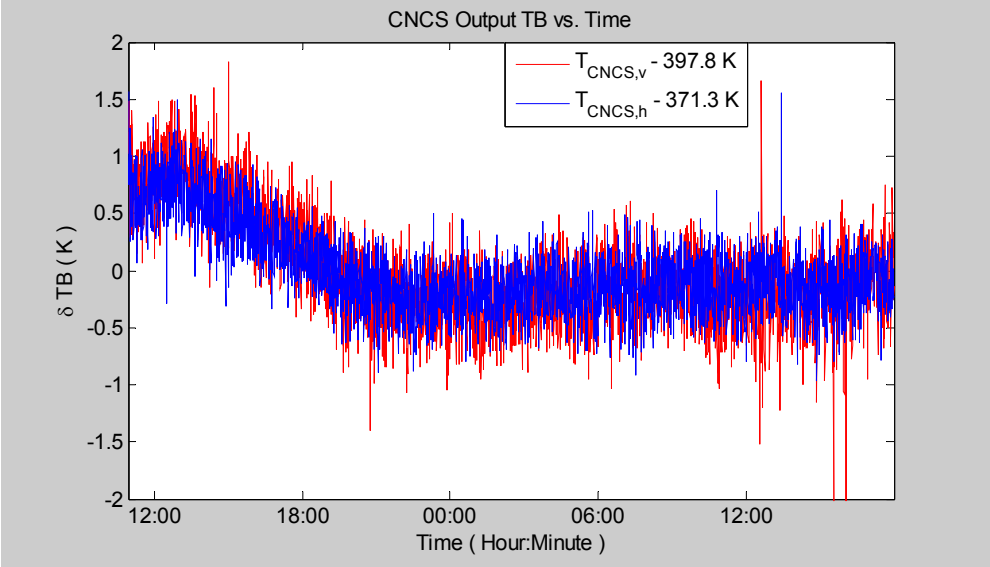

(a)

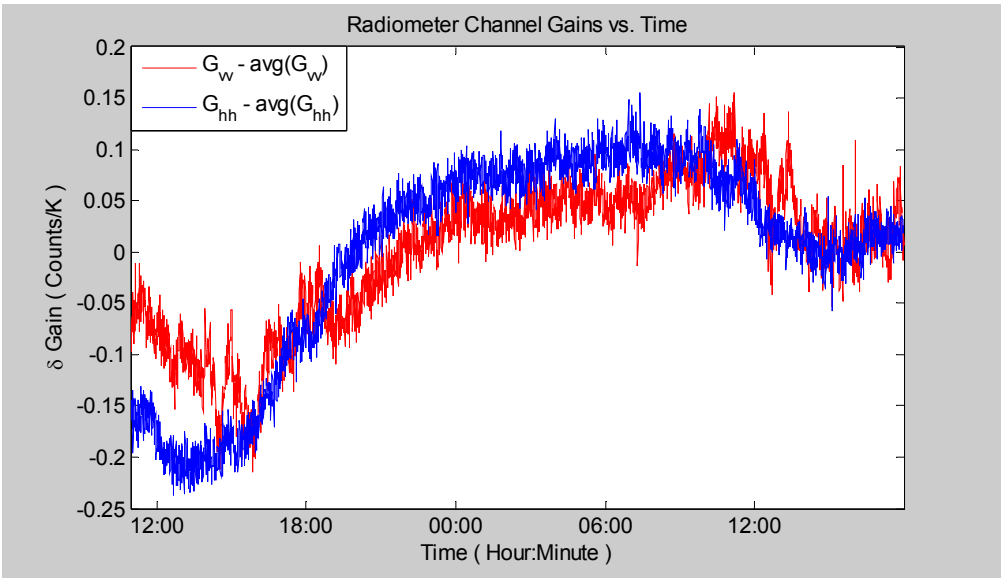

(b)

Figure 3.12 CNCS and radiometer drift. (a) CNCS channel gain drift; (b) channel gain drift of the DetMit L-band Radiometer

3.6.8 CNCS and Radiometer Under Test Gain Drift

A ~30 hour time series of measurements with the CNCS and the DetMit radiometer has been taken to investigate the drift of the CNCS and the radiometer. The CNCS channel gain drifts are shown in Figure 3.12a. The averages of the CNCS output are 397.8 Kelvin for *v*-pol channel and 371.3 Kelvin for *h*-pol channel. Brightness temperature variations for both channels are less than 2 Kelvin, and the long terms stability is better than 0.5%. This result shows the excellent stability of the CNCS.

Figure 3.12b shows the channel gain drift of the DetMit radiometer versus time. In the afternoon, because the room temperature is relatively high, the radiometer gain is low. At midnight, the gain is much more stable due to a stable ambient room temperature.

3.7 Validation of the Retrieved Calibration Parameters

The calibration algorithm estimates both CNCS and RUT forward model parameters simultaneously. Because both forward models account for non-ideal characteristics, several tests were performed to ensure that non-idealities in the CNCS did not influence the parameters retrieved for the RUT, and vice versa. The tests involved introducing certain changes into either the CNCS or RUT hardware and then verifying that the changes in retrieved parameters responded accordingly.

3.7.1 CNCS Channel Gain Imbalance Validation

A coaxial attenuator was inserted between the AWG and the RF head of the CNCS, first along the *v*-pol and then along the *h*-pol signal paths. The attenuation was measured to be 1.91 dB by a network analyzer. The retrieved CNCS channel gain

imbalance parameters (k_v and k_h in (3.2.2)) were altered as a result. Using the new values for k_v and k_h, the maximum possible brightness temperature that the CNCS could generate decreased by 1.84 dB and 1.89 dB for the *v*- and *h*-pol channels, respectively. The differences from the 1.91 dB change predicted by the network analyzer measurement likely result from a combination of CNCS parameter estimation errors, network analyzer measurement errors, and the differences in impedance matching for each of the three cases.

3.7.2 CNCS and Radiometer Channel Phase Imbalance Validation

An SMA male/female adapter was inserted at various places along the CNCS coaxial signal path or between the CNCS and the RUT. The adapter introduces an additional phase imbalance into the system. The locations where the adapter was added are shown in Figure 3.13. For each position of the adapter, the complete calibration procedure was followed in order to retrieve all forward model parameters – in particular both the CNCS and the radiometer channel phase imbalances. One or the other of the phase imbalances (but not both) should change, depending on where the adapter was placed. The retrieved change should be close to the electrical length of the SMA adapter itself, as determined independently by a network analyzer. Small differences are possible due impedance mismatches between the adapter and the circuit at its point of insertion. Results of these tests are summarized in Table 3.8. In the table, the letter given in column 1 (SMA location) matches the spot labeled in Figure 3.13 where the SMA adapter was inserted. Column 2 ($\Delta\theta_{CNCS}$) gives the change in the CNCS phase imbalance, Δ, due to the insertion of the adapter. Column 3 ($\Delta\theta_{RAD}$) gives the change in the radiometer phase imbalance, as defined by (8), due to the insertion of the adapter.

Column 4 (Predicted phase shift) gives the change predicted based on network analyzer measurements, which varies with each adapter location because the frequency of the signal changes. Column 5 (Retrieval error) gives the difference between the predicted and retrieved change in phase imbalance for the retrieved imbalance that was supposed to change. The change in the other imbalance should in all cases have been zero.

The sign of the changes in phase imbalance listed in Table 3.8 follows sign conventions for the imbalance in the *v*-pol channel relative to the *h*-pol channel. In each case, the phase shift due to the adapter has the predicted sign. The RMS error in magnitude of the retrieved phase shift over all 6 cases, relative to the value predicted by network analyzer measurements of the adapter, is 0.8^{o}. Any change in the retrieved phase imbalance for the portion of the system that was not affected by the insertion of the adapter represents an error. These are the shaded entries in Table 3.8. The RMS value of these errors, over all 6 cases, is 0.3^{o}.

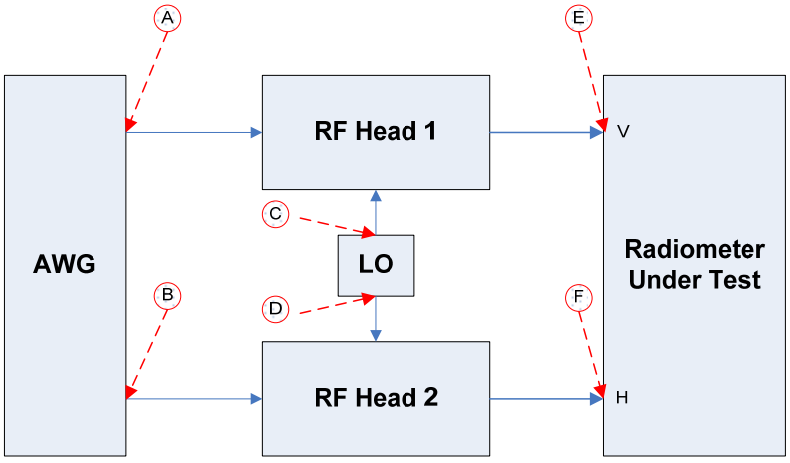

Figure 3.13 Locations where an additional adapter was inserted to verify the proper retrieval of phase imbalances between *v*- and *h*-pol channels. The circled numbers indicate the placement of the adapter.

Table 3.8. Verification of Channel Phase Imbalance Retrieval

SMA adapter Location	$\Delta\theta_{CNCS}$* (deg)	$\Delta\theta_{RAD}$** (deg)	Predicted Phase Shift (deg)	Retrieval Error (deg)
A	-7.005	0.141	-7.200	0.195
B	8.018	0.258	7.200	0.818
C	-23.554	-0.008	-24.330	0.776
D	24.677	0.204	24.330	0.347
E	0.205	-32.581	-31.550	-1.031
F	0.620	32.833	31.550	1.283

*$\Delta\theta_{CNCS}$ is the CNCS phase imbalance shift due to the SMA adapter
**$\Delta\theta_{RAD}$ is the radiometer phase imbalance shift due to the SMA adapter

3.8 Summary

Test procedures and data analysis algorithms have been presented to calibrate a fully polarimetric radiometer receiver using the Correlated Noise Calibration Standard (CNCS). The CNCS is a digital microwave signal generator capable of producing pairs of simulated thermal noise signals which have independent programmable brightness temperatures and partial correlation. In order to accurately calibrate the radiometer, it is necessary to identify and quantify the non-ideal characteristics of the CNCS. In other words, the calibration source must also be calibrated. It is possible to calibrate both radiometer and CNCS simultaneously, provided a sufficient number and variety of test signals and conditions are generated.

Simultaneous calibration is approached by developing parameterized forward models for both the CNCS and radiometer. The CNCS forward model describes the relationship between the digitally programmable settings of the signal generator and the actual brightness temperatures that are generated. The radiometer forward model, in turn,

describes the relationship between the brightness temperatures entering its input ports and the detector counts recorded on its data system. Composed together, the complete forward model relates programmable CNCS settings to radiometer counts. The simultaneous calibration algorithm estimates the parameters of the complete forward model from the counts that are measured while the CNCS settings are varied over a suitable range.

All of the unknown parameter in the CNCS and RUT forward models except the CNCS channel phase imbalance can be resolved simultaneously. The CNCS channel phase imbalance which has been shown not to be resolvable simultaneously can be obtained by cross-swapping the CNCS output cables. Simulations using the CNCS parameters and the AESMIR gain matrix show that the calibration test set is efficient, and the calibration algorithm can calibrate a fully polarimetric radiometer with high accuracy.

The calibration method has been demonstrated using L-band versions of the CNCS and a correlating polarimetric radiometer. All elements of the polarimetric gain matrix of the radiometer are solved for, including the off-diagonal elements that account for gain and phase imbalances between polarimetric channels. All necessary gain and phase imbalance parameters of the CNCS are also retrieved. The validity of the solutions is tested by intentionally modifying the amplitude and phase imbalances of both the CNCS and the radiometer in known ways, and then verifying that the calibration procedure correctly identifies the changes. In all cases, the tests were successful. In particular, the calibration procedure was correctly able to identify whether a change was made to the CNCS or the radiometer and whether the change altered the amplitude or the phase imbalance between *v*- and *h*-pol channels.

The CNCS has both advantages and limitations relative to other methods for calibrating a polarimetric radiometer. The most important limitation is the fact that, because it is installed in place of a radiometer's antenna, the CNCS cannot calibrate the effects of the antenna itself on measurement of the Stokes parameters in brightness temperature. Cross-pol leakage in the antenna, for example, would not be accounted for by the off-diagonal terms of the polarimetric gain matrix estimated by the CNCS. Those terms would only characterize the behavior of the receiver, orthomode transducer, and other components and subsystems present during CNCS testing. Antenna effects would still need to be accounted for by some other means – typically with antenna range measurements and/or on-orbit intercomparisons with ground truth-based radiative transfer model predictions. Other, relatively minor, limitations with a CNCS calibration include the available bandwidth of its simulated noise (currently limited to 500 MHz by the clock rate of the commercial AWG being used) and the fact that the effective brightness temperature generated by the CNCS needs to be re-calibrated whenever changes are made to the radiometer passband response (because the CNCS active cold load has a frequency dependent brightness temperature).

The primary advantages of CNCS calibration are its simplicity and automation and its flexibility. The ready availability of a variable brightness temperature source during receiver development, integration and testing, without the need for LN_2 cooling, can be extremely convenient and time saving. The ability to generate known 3^{rd} and 4^{th} Stokes parameters in brightness temperature, to vary them in a known way, and to be able to precisely and accurately reproduce them later, can greatly simplify the characterization and trouble shooting of a polarimetric receiver during its development phase. And the

fact that variations in both signal strength and polarization coherence are programmable makes fully automated testing straightforward. The precision, or repeatability, of estimates of the polarimetric gain matrix and offset vector were shown to be approximately 0.2 K for the gain elements and 0.05 K for the offsets. The accuracy of the retrieved CNCS calibration parameters can be estimated by comparisons with network analyzer measurements of the radiometer components. The phase imbalance between *v*- and *h*-pol channels, introduced by adding an SMA adapter (see Table 3.8), was estimated with 0.8^{o} RMS accuracy with respect to the network analyzer measurements. Changes in amplitude of the CNCS channels are more difficult to validate due to the inherent inaccuracies associated with network analyzer measurements of absolute component losses. CNCS amplitudes have been validated with an accuracy of at best several Kelvins.

Absolute end-to-end calibration of any radiometer is best done with the complete system, including its antenna, assembled while viewing external calibration targets. The greatest value of the CNCS is as a tool during radiometer development. It can generate precise and repeatable variations in the full Stokes parameters in brightness temperature. This permits a determination of the relative response of the radiometer to known changes in its input.

3.9 Original Contributions and Publication

Original contributions concerning the polarimetric radiometer calibration method include

1) Development of a CNCS hardware forward model;
2) Development of implementation of a calibration algorithm, including experimental validation;
3) Development of an impedance-mismatching correction algorithm for the retrieved radiometer gain matrix and offsets and CNCS forward model parameters.

One associated paper is published:

1) J. Peng and C. Ruf, "*Calibration Method for Fully Polarimetric Radiometers using the Correlated Noise Calibration Standard*," IEEE Trans. Geosci. Remote Sens., 46(10), Oct. 2008.

Chapter 4

CNCS Application I — Aquarius

The L-Band CNCS was used to evaluate and the Aquarius engineering model radiometer at NASA Goddard Space Flight Center (GSFC). Evaluation tests included retrieval of the gain matrix and radiometer channel phase imbalance and the investigation of the temperature characteristics of the *v*-pol antenna cable. The calibration method is described in Chapter 3, except that the effects of impedance-mismatches are not considered. The effect of calibration error due to radiometer channel phase imbalance has been analyzed. Results show that the CNCS can generate calibration signals over a large dynamic range and can calibrate a fully polarimetric radiometer with high precision.

4.1 Introduction to the Aquarius Radiometer

The Aquarius radiometer is a tri-polarimetric radiometer: it has the third Stokes channel formed by using the p- and m-pol channels and it does not include a fourth Stokes channel. A detailed block diagram and the illustration are shown in Figure 4.1 and Figure 4.2 respectively [54].

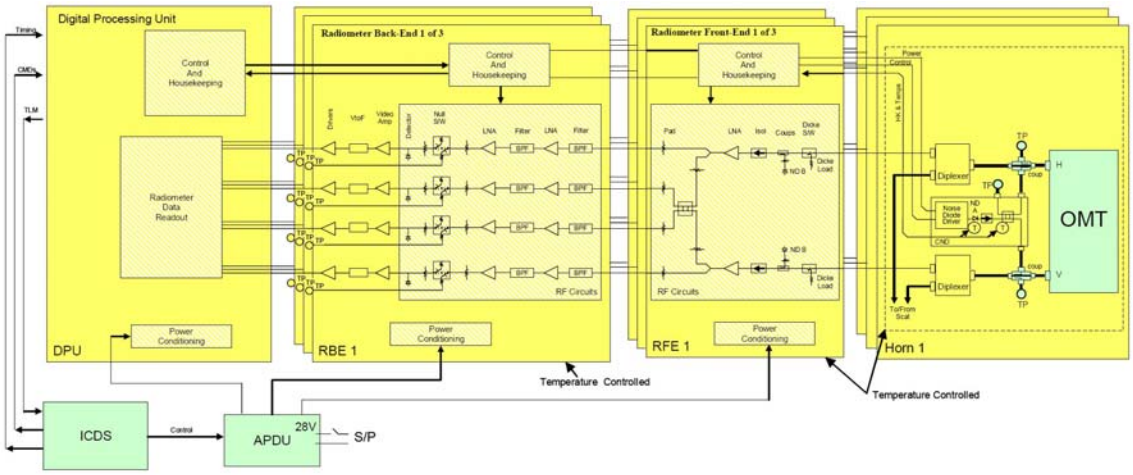

Figure 4.1 Detailed aquarius radiometer block diagram [54]

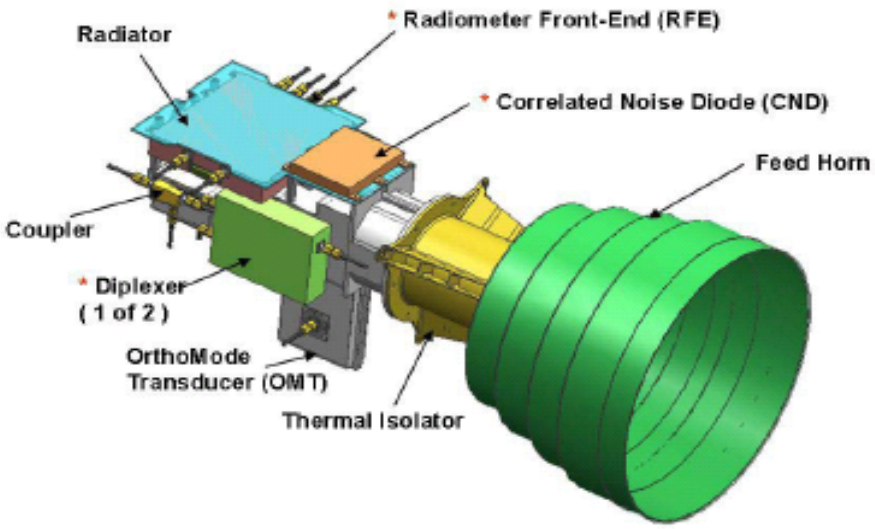

Figure 4.2 Illustration of the Aquarius radiometer installation [54]

The p- and m-pol channels are used to estimate the degree of Faraday rotation with the assumption that the third and fourth Stokes brightness temperatures emitted from the sea surface at L-band are zero. Since the channel phase imbalance of the radiometer itself can affect the measurement of the correlation between the *v*- and *h*-pol signals, it

needs to be characterized precisely. The CNCS has the ability to investigate the channel phase imbalance of the radiometer since it can measure the radiometer gain matrix, and then obtain its channel phase imbalance.

For each radiometer, the two-channel cables connecting the feed horn with the Radiometer Front-End (RFE) are temperature controlled, but the control cannot guarantee perfectly matched temperature variations. Unmatched variations can introduce phase mismatches, whuch must be predictable in order to be corrected in ground processing. The CNCS is used to determine the temperature dependent characteristics of the cable.

4.2 Aquarius Radiometer (EM) Calibration

The L-band CNCS is primarily designed for the Aquarius radiometer calibration. It has almost the same CNCS configuration as that for the DetMit radiometer calibration except that the output cables are 1 foot shorter due to availability, and the differences of brightness temperatures provided by the CNCS are 2.35 Kelvin for *v*-ch and 0.1 Kelvin for *h*-ch. Difference of the *v*-ch might be due to impedance mismatching, calibration error of the CNCS ColdFET, or the non-ideal characteristics of the CNCS itself. The difference of two measurements on the CNCS channel phase imbalance is 0.88°, which might be due to different output cables.

Table 4.1 Gain matrix (in Counts/K) and offsets (in Counts) at 22.3°C

	T_v	T_h	T_3	T_4	*offset*
C_v	0.9374	0.0002	0.0010	-0.0015	455.9503
C_h	0.0003	0.9189	-0.0027	-0.0033	469.3608
C_p	0.4683	0.4839	0.4686	0.0684	450.4431
C_m	0.4046	0.3986	-0.3951	-0.0702	759.7019

The retrieved Aquarius radiometer gain matrix and channel offsets are listed in Table 4.1. The measurements were made at room temperature and are the average of 4 independent retrievals. It takes 15 minutes to generate the measurements required for each retrieval. From the gain matrix, the coupling coefficient from *v*-pol to *h*-pol can be determined to be -34.9 dB and the coupling from *h*-pol to *v*-pol is -36.6 dB. The offset of the m-pol channel is significantly higher than that of the others. The phase imbalance between the *v*-pol and *h*-pol channels of the radiometer is found to be 8.31°. Cross-talk in the video circuits dominates the inter-channel gain elements and this lesson-learned resulted in design improvements.

4.3 Temperature Characteristics of the Aquarius Antenna Cable

CNCS has the ability to dynamically retrieve the gain matrix. On 8-9 Feb 2007, a test was conducted in which the physical temperature of the teflon-core coaxial cable connecting the Aquarius *v*-pol channel receiver to the antenna assembly was rapidly increased from 15°C to 44°C, held at 44°C for approximately 20 hours, and then dropped back to room temperature as shown in Figure 4.3. The objective was to investigate the temperature sensitivity of the cable.

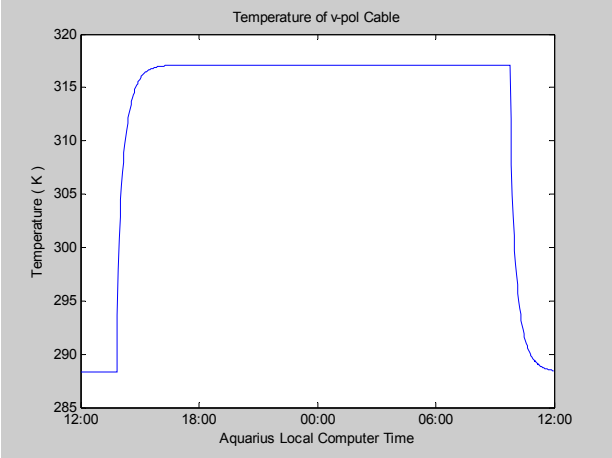

Figure 4.3 The physical temperature of the teflon-core coaxial cable

A time series of the retrieved CNCS outputs, gain matrix elements and the derived phase imbalance between *v*- and *h*-pol channels are shown in Figure 4.4. The phase imbalance can be seen to decrease with increasing cable temperature during the first ~1 hour of the test. The total change in phase imbalance is 0.35° over a temperature change of 29°C. Several hours after the temperature had reached 44°C, there was a sudden decrease in the gain of the *M*-pol radiometer channel, as seen in the time series of raw measurement of *M*-pol channel in Figure 4.5, while measurements in other channels kept stable. This hardware shift generated a spurious jump in the retrieved parameters including phase imbalance, shown in Figure 4.4, that is probably not real. Once the gain stabilized at its new lower value, the retrieval of parameters—the gain matrix elements and offsets, the CNCS outputs, and radiometer phase imbalance—recovered back to its previous value. Near the end of the experiment, the temperature was lowered back to ambient and the phase imbalance shifted back toward its original value (but not quite all the way since the temperature was not cooled all the way back down to 15°C). The precision of the retrieved channel phase imbalance is 0.02°.

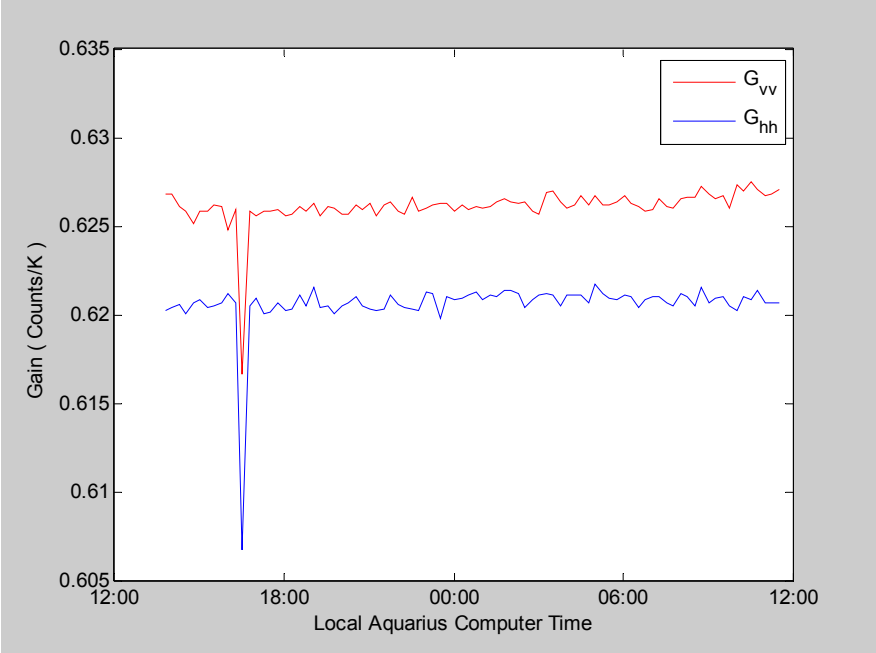

(a) G_{vv} and G_{hh}

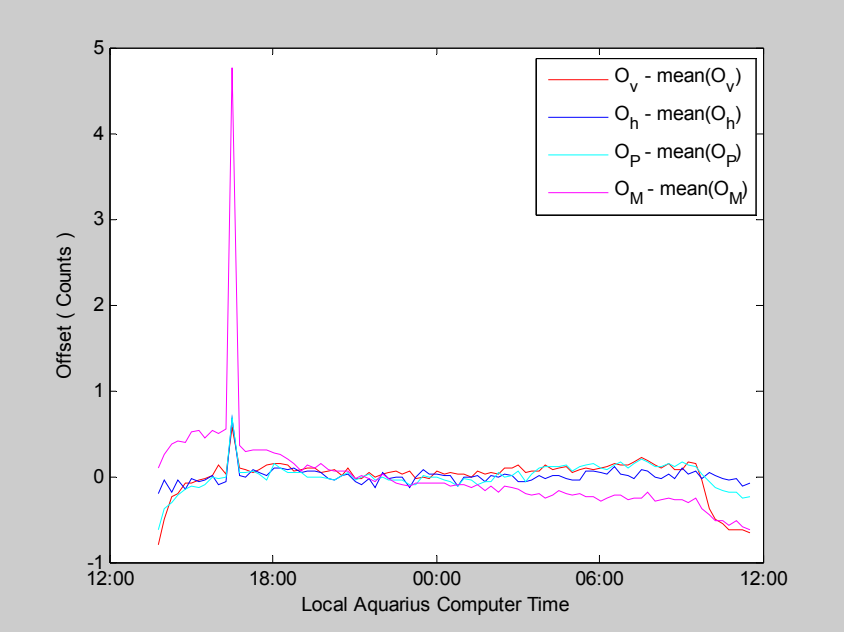

(b) Offsets

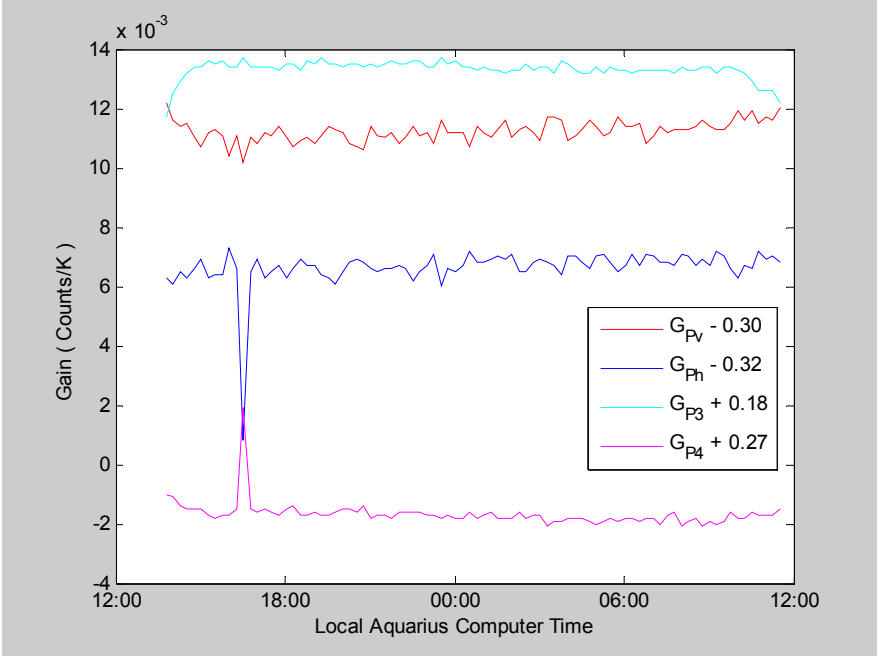

(c) G_{Pv}, G_{Ph}, G_{P3} and G_{P4}

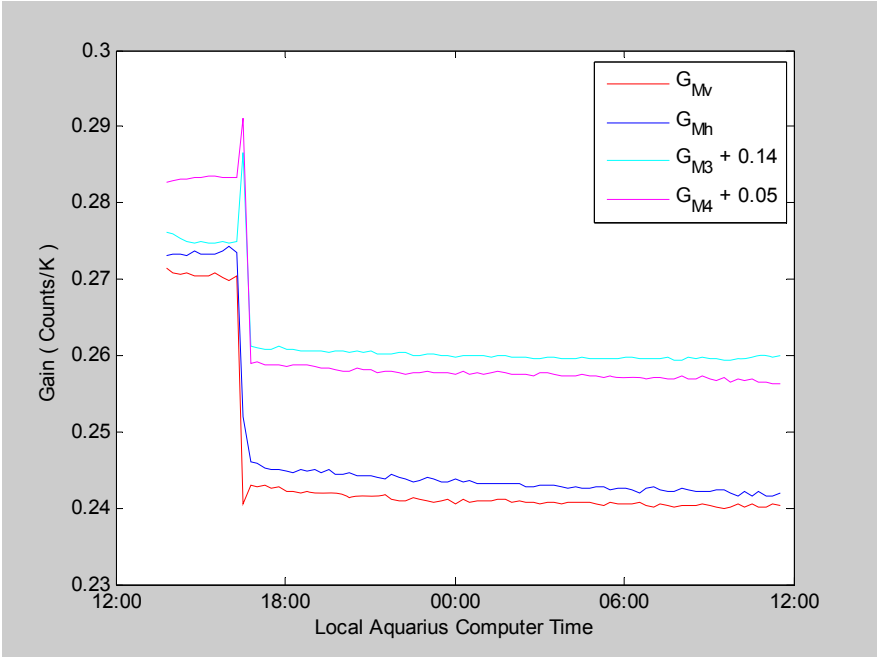

(d) G_{Mv}, G_{Mh}, G_{M3} and G_{M4}

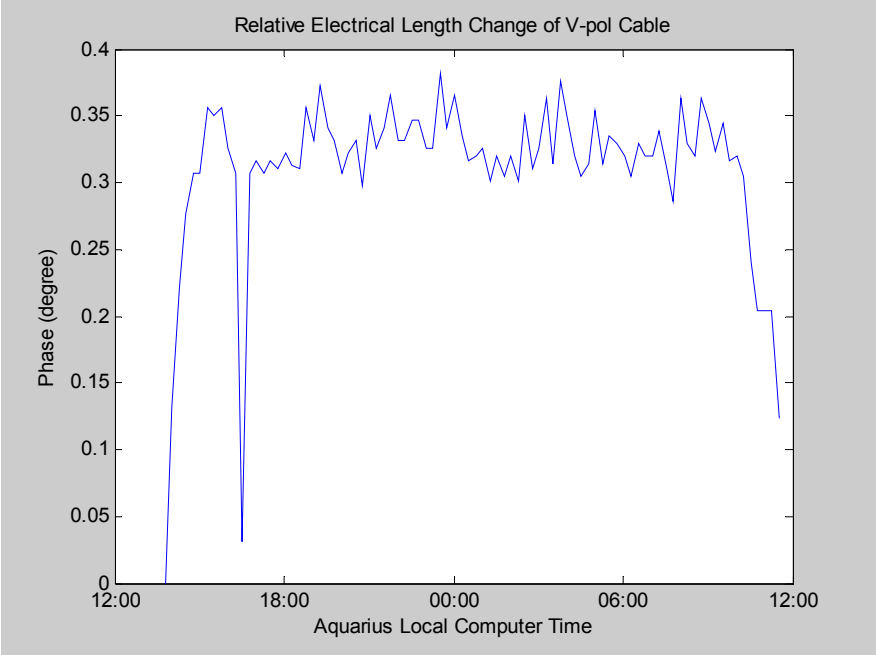

(e) Relative electrical length change of the *v*-pol cable

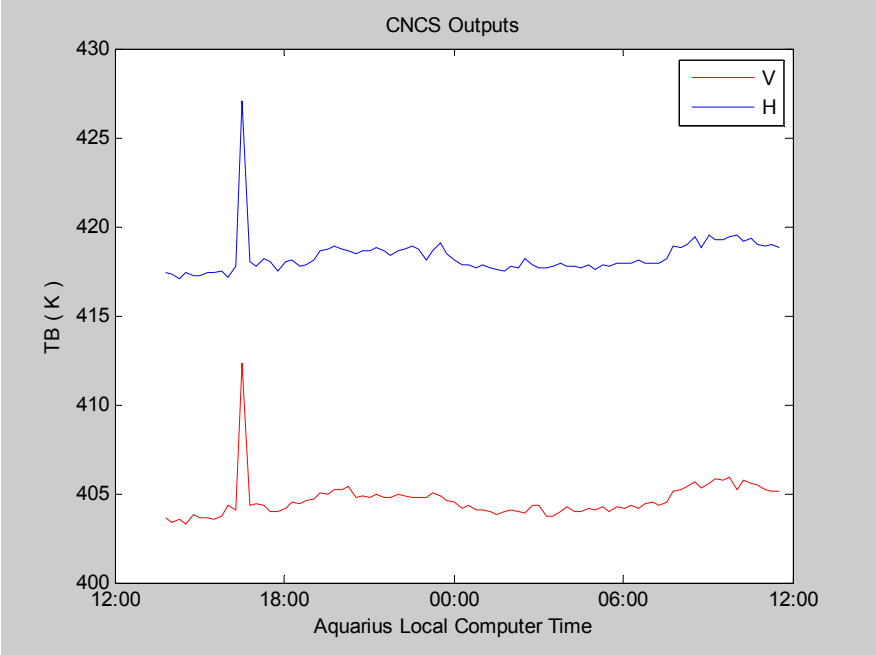

(f) Change of the CNCS outputs

Figure 4.4 Change in Aquarius radiometer gain matrix elements (a~d), *v*-pol/*h*-pol phase imbalance (e) and CNCS output (f) during ~24 hour test while varying *v*-pol input cable temperature.

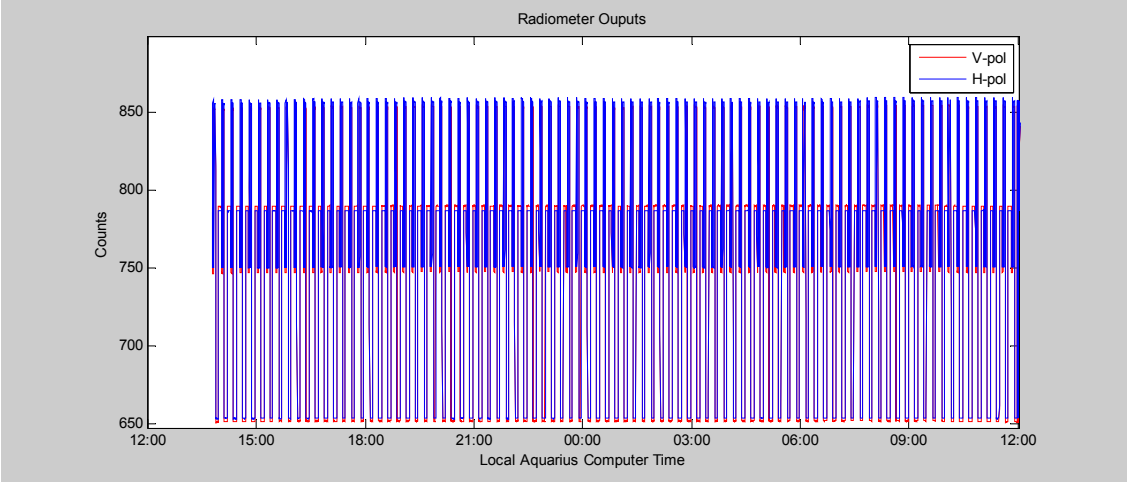

(a) Raw measurements for *v*- & *h*-pol. channels

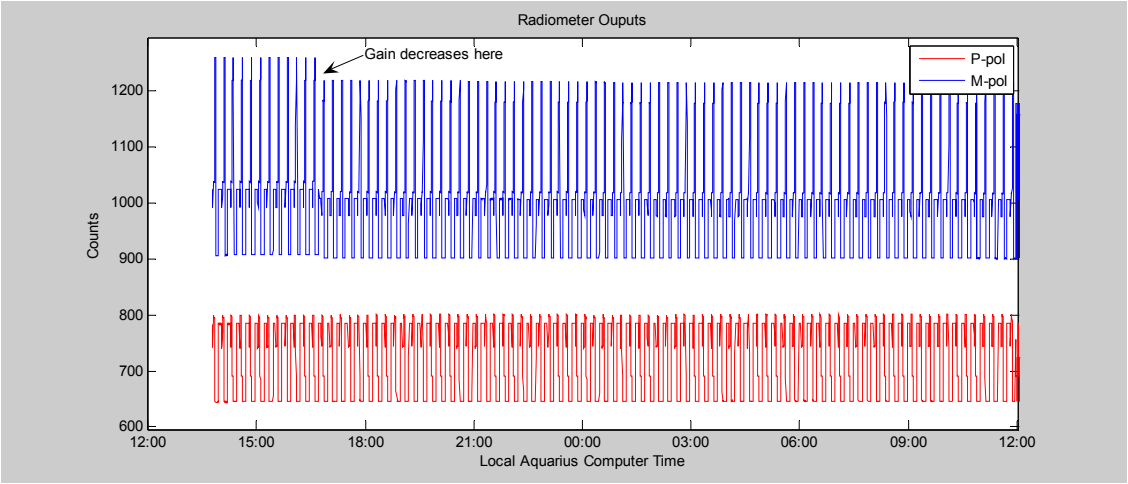

(b) Raw measurements for *P*- & *M*-pol. channels

Figure 4.5 Aquarius radiometer raw measurements

4.4 Effect of Calibration Error to the Retrieved Sea Surface Salinity

As mentioned in section 4.2, the third Stokes channel is used to estimate the degree of Faraday rotation with the assumption that the third and fourth Stokes from the sea surface at L-band are zero. If there is error in the estimated radiometer channel phase

imbalance, the estimated degree of Faraday ration will be biased and the retrieved SSS will be wrong.

A radiometer can be treated as a combination of a perfectly phase-balanced radiometer with gain maxtrix G' and a phase shift network. The phase shift network can be represented by the matrix M, or

$$M = \begin{bmatrix} 1 & 0 & 0 & 0 \\ 0 & 1 & 0 & 0 \\ 0 & 0 & \cos(\Delta\phi) & \sin(\Delta\phi) \\ 0 & 0 & -\sin(\Delta\phi) & \cos(\Delta\phi) \end{bmatrix} \tag{4.4.1}$$

where $\Delta\phi$ is the radiometer channel phase imbalance.

The matrix of the phase shift network can be divided into 2 matrices. One contains the estimated radiometer channel phase imbalance only and the other contains the error of the estimated radiometer channel phase imbalance.

$$M_{est} = \begin{bmatrix} 1 & 0 & 0 & 0 \\ 0 & 1 & 0 & 0 \\ 0 & 0 & \cos(\Delta\phi_{est}) & \sin(\Delta\phi_{est}) \\ 0 & 0 & -\sin(\Delta\phi_{est}) & \cos(\Delta\phi_{est}) \end{bmatrix} \tag{4.4.2a}$$

and

$$M_{err} = \begin{bmatrix} 1 & 0 & 0 & 0 \\ 0 & 1 & 0 & 0 \\ 0 & 0 & \cos(\Delta\phi_{err}) & \sin(\Delta\phi_{err}) \\ 0 & 0 & -\sin(\Delta\phi_{err}) & \cos(\Delta\phi_{err}) \end{bmatrix} \tag{4.4.2b}$$

where $\Delta\phi_{est}$ is the estimated radiometer channel phase imbalance and $\Delta\phi_{err}$ is its estimated error, and $\Delta\phi = \Delta\phi_{est} + \Delta\phi_{err}$.

So the true radiometer gain matrix is given by

$$G = G' \cdot M = G' \cdot M_{est} \cdot M_{err} \tag{4.4.3}$$

The estimated input Stokes brightness temperatures $\{T'_{x,est}$, x = v, h, 3 & 4$\}$ and the true input Stokes brightness temperatures $\{T'_x$, x = v, h, 3 & 4$\}$ are related by

$$\begin{pmatrix} T'_{v,est} \\ T'_{h,est} \\ T'_{3,est} \\ T'_{4,est} \end{pmatrix} = M_{err} \begin{pmatrix} T'_v \\ T'_h \\ T'_3 \\ T'_4 \end{pmatrix} \tag{4.4.4}$$

or

$$T'_{v,est} = T'_v \tag{4.4.5a}$$

$$T'_{h,est} = T'_h \tag{4.4.5b}$$

$$T'_{3,est} = T'_3 \cos(\Delta\phi_{err}) + T'_4 \sin(\Delta\phi_{err}) \tag{4.4.5c}$$

$$T'_{4,est} = -T'_3 \sin(\Delta\phi_{err}) + T'_4 \cos(\Delta\phi_{err}) \tag{4.4.5d}$$

The fourth Stokes brightness temperature is insensitive to the Faraday rotation. With the assumption that the fourth Stokes brightness temperature from the sea surface at L-band is zero, T'_4 in Equations (4.4.5c) and (4.4.5d) is zero.

Ignoring the contribution of the third Stokes parameter from the sea surface, the degree of Faraday rotation is estimated by [19]

$$\begin{aligned} \Omega_{est} &= \frac{1}{2}\tan^{-1}\left(-\frac{T'_{3,est}}{T'_{v,est} - T'_{h,est}}\right) \\ &= \frac{1}{2}\tan^{-1}\left\{-\frac{T'_3}{T'_v - T'_h}\cos(\Delta\phi_{err})\right\} \end{aligned} \tag{4.4.6}$$

and the *v*- & *h*-pol brightness temperatures from the sea surface are estimated by [19]

$$
\begin{aligned}
T_{v,est} &= T'_{v,est}\cos^2\Omega_{est} + T'_{h,est}\sin^2\Omega_{est} - \frac{T'_{3,est}}{2}\sin 2\Omega_{est} \\
&= T'_{v}\cos^2\Omega_{est} + T'_{h}\sin^2\Omega_{est} - \frac{T'_{3}}{2}\cos(\Delta\phi_{err})\sin 2\Omega_{est}
\end{aligned}
\tag{4.4.7a}
$$

$$
\begin{aligned}
T_{h,est} &= T'_{v,est}\sin^2\Omega_{est} + T'_{h,est}\cos^2\Omega_{est} + \frac{T'_{3,est}}{2}\sin 2\Omega_{est} \\
&= T'_{v}\sin^2\Omega_{est} + T'_{h}\cos^2\Omega_{est} + \frac{T'_{3}}{2}\cos(\Delta\phi_{err})\sin 2\Omega_{est}
\end{aligned}
\tag{4.4.7b}
$$

where the value of $\{T'_x$, x = *v*, *h* & 3$\}$ is from Equations (1.3.2) & (1.3.3) with $T_3 = 0$.

The estimated *v*- & *h*-pol brightness temperatures from the sea surface are function of the calibration error of the radiometer channel phase imbalance. When the calibration error is zero, the estimated brightness temperatures are unbiased. If the calibration error is non-zero, the estimated errors would be given by

$$\delta T_v = T_{v,est}(\Delta\phi_{err}) - T_{v,est}(\Delta\phi_{err} = 0) \tag{4.4.8a}$$

$$\delta T_h = T_{h,est}(\Delta\phi_{err}) - T_{h,est}(\Delta\phi_{err} = 0) \tag{4.4.8b}$$

Assuming that SSS = 32.54 ppt, SST = 15 °C, and the *v*- & *h*-pol brightness temperatures are 114 Kelvin and 77 Kelvin respectively, the estimated errors versus the calibration errors of the radiometer channel phase imbalance are shown in Figure 4.6.

The error can't be ignored. For example, with 10° Faraday rotation angle and 7° calibration error of the radiometer channel phase imbalance, the errors on *v*- & *h*-pol brightness temperatures will be -0.016 K and 0.016 K. Considering that the requirement of the long-term calibration stability is 0.15 K over 7 days [54], the 7° radiometer channel phase imbalance error will contribute 11% of the error budget.

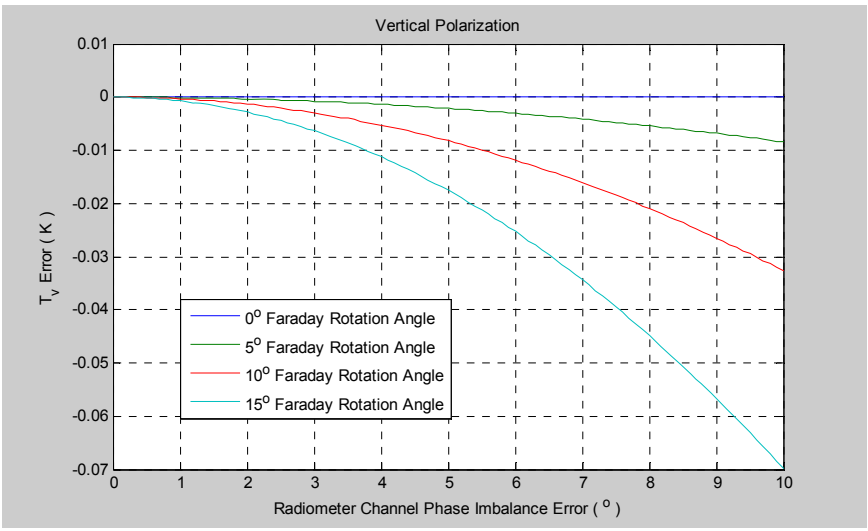

(a) Vertical polarization

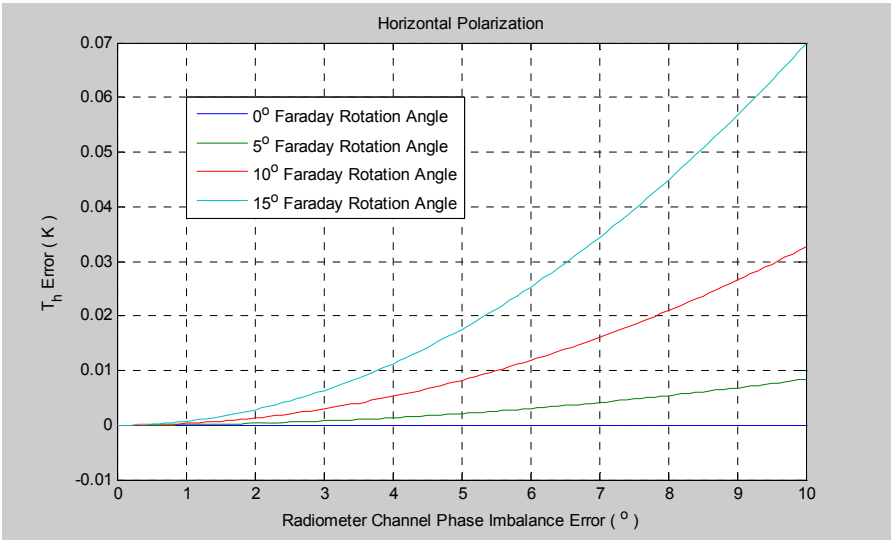

(b) Horizontal polarization

Figure 4.6 Effect of the calibration error of the radiometer channel phase imbalance

4.5 Summary

The new and improved L-Band CNCS was used to evaluate the Aquarius engineering model radiometer at GSFC. The CNCS channel phase imbalance can be

retrieved by cross-swapping CNCS output cables. All other unknown parameters of both the CNCS and the radiometer under test can be retrieved simultaneously.

Tests included retrieval of gain matrix and radiometer channel phase imbalance and the investigation of the temperature characteristics of the *v*-pol antenna cable. The effect of the calibration error of the radiometer channel phase imbalance has been analyzed. Results show that the CNCS can generate calibration signals over a large dynamic range and can calibrate a fully polarimetric radiometer with high precision.

4.6 Original Contributions and Publication

The original contributions related to the application of CNCS calibration to the Aquarius radiometer include:

1) Gain matrix and channel phase imbalance for the Aquarius radiometer are obtained;
2) Characterization of the temperature dependence of the Aquarius antenna cable with respect to phase imbalance;
3) Analysis of the effect on system calibration of the radiometer channel phase imbalance.

One associated paper is published:

1) J. Peng, C.S. Ruf, S. Brown and J. Piepmeier, "*Characterization of the Aquarius and Juno Radiometers Using a Programmable Digital Noise Source*," Proc. 2007 IEEE International Geoscience and Remote Sensing Symposium, Barcelona, SPAIN, 23-27 July, 2007.

Chapter 5

CNCS Application II — Juno

Juno is a mission to explore Jupiter by peering deep into Jupiter's atmosphere to uncover evidence of fundamental processes associated with the formation and early evolution of our solar system. The primary instrument is the Juno Microwave Radiometer (MWR) and its primary goal is to profile the relative abundance of water and ammonia gas in the deep atmosphere of Jupiter.

The Juno MWR built by the JPL consists of 6 frequency bands centered at 0.6, 1.25, 2.6, 5.2, 10 and 22 GHz. The spacecraft is illustrated in Figure 5.1 [75].

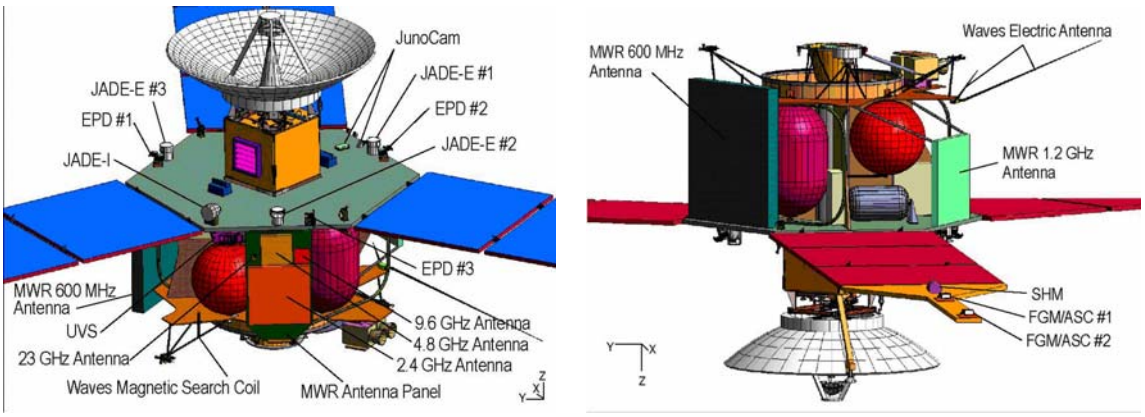

(a) Front view (b) Back view

Figure 5.1 Illustration of the Juno spacecraft [75]

The MWR will obtain measurements by scanning Jupiter along the orbital track as the spacecraft spins around its z-axis in Figure 5.1. Due to the synchrotron emission, which is electromagnetic radiation generated by extremely high speed electrons accelerating through its magnetic field, the received brightness temperature could be high up to 20,000 Kelvin at the longest wavelengths. To correct for the synchrotron emission entering the radiometer, its dynamic range needs to be much higher than that of a conventional radiometer used for Earth remote sensing with an upper limit of approximately 300 Kelvin.

The L-band CNCS was used to calibrate the breadboard model of the 1.2 GHz channel of the Juno MWR receiver. Its bandwidth is 25 MHz . Calibration tests include linearity tests and a Juno orbit TB profile simulation. The goal of these tests, for our purposes, is to demonstrate that the CNCS has the ability to calibrate the Juno radiometer. The goal for the Juno project is to verify the required performance of the MWR receiver and to fully characterize its performance as part of the development of a Level 1 flight calibration algorithm.

5.1 CNCS Linearization

The current version of the CNCS was originally designed for the 1.4 GHz Aquarius radiometer, and the highest brightness temperature that could be output is approximately 5000 Kelvin with a 60 MHz signal bandwidth. The lowest brightness temperature is 110 Kelvin (limited by the CNCS ColdFET, with a brightness temperature of 104 Kelvin at 1.2 GHz).

The voltage gain of the AWG output amplifiers can only be varied over a range of [0.17, 0.25], resulting in an AWG dynamic range of 3.3 dB. For this reason, 12 lookup tables with different signal variance are used to cover the brightness temperature range of [110, 5000]. Overlap exists in the signal strength produced by neighboring lookup tables when the AWG output gain is varied. Therefore, the net output signal strength is a function of both the lookup table selected and the setting of the AWG output gain, and the CNCS forward model becomes

$$T_{cncs,m} = k_m G^2 T_n + O_{awg,m} + T_{cold} \tag{5.1.1}$$

where k_m is scale factor used to represent gain imbalance between the two CNCS channels. G is the voltage gain of the AWG channel with range [0.17 0.25]. T_n = 4480 Kelvin is the nominal brightness temperature generated by the AWG, and $O_{awg,m}$ is a possible offset brightness temperature. T_{cold} is the brightness temperature of the ColdFET. The subscript m designates the index of the lookup tables.

The output brightness temperature $T_{cncs,m}$ of lookup table m could be calibrated using conventional two-point temperature calibration method assuming a linear radiometer with enough large dynamic range. But there are two problems. One is that the known calibration sources are the CNCS ColdFET (Cold load) and Reference Load (Hot load). The brightness temperature of the hot load is around 300 Kelvin and the difference of brightness temperatures between the two known sources is about 200 Kelvin. Using the two calibration sources to measure the brightness temperature of 5000 Kelvin (or 20,000 Kelvin) will lead to large calibration error. The other problem is that the linearity of the radiometer is unknown, so the assumption does not stand.

One solution to this problem involves attenuating the AWG brightness temperature so that the CNCS output brightness temperature is in the range of the

brightness temperatures of the hot and cold loads. The CNCS forward model will be given by

$$T'_{cncs,m} = A\left(k_m G^2 T_n + O_{awg,m}\right) + T_{cold} \tag{5.1.2}$$

where A is the value of the attenuator.

Then the brightness temperature $T'_{cncs,m}$ can be calibrated using the hot and cold loads. If the attenuator is well known, the brightness temperature $T_{cncs,m}$ can be derived.

The attenuator can be measured in two approaches. The first approach is using a network analyzer, while the other approach is to measure it in-circuit. In-circuit measurement could be more accurate because the effect of impedance-mismatch is included in the derived value of the attenuator.

5.1.1 Calibration of an Attenuator in-Circuit

An attenuator inserted between the AWG and the RF Head can be calibrated in-circuit to obtained higher precision compared to measuring it with a network analyzer. Prior to linearization of the radiometer under test, it is necessary to constrain the CNCS output brightness temperature to be in the range of the brightness temperatures of the hot and cold loads. This is because the radiometer is regarded as linear in this range. So the AWG lookup table should be selected to satisfy this requirement.

For the L-band CNCS, the lookup tables with index less than or equal to 6 will satisfy this requirement (Lookup table 1 has the highest output brightness temperature). For each lookup table, at least four equations can be obtained with different AWG gain and with/without the attenuator present.

$$C_{1,m} = G_{rad} \cdot \left(k_m G_1^{\,2} T_n + O_{awg,m}\right) + O_{rest} \tag{5.1.3a}$$

$$C'_{1,m} = A \cdot G_{rad} \cdot \left(k_m G_1^{\,2} T_n + O_{awg,m}\right) + O_{rest} \tag{5.1.3b}$$

$$C_{2,m} = G_{rad} \cdot \left(k_m G_2^{\,2} T_n + O_{awg,m}\right) + O_{rest} \tag{5.1.3c}$$

$$C'_{2,m} = A \cdot G_{rad} \cdot \left(k_m G_2^{\,2} T_n + O_{awg,m}\right) + O_{rest} \tag{5.1.3d}$$

where G_{rad} is the gain of the radiometer under test, in Counts/Kelvin, and O_{rest} is the offset due to the CNCS ColdFET, radiometer noise figure, etc. in Counts.

The value of the attenuator can be obtained by

$$A = \frac{C'_{1,m} - C'_{2,m}}{C_{1,m} - C_{2,m}} \tag{5.1.4}$$

For example, the value of a 2 dB attenuator obtained in this way is plotted in Figure 5.2. The average value is -1.855 dB with an error of 0.07% which does not include the effects of mating/demating the connector. The value of the 2 dB attenuator measured by a network analyzer is -1.915 dB.

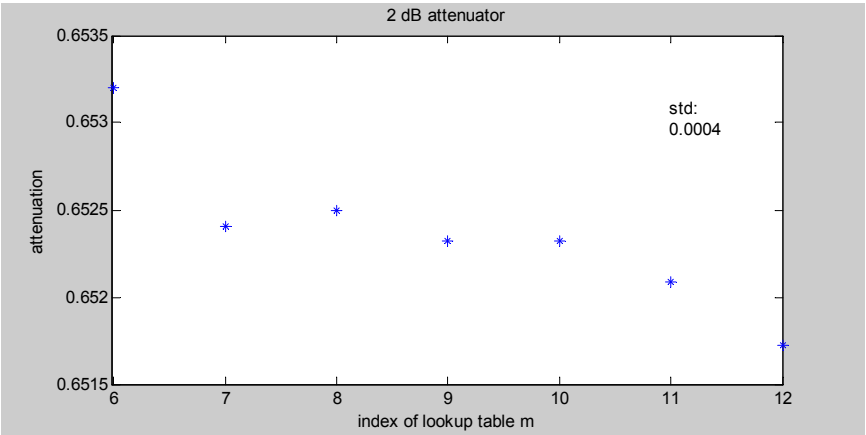

Figure 5.2 Measured value of the 2 dB attenuator

5.1.2 Retrieval of the CNCS Forward Model Parameters

There is another way to obtain the CNCS forward models without bringing down the CNCS outputs below the 300 Kelvin that is the brightness temperature of the CNCS

hot load. The advantage of this approach is that it does not require on the linearity of a radiometer above 300 Kelvin, and only one attenuator is needed. The attenuator is measured using the method in section 5.1.1.

The procedure is shown below:

1) Start from lookup table 1 (m = 1) with known brightness temperature 5000 Kelvin (maximum, let it be $T_{cncs,m,max}$).
2) Take a measurement with AWG gain G = 0.17. Let the radiometer output be C_m.
3) Insert a 2 dB attenuator between the AWG and the RF Head, then adjust the AWG gain so that the radiometer output is equal to C_m. If the exact matching is hard to obtain, interpolation can be used to find it. Record the corresponding AWG gain G_A. Then the following relation can be obtained.

$$0.25^2 k_m T_n + O_{awg,m} + T_{cold} = T_{cncs,m,\max} \tag{5.1.5a}$$

$$0.17^2 k_m T_n + O_{awg,m} = A \cdot \left(G_A^{\,2} k_m T_n + O_{awg,m} \right) \tag{5.1.5b}$$

With determined value of the 2 dB attenuator, A, the forward model parameters of lookup table m can be obtained

$$k_m = \frac{(A-1)\left(T_{cncs,m,\max} - T_{cold}\right)}{\left(0.25^2 A - G_A^{\,2} A - 0.0336\right) T_n} \tag{5.1.6a}$$

$$O_{awg,m} = \frac{\left(0.17^2 - A G_A^{\,2}\right) T_n}{A-1} k_m \tag{5.1.6b}$$

4) Find the maximum output brightness temperature, $T_{cncs,m+1,max}$, of lookup table m+1.

Because the nearby lookup tables are overlapped, the maximum outputs of the to-be-determined forward model of lookup table m+1 can be found. The approach is to adjust the AWG gain with lookup table m so that the radiometer output is equal to that with AWG gain 0.25 and lookup table m+1. Interpolation is used here as well. Assume that the adjusted AWG gain is G_f.

$$T_{cncs,m+1,\max} = G_f{}^2 k_m T_n + O_{awg,m} + T_{cold} \tag{5.1.7}$$

5) Repeat steps 2~4 until all the forward model parameters of all lookup tables are determined.

In these 2 approaches, the CNCS forward model parameters can be obtained and they are listed in Table 5.1.

Table 5.1 Retrieved CNCS forward model parameters

Index of Lookup Table	Parameter	Approach 1	Approach 2
1	k	17.387	17.481
	O_{awg}	92.131	87.211
2	k	8.706	8.737
	O_{awg}	46.995	46.239
3	k	4.379	4.376
	O_{awg}	22.180	24.182
4	k	2.197	2.190
	O_{awg}	11.035	13.378
5	k	1.096	1.096
	O_{awg}	6.817	7.851
6	k	0.553	0.545
	O_{awg}	2.720	5.944
7	k	0.277	0.273
	O_{awg}	1.420	4.427
8	k	0.139	0.136
	O_{awg}	0.571	3.860
9	k	0.093	0.093
	O_{awg}	0.504	3.422
10	k	0.051	0.050
	O_{awg}	0.272	3.225
11	k	0.028	0.028
	O_{awg}	0.104	2.788
12	k	0.015	0.017
	O_{awg}	0.113	2.441

Note: In approach 1, the attenuators are measured by a network analyzer; In approach 2, the attenuator is measured in-circuit.

5.2 Juno BM Radiometer Linearity Test

After the CNCS forward model is established, the CNCS can output signals with desired brightness temperatures. Injecting signals by sweeping brightness temperatures from the lowest to the highest will measure the linearity of the radiometer.

The AWG gain is changed from 0.17 to 0.25 in steps of 0.01 for each lookup table. The corresponding output brightness temperature $T_{cncs,m}$ from CNCS is injected into the Juno radiometer. The radiometer output counts are calibrated into brightness

temperature $T'_{cncs,m}$, referred to the radiometer input port, using the CNCS ColdFET and Reference Load as calibration sources, under the assumption that the radiometer is linear. If the assumption is true, $T_{cncs,m}$ and $T'_{cncs,m}$ will be equal; otherwise, they will differ. The difference is a measure of the non-linearity of the Juno radiometer.

For example, assuming that the CNCS output is T_i in Figure 5.3, the radiometer output will be C_L if the radiometer is linear. Using the CNCS ColdFET and Reference Load, the radiometer input can be estimated if the effect of the noise uncertainty is ignored. If the radiometer is nonlinear, the radiometer input and the estimated input will be different. The radiometer output will be larger than C_L if the radiometer has gain expansion behavior. The estimated input will be T_e in Figure 5.3 and it's larger than T_i. For a radiometer that has gain compression behavior, the result is opposite.

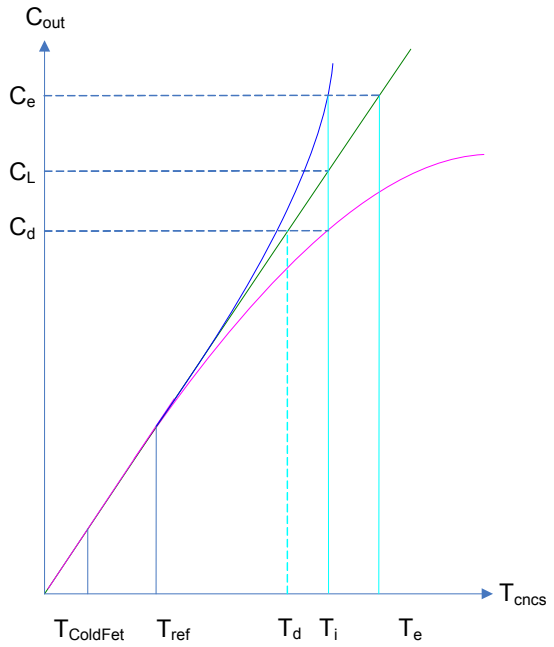

Figure 5.3 Illustration of the linearity

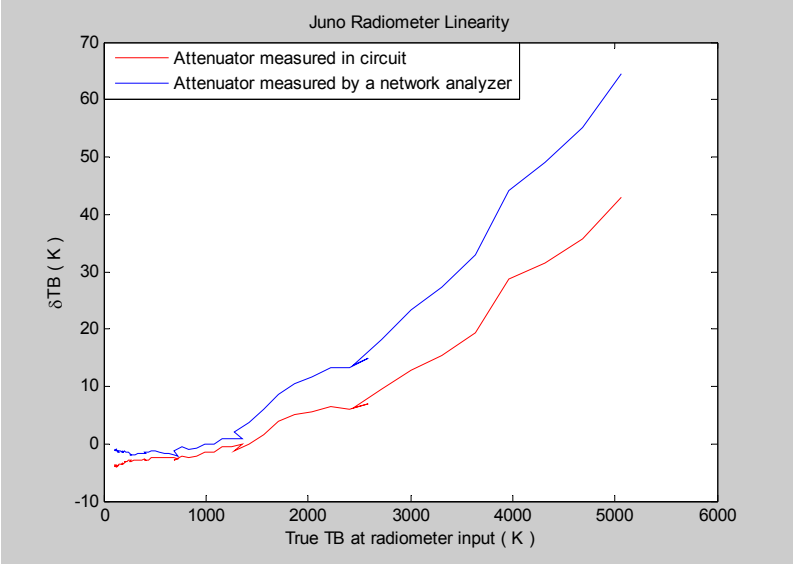

Figure 5.4 Juno BM radiometer linearity

Assuming that the true radiometer input brightness temperature is T_{cncs} and the calibrated input brightness temperature is T'_{cncs}, the difference between them will be given by

$$\delta TB = T'_{cncs} - T_{cncs} \tag{5.2.1}$$

Test results for the Juno radiometer are shown in Figure 5.4. It can be seen that the gain of the Juno radiometer increases with signal strength. This indicates that the radiometer has gain expansion, not compression.

The TB overlap that is evident in Figure 5.4 is due to the overlap of the brightness temperature covered by each lookup table. This also shows the repeatability of the TB when the lookup table is changed.

5.3 Juno Orbit TB Profile Simulation

Orbital TB profile simulations were generated by the CNCS to test the full response of the Juno radiometer in a realistic setting. During the simulation, the CNCS dynamically updates the AWG lookup table and the AWG gain to simulate the Juno orbit brightness temperature profile. Then the radiometer output is compared with the input TB profile.

Figure 5.5 shows the result of the orbit simulation of the TB time series expected during a 30 sec full 360^{o} pitch maneuver by the spacecraft. Figure 5.5a shows a typical Juno orbit TB profile. The extremely high TB values near the center of the time series result from synchrotron emission by Jupiter's radiation belts at L-band. In the Figure, the time series begins with upwelling emission from the Jupiter atmosphere, then sweeps off the planetary limb and begins to encounter the synchrotron emission. Figure 5.5b shows the calibrated brightness temperature. In the middle of the measurements, a marker is added to separate the two orbit TB profile data. There are several glitches which are due to the AWG lookup table switching. These glitches can be easily removed by data processing and the result without glitches is shown in Figure 5.5c.

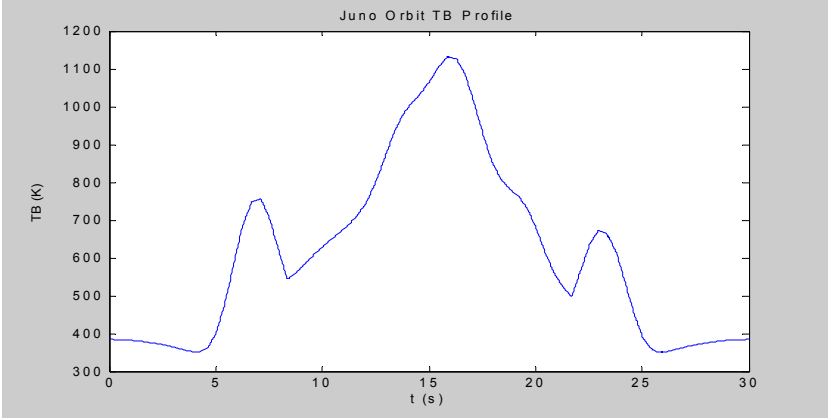

(a) Juno orbit TB profile

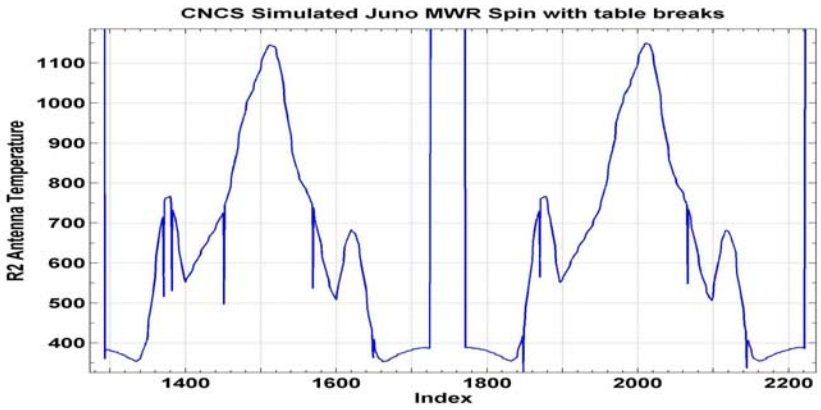

(b) Calibrated TB (*Courtesy of Dr. Shannon Brown, JPL)*

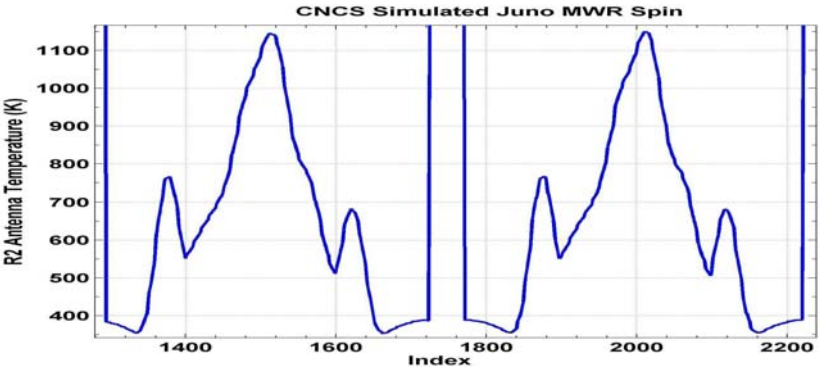

(c) Calibrated TB with glitch removed (*Courtesy of Dr. Shannon Brown, JPL)*

Figure 5.5 Juno orbit simulation

5.4 Summary

The new and improved L-Band CNCS was used to evaluate the Juno breadboard radiometer at JPL. To measure the linearity of the L-band Juno radiometer receiver in broad dynamic range, multiple AWG lookup tables with different standard deviation are used and the CNCS forward model associated with each AWG lookup table is established.

Two approaches are introduced to establish the CNCS forward models with each AWG lookup table. Both approaches need attenuator(s) to vary the CNCS outputs. One approach uses attenuators to bring down the CNCS outputs with each AWG lookup table into the range from the ColdFET brightness to that of the reference load, and then calibrate them with the two calibration sources. With the attenuators measured using a network analyzer, the CNCS forward model in broad dynamic range can be established.

The other approach uses only one attenuator. The attenuator can be measured in-circuit without being affected by the nonlinearity of the radiometer. The radiometer is only used to find the same output for the CNCS with/without the attenuator inserted between the AWG and the RF Head. With one known output which can be recursively derived from the neighboring AWG lookup table and its related CNCS forward model, the CNCS forward model related with its current AWG lookup table can be established, and so on.

For both approaches, the measured linearity of the Juno radiometer is almost the same. Both results show that the Juno radiometer has gain expansion behavior.

With an established CNCS forward model, the CNCS can also generate desired brightness temperatures to simulate the Juno orbit brightness temperature profile.

Although there are glitches in the outputs due to switching between AWG lookup tables, these glitches can be easily removed by data processing.

All of the applications show the flexibility of CNCS and that the CNCS can generate calibration signals over a large dynamic range to calibrate a radiometer.

5.5 Original Contributions and Publication

The original contributions related to the application of CNCS calibration to the Juno radiometer include:

1) CNCS linearization over a large dynamic range;

2) Test the Juno radiometer (L-band) linearity;

3) Juno orbit brightness temperature profile simulation.

One associated paper is published and this paper is also listed in Chapter 4:

1) J. Peng, C.S. Ruf, S. Brown and J. Piepmeier, "*Characterization of the Aquarius and Juno Radiometers Using a Programmable Digital Noise Source*," Proc. 2007 IEEE International Geoscience and Remote Sensing Symposium, Barcelona, SPAIN, 23-27 July, 2007.

Chapter 6

Conclusion

6.1 Contributions

This main theme of this dissertation is the development of the calibration algorithm for a polarimetric radiometer using the Correlated Noise Calibration System (CNCS). We have successfully accomplished this task through several stages of development: (1) the theoretical derivation of the covariance matrix of fully polarimetric radiometer measurements, and its experimental verification; 2) the development of the CNCS forward model; 3) the development of the polarimetric radiometer calibration algorithm; 4) Application to the Aquarius radiometer calibration; 5) CNCS linearization with broad dynamic range of the output brightness temperature signal, with application to the Juno radiometer calibration.

There are in general two types of detection methods used for polarimetric radiometers: coherent detection and incoherent detection. In both cases, the received brightness temperature noise signal and the noise generated internally by the receiver can be modeled as additive, zero mean, white Gaussian noise signals. By modeling the signal flow through all of the components in the radiometers, the covariance matrix of the radiometer measurements has been derived for both types of radiometer detection. For

the incoherent detection case, there are several approaches to form the third and/or fourth Stokes parameters. It is shown that the precision of the resulting measurements (the radiometer NEDT) is the same for each approach, provided the detector sensitivities of the square-law detectors are the same. The radiometer NEDT of the other polarization channels, besides the vertical and horizontal polarization channels, have also been derived. The results have been experimentally verified with a tri-polarimetric radiometer (the DetMit radiometer).

CNCS is a programmable calibration source intended for use by a polarimetric radiometer. The calibration source can generate two channel signals with 'desired' correlation between the signals. Due to hardware limitations, there are non-ideal characteristics of the CNCS and they need to be determined during radiometer calibration. For this reason, a parameterized CNCS forward model has been developed to describe the CNCS characteristics, and its parameters estimated from measurements.

Based on the CNCS forward model and a polarimetric radiometer forward model, a calibration algorithm has been developed. The advantage of this calibration algorithm is that it can calibrate a polarimetric radiometer and at the same time determined the non-ideal characteristics of the CNCS itself. The CNCS channel phase imbalance is estimated by cross-swapping the CNCS output cables. A theoretical analysis shows that the CNCS channel phase imbalance is not retrievable without cross-swapping the CNCS output cables. A Monte-Carlo simulation is used to determine a reasonable calibration data set needed for the calibration algorithm to perform with sufficiently high accuracy. A calibration procedure is described to implement the calibration algorithm. The effect of impedance-mismatches between the CNCS and the radiometer is considered and a

resulting correction is derived for the estimated radiometer gain matrix and offsets. The calibration algorithm is demonstrated using the DetMit radiometer. The retrieved CNCS channel gain imbalance and the CNCS/radiometer channel phase imbalance are validated experimentally. Results show that the polarimetric calibration algorithm can calibrate a polarimetric radiometer effectively with high precision.

The CNCS was used to calibrate the engineering model of the Aquarius radiometer, including the temperature induced phase imbalance characteristics of the Aquarius antenna cables. The effect of errors in calibration of the radiometer channel phase imbalance on the retrieved sea surface salinity has also been analyzed. Results further show that the CNCS can calibrate a polarimetric radiometer with high precision. For example, the uncertainty in the retrieved radiometer channel phase imbalance is 0.02°.

The CNCS has also been linearized over a very wide output dynamic range in order to calibrate the Juno radiometer. Two approaches are developed to establish the CNCS forward models, using multiple AWG lookup tables. In addition, the CNCS can generate a programmable brightness temperature profile in order to simulate the Juno brightness temperature profile expected while in orbit around Jupiter.

6.2 Future Work

The work presented in this dissertation represents the first complete analysis and implementation of polarimetric radiometer calibration using the CNCS, and of its application to radiometers with extremely wide dynamic range. All of the calibration efforts to date have been taken before launch, and the calibration has only applied to

radiometer receivers. Considering these limitations, future work is recommended in following areas:

1) Develop a new and compact CNCS for on-orbit calibration of a space-borne radiometer;

Currently a commercial AWG is used to generate correlated noise signals, and the AWG is mounted in a PXI chassis, so the overall weight and size are not suitable for space application. In addition, most of the complex functions of the AWG are not needed for the CNCS application. For polarimetric radiometer calibration, the lookup tables are fixed and don't need to be dynamically updated. So it should be possible to develop a new and compact CNCS for on-orbit radiometer calibration.

2) Add a known correlated noise source to the CNCS so that cable-swapping isn't required during calibration and develop a new inversion algorithm to support it;

The radiometer channel phase imbalance can't be obtained unless the CNCS channel phase imbalance is known. This could be accomplished if a known, correlated noise source was included in the CNCS, so that an unknown polarimetric radiometer can be calibrated without cross-swapping CNCS output cables. The corresponding calibration algorithm needs to be developed as well.

3) Add an antenna to the CNCS for end-to-end calibration.

Currently, the CNCS can only calibrate a polarimetric radiometer receiver without a radiometer antenna involved. It would be useful to be able to calibrate the complete radiometer system. Because an antenna can't be ideal and the signal can enter the radiometer from the antenna sidelobe, the radiometer calibration will be more complicated.

Appendix 1

Stokes Parameters in Different Coordinate Systems

In a spherical coordinate system, vertically and horizontally polarized signals are defined along the unit vectors $\hat{\theta}$ and $\hat{\phi}$, respectively. Assume that the unit vector $\hat{r}$ is the same as the unit vector $\hat{z}$ in the rectangular coordinate system, or θ = 0. Then the spherical components (vertical component E_θ and horizontal component E_ϕ) of a plane wave are related its rectangular components (E_x and E_y) by [76]

$$E_\theta = E_x \cos\phi + E_y \sin\phi \tag{A1.1a}$$

$$E_\phi = -E_x \sin\phi + E_y \cos\phi \tag{A1.1b}$$

The modified Stokes parameters can be calculated as

$$\begin{aligned} T_{v,\theta\phi} &= \frac{\lambda^2}{k\eta B}\left\{\left|E_x\right|^2 \cos^2\phi + \left|E_y\right|^2 \sin^2\phi + \left(E_y^* E_x + E_y E_x^*\right)\sin\phi\cos\phi\right\} \\ &= \frac{\lambda^2}{k\eta B}\left\{\left|E_x\right|^2 \cos^2\phi + \left|E_y\right|^2 \sin^2\phi + \mathrm{Re}\left\{E_y E_x^*\right\}\sin 2\phi\right\} \end{aligned} \tag{A1.2a}$$

$$\begin{aligned} T_{h,\theta\phi} &= \frac{\lambda^2}{k\eta B}\left\{\left|E_x\right|^2 \sin^2\phi + \left|E_y\right|^2 \cos^2\phi - \left(E_y^* E_x + E_y E_x^*\right)\sin\phi\cos\phi\right\} \\ &= \frac{\lambda^2}{k\eta B}\left\{\left|E_x\right|^2 \sin^2\phi + \left|E_y\right|^2 \cos^2\phi - \mathrm{Re}\left\{E_y E_x^*\right\}\sin 2\phi\right\} \end{aligned} \tag{A1.2b}$$

$$T_{3,\theta\phi} = 2\frac{\lambda^2}{k\eta B}\mathrm{Re}\left\{E_\theta E_\phi^*\right\} = \frac{\lambda^2}{k\eta B}\left\{\left(\left|E_y\right|^2 - \left|E_x\right|^2\right)\sin 2\phi + 2\,\mathrm{Re}\left\{E_y E_x^*\right\}\cos 2\phi\right\} \tag{A1.2c}$$

$$T_{4,\theta\phi} = 2\frac{\lambda^2}{k\eta B}\mathrm{Im}\left\{E_\theta E_\phi^*\right\} = -2\frac{\lambda^2}{k\eta B}\mathrm{Im}\left\{E_y E_x^*\right\} \tag{A1.2d}$$

where the subscript $\theta\phi$ indicates the use of a spherical coordinate system.

In a rectangular coordinate system, E_x and E_y are defined as horizontal and vertical polarization components, respectively [8, 28]. Then the Stokes parameters in the rectangular coordinate system are defined as

$$\begin{bmatrix} T_{v,xy} \\ T_{h,xy} \\ T_{3,xy} \\ T_{4,xy} \end{bmatrix} = \frac{\lambda^2}{k\eta B}\begin{bmatrix} \left|E_y\right|^2 \\ \left|E_x\right|^2 \\ 2\,\mathrm{Re}\left\{E_y E_x^*\right\} \\ 2\,\mathrm{Im}\left\{E_y E_x^*\right\} \end{bmatrix} \tag{A1.3}$$

Equation (A1.1) can be expressed as

$$T_{v,\theta\phi} = T_{v,xy}\sin^2\phi + T_{h,xy}\cos^2\phi + \frac{T_{3,xy}}{2}\sin 2\phi \tag{A1.4a}$$

$$T_{h,\theta\phi} = T_{v,xy}\cos^2\phi + T_{h,xy}\sin^2\phi - \frac{T_{3,xy}}{2}\sin 2\phi \tag{A1.4b}$$

$$T_{3,\theta\phi} = \left(T_{v,xy} - T_{h,xy}\right)\sin 2\phi + T_{3,xy}\cos 2\phi \tag{A1.4c}$$

$$T_{4,\theta\phi} = -T_{4,xy} \tag{A1.4d}$$

where the subscript *xy* indicates the use of a rectangular coordinate system.

For Stokes parameters, the relations to the modified Stokes parameters are given by

$$I_{\theta\phi} = I_{xy} \tag{A1.5a}$$

$$Q_{\theta\phi} = -Q_{xy}\cos 2\phi + U_{xy}\sin 2\phi \tag{A1.5b}$$

$$U_{\theta\phi} = Q_{xy}\sin 2\phi + U_{xy}\cos 2\phi \tag{A1.5c}$$

$$V_{\theta\phi} = -V_{xy} \tag{A1.5d}$$

Once their axes are overlapped, and $\phi = 0$, Equations (A1.4) and (A1.5) become

$$\begin{bmatrix} T_{v,\theta\phi} \\ T_{h,\theta\phi} \\ T_{3,\theta\phi} \\ T_{4,\theta\phi} \end{bmatrix} = \begin{bmatrix} T_{h,xy} \\ T_{v,xy} \\ T_{3,xy} \\ -T_{4,xy} \end{bmatrix} \tag{A1.6}$$

and

$$\begin{bmatrix} I_{\theta\phi} \\ Q_{\theta\phi} \\ U_{\theta\phi} \\ V_{\theta\phi} \end{bmatrix} = \begin{bmatrix} I_{xy} \\ -Q_{xy} \\ U_{xy} \\ -V_{xy} \end{bmatrix} \tag{A1.7}$$

For $\phi = 90°$

$$\begin{bmatrix} T_{v,\theta\phi} \\ T_{h,\theta\phi} \\ T_{3,\theta\phi} \\ T_{4,\theta\phi} \end{bmatrix} = \begin{bmatrix} T_{v,xy} \\ T_{h,xy} \\ -T_{3,xy} \\ -T_{4,xy} \end{bmatrix} \tag{A1.8}$$

and

$$\begin{bmatrix} I_{\theta\phi} \\ Q_{\theta\phi} \\ U_{\theta\phi} \\ V_{\theta\phi} \end{bmatrix} = \begin{bmatrix} I_{xy} \\ Q_{xy} \\ -U_{xy} \\ -V_{xy} \end{bmatrix} \tag{A1.9}$$

Appendix 2

Covariance of Hybrid Combining Polarimetric Radiometer Signals

The time varying voltages $b_v(t)$ and $b_h(t)$ in (2.2.1) are associated with the *v*- and *h*-pol brightness temperatures observed by the radiometer. Their lag cross correlation is given by [12]

$$\langle b_v(t) b_h(t-\tau) \rangle = \left\{ \frac{T_3}{2} \cos(2\pi f_c \tau) - \frac{T_4}{2} \sin(2\pi f_c \tau) \right\} \text{sinc}(B\tau) \tag{A2.1}$$

The time varying voltages $n_v(t)$ and $n_h(t)$ in (2.2.1) are associated with the noise in the *v*- and *h*-pol channels of the radiometer hardware. The noise generating hardware components are, for the most part, distinct between channels and so their lag cross correlation also satisfies

$$\langle n_v(t) n_h(t-\tau) \rangle = 0 \tag{A2.2}$$

The auto correlation and lag cross correlation between the signals $v_v(t)$ and $v_h(t)$ in (2.2.1) can be expanded as

$$\begin{aligned} R_{v,v}(\tau) &= \langle v_v(t) \cdot v_v(t-\tau) \rangle \\ &= G_v \langle [b_v(t) + n_v(t)] \cdot [b_v(t-\tau) + n_v(t-\tau)] \rangle \\ &= G_v \langle b_v(t) b_v(t-\tau) + n_v(t) n_v(t-\tau) \rangle \\ &= G_v T_{sys,v} \text{sinc}(B\tau) \cos(2\pi f_c \tau) \end{aligned} \tag{A2.3a}$$

$$
\begin{aligned}
R_{h,h}(\tau) &= \langle v_h(t)\cdot v_h(t-\tau)\rangle \\
&= G_h\langle [b_h(t)+n_h(t)]\cdot[b_h(t-\tau)+n_h(t-\tau)]\rangle \\
&= G_h\langle b_h(t)b_h(t-\tau)+n_h(t)n_h(t-\tau)\rangle \\
&= G_h T_{sys,h}\,\mathrm{sinc}(B\tau)\cos(2\pi f_c\tau)
\end{aligned}
\tag{A2.3b}
$$

$$
\begin{aligned}
R_{v,h}(\tau) &= \langle v_v(t)\cdot v_h(t-\tau)\rangle \\
&= \sqrt{G_vG_h}\langle [b_v(t)+n_v(t)]\cdot[b_h(t-\tau)+n_h(t-\tau)]\rangle \\
&= \sqrt{G_vG_h}\left\{\frac{T_3}{2}\cos(2\pi f_c\tau)-\frac{T_4}{2}\sin(2\pi f_c\tau)\right\}\mathrm{sinc}(B\tau)
\end{aligned}
\tag{A2.3c}
$$

$$
\begin{aligned}
R_{h,v}(\tau) &= \langle v_h(t)\cdot v_v(t-\tau)\rangle \\
&= \sqrt{G_hG_v}\langle [b_h(t)+n_h(t)]\cdot[b_v(t-\tau)+n_v(t-\tau)]\rangle \\
&= \sqrt{G_hG_v}\left\{\frac{T_3}{2}\cos(2\pi f_c\tau)+\frac{T_4}{2}\sin(2\pi f_c\tau)\right\}\mathrm{sinc}(B\tau)
\end{aligned}
\tag{A2.3d}
$$

where $T_{sys,v} = T_v + T_{Rv}$ and $T_{sys,h} = T_h + T_{Rh}$ are the equivalent system noise temperatures of the *v*- and *h*-pol channels respectively.

Useful higher order auto and cross correlation statistics for $v_v(t)$ and $v_h(t)$ can be written in terms of the 2nd order statistics using the identity $\langle abcd\rangle = \langle ab\rangle\langle cd\rangle + \langle ac\rangle\langle bd\rangle + \langle ad\rangle\langle bc\rangle$, which is valid for zero mean, gaussian distributed random variables [1]. These higher order moments are

$$\langle v_v^2(t)v_v^2(t-\tau)\rangle = R_{v,v}^2(0) + 2R_{v,v}^2(\tau) \tag{A2.4a}$$

$$\langle v_v^2(t)v_h^2(t-\tau)\rangle = R_{v,v}(0)R_{h,h}(0) + 2R_{v,h}^2(\tau) \tag{A2.4b}$$

$$\langle v_v^2(t)v_v(t-\tau)v_h(t-\tau)\rangle = R_{v,v}(0)R_{v,h}(0) + 2R_{v,v}(\tau)R_{v,h}(\tau) \tag{A2.4c}$$

$$\langle v_h^2(t)v_h^2(t-\tau)\rangle = R_{h,h}^2(0) + 2R_{h,h}^2(\tau) \tag{A2.4d}$$

$$\langle v_h^2(t)v_v^2(t-\tau)\rangle = R_{v,v}(0)R_{h,h}(0) + 2R_{h,v}^2(\tau) \tag{A2.4e}$$

$$\left\langle v_h^2(t)v_v(t-\tau)v_h(t-\tau)\right\rangle = R_{h,h}(0)R_{v,h}(0) + 2R_{h,h}(\tau)R_{h,v}(\tau) \tag{A2.4f}$$

$$\left\langle v_v(t)v_h(t)v_v^2(t-\tau)\right\rangle = R_{v,v}(0)R_{v,h}(0) + 2R_{v,v}(\tau)R_{h,v}(\tau) \tag{A2.4g}$$

$$\left\langle v_v(t)v_h(t)v_h^2(t-\tau)\right\rangle = R_{h,h}(0)R_{v,h}(0) + 2R_{h,h}(\tau)R_{v,h}(\tau) \tag{A2.4h}$$

$$\left\langle v_v(t)v_h(t)v_v(t-\tau)v_h(t-\tau)\right\rangle = R_{v,h}^2(0) + R_{v,v}(\tau)R_{h,h}(\tau) + R_{v,h}(\tau)R_{h,v}(\tau) \tag{A2.4i}$$

In order to derive the auto correlation and lag cross correlation of the output signals from the radiometer, $x_v(t)$, $x_P(t)$, $x_M(t)$, $x_h(t)$, $x_L(t)$ and $x_R(t)$, the auto correlation and lag cross correlation of the intermediate signals entering the low pass filters, $w_v(t)$, $w_P(t)$, $w_M(t)$, $w_h(t)$, $w_L(t)$ and $w_R(t)$ in (10), must first be determined. The auto correlation of $w_v(t)$ can be expanded as

$$\begin{aligned} R_{wv,wv}(\tau) &= \left\langle w_v(t)w_v(t-\tau)\right\rangle \\ &= c_v^2\left\langle v_v^2(t)v_v^2(t-\tau)\right\rangle \\ &= c_v^2\left\{R_{v,v}^2(0) + 2R_{v,v}^2(\tau)\right\} \\ &= c_v^2G_v^2T_{sys,v}^2 + c_v^2G_v^2T_{sys,v}^2\cdot\mathrm{sinc}^2(B\tau)\left[1+\cos(4\pi f_c\tau)\right] \\ &= c_v^2G_v^2T_{sys,v}^2\left[1+\mathrm{sinc}^2(B\tau)\right] + c_v^2G_v^2T_{sys,v}^2\mathrm{sinc}^2(B\tau)\cos(4\pi f_c\tau) \end{aligned} \tag{A2.5a}$$

The cross-correlation between $w_v(t)$ and $w_P(t)$ can be expanded as

$$
\begin{aligned}
R_{wv,wP}(\tau) = R_{wP,wv}(-\tau) &= \left\langle w_v(t) w_P(t-\tau) \right\rangle \\
&= \frac{c_v c_P}{2} \left\langle v_v^2(t) \left[v_v(t-\tau) + v_h(t-\tau) \right]^2 \right\rangle \\
&= \frac{c_v c_P}{2} \left\langle v_v^2(t) v_v^2(t-\tau) + 2 v_v^2(t) v_v(t-\tau) v_h(t-\tau) + v_v^2(t) v_h^2(t-\tau) \right\rangle \\
&= \frac{c_v c_P}{2} \left\langle R_{v,v}^2(0) + 2R_{v,v}^2(\tau) + 2R_{v,v}(0) R_{v,h}(0) \right\rangle \\
&\quad + \frac{c_v c_P}{2} \left\langle 4R_{v,v}(\tau) R_{v,h}(\tau) + R_{v,v}(0) R_{h,h}(0) + 2R_{v,h}^2(\tau) \right\rangle \\
&= \frac{c_v c_P}{2} G_v^2 T_{sys,v} \left\{ T_{sys,v} + \sqrt{g} T_3 + g T_{sys,h} \right\} \\
&\quad + \frac{c_v c_P}{2} G_v^2 \left\{ \left(T_{sys,v} + \frac{\sqrt{g}}{2} T_3 \right)^2 + \frac{g}{4} T_4^2 \right\} \operatorname{sinc}^2(B\tau) \\
&\quad + \frac{c_v c_P}{2} G_v^2 \left\{ \left(T_{sys,v} + \frac{\sqrt{g}}{2} T_3 \right)^2 - \frac{g}{4} T_4^2 \right\} \operatorname{sinc}^2(B\tau) \cos(4\pi f_c \tau) \\
&\quad + \frac{c_v c_P}{2} G_v^2 \left\{ -\sqrt{g} T_{sys,v} T_4 - \frac{g}{2} T_3 T_4 \right\} \operatorname{sinc}^2(B\tau) \sin(4\pi f_c \tau)
\end{aligned}
\tag{A2.5b}
$$

Similarly, the other relevant auto correlations and lag cross correlations can be expanded as

$$
\begin{aligned}
R_{wv,wM}(\tau) = R_{wM,wv}(-\tau) &= \left\langle w_{wv}(t) w_{wM}(t-\tau) \right\rangle \\
&= \frac{c_v c_M}{2} \left\langle v_v^2(t) \left[v_v(t-\tau) - v_h(t-\tau) \right]^2 \right\rangle \\
&= \frac{c_v c_M}{2} \left\langle v_v^2(t) v_v^2(t-\tau) - 2 v_v^2(t) v_v(t-\tau) v_h(t-\tau) + v_v^2(t) v_h^2(t-\tau) \right\rangle \\
&= \frac{c_v c_M}{2} \left\langle R_{v,v}^2(0) + 2R_{v,v}^2(\tau) - 2R_{v,v}(0) R_{v,h}(0) \right\rangle \\
&\quad + \frac{c_v c_M}{2} \left\langle -4R_{v,v}(\tau) R_{v,h}(\tau) + R_{v,v}(0) R_{h,h}(0) + 2R_{v,h}^2(\tau) \right\rangle \\
&= \frac{c_v c_M}{2} G_v^2 T_{sys,v} \left\{ T_{sys,v} - \sqrt{g} T_3 + g T_{sys,h} \right\} \\
&\quad + \frac{c_v c_M}{2} G_v^2 \left\{ \left(T_{sys,v} - \frac{\sqrt{g}}{2} T_3 \right)^2 + \frac{g}{4} T_4^2 \right\} \operatorname{sinc}^2(B\tau) \\
&\quad + \frac{c_v c_M}{2} G_v^2 \left\{ \left(T_{sys,v} - \frac{\sqrt{g}}{2} T_3 \right)^2 - \frac{g}{4} T_4^2 \right\} \operatorname{sinc}^2(B\tau) \cos(4\pi f_c \tau) \\
&\quad + \frac{c_v c_M}{2} G_v^2 \left\{ \sqrt{g} T_{sys,v} T_4 - \frac{g}{2} T_3 T_4 \right\} \operatorname{sinc}^2(B\tau) \sin(4\pi f_c \tau)
\end{aligned}
\tag{A2.5c}
$$

$$
\begin{aligned}
R_{wv,wh}(\tau) = R_{wh,wv}(-\tau) &= \langle w_v(t) w_h(t-\tau) \rangle \\
&= c_v c_h \langle v_v^2(t) v_h^2(t-\tau) \rangle \\
&= c_v c_h \{ R_{v,v}(0) R_{h,h}(0) + 2R_{v,h}^2(\tau) \} \\
&= c_v c_h G_v^2 g T_{sys,v} T_{sys,h} \\
&\quad + \frac{c_v c_h}{4} G_v^2 g \{ T_3^2 + T_4^2 \} \mathrm{sinc}^2(B\tau) \\
&\quad + \frac{c_v c_h}{4} G_v^2 g \{ T_3^2 - T_4^2 \} \mathrm{sinc}^2(B\tau) \cos(4\pi f_c \tau) \\
&\quad + \frac{c_v c_h}{4} G_v^2 g \{ -2T_3 T_4 \} \mathrm{sinc}^2(B\tau) \sin(4\pi f_c \tau)
\end{aligned}
\qquad \text{(A2.5d)}
$$

$$
\begin{aligned}
R_{wv,wL}(\tau) = R_{wL,wv}(-\tau) &= \langle w_v(t) w_L(t-\tau) \rangle \\
&= \frac{c_v c_L}{2} \left\langle v_v^2(t) \cdot \left[v_h(t-\tau) + v_v(t-\tau-\frac{1}{4f_c}) \right]^2 \right\rangle \\
&= \frac{c_v c_L}{2} \left\{ \langle v_v^2(t) v_h^2(t-\tau) \rangle + \left\langle v_v^2(t) v_v^2(t-\tau-\frac{1}{4f_c}) \right\rangle \right\} \\
&\quad + \frac{c_v c_L}{2} \left\langle 2v_v^2(t) v_h(t-\tau) v_v(t-\tau-\frac{1}{4f_c}) \right\rangle \\
&= \frac{c_v c_L}{2} \left\{ R_{v,v}(0) R_{h,h}(0) + 2R_{v,h}^2(\tau) + R_{v,v}^2(0) + 2R_{v,v}^2(\tau+\frac{1}{4f_c}) \right\} \\
&\quad + \frac{c_v c_L}{2} \left\{ 2R_{v,v}(0) R_{h,v}(\frac{1}{4f_c}) + 4R_{v,h}(\tau) R_{v,v}(\tau+\frac{1}{4f_c}) \right\} \\
&\approx \frac{c_v c_L}{2} G_v^2 T_{sys,v} \{ T_{sys,v} + g T_{sys,h} + \sqrt{g} T_4 \} \\
&\quad + \frac{c_v c_L}{2} G_v^2 \left\{ \frac{g}{4} \left(T_3^2 + T_4^2 \right) + T_{sys,v}^2 + \sqrt{g} T_{sys,v} T_4 \right\} \mathrm{sinc}^2(B\tau) \\
&\quad + \frac{c_v c_L}{2} G_v^2 \left\{ \frac{g}{4} \left(T_3^2 - T_4^2 \right) - T_{sys,v}^2 - \sqrt{g} T_{sys,v} T_4 \right\} \mathrm{sinc}^2(B\tau) \cos(4\pi f_c \tau) \\
&\quad + \frac{c_v c_L}{2} G_v^2 \left\{ -\frac{g}{2} T_3 T_4 - \sqrt{g} T_{sys,v} T_3 \right\} \mathrm{sinc}^2(B\tau) \sin(4\pi f_c \tau)
\end{aligned}
\qquad \text{(A2.5e)}
$$

where $\mathrm{sinc}(B\tau + B\frac{1}{4f_c}) \approx \mathrm{sinc}(B\tau)$ *for* $B << f_c$.

$$
\begin{aligned}
R_{cv,cR}(\tau) = R_{cR,cv}(-\tau) &= \left\langle w_v(t) w_R(t-\tau) \right\rangle \\
&= \frac{c_v c_R}{2} \left\langle v_v^2(t) \cdot \left[v_h(t-\tau) - v_v(t-\tau-\frac{1}{4f_c}) \right]^2 \right\rangle \\
&= \frac{c_v c_R}{2} \left\{ \left\langle v_v^2(t) v_h^2(t-\tau) \right\rangle + \left\langle v_v^2(t) v_v^2(t-\tau-\frac{1}{4f_c}) \right\rangle \right\} \\
&\quad - \frac{c_v c_R}{2} \left\langle 2 v_v^2(t) v_h(t-\tau) v_v(t-\tau-\frac{1}{4f_c}) \right\rangle \\
&= \frac{c_v c_R}{2} \left\{ R_{v,v}(0) R_{h,h}(0) + 2R_{v,h}^2(\tau) + R_{v,v}^2(0) + 2R_{v,v}^2(\tau+\frac{1}{4f_c}) \right\} \\
&= \frac{c_v c_R}{2} \left\{ -2R_{v,v}(0) R_{h,v}(\frac{1}{4f_c}) - 4R_{v,h}(\tau) R_{v,v}(\tau+\frac{1}{4f_c}) \right\} \\
&\approx \frac{c_v c_R}{2} G_v^2 T_{sys,v} \left\{ T_{sys,v} + g T_{sys,h} - \sqrt{g} T_4 \right\} \\
&\quad + \frac{c_v c_R}{2} G_v^2 \left\{ \frac{g}{4} \left(T_3^2 + T_4^2 \right) + T_{sys,v}^2 - \sqrt{g} T_{sys,v} T_4 \right\} \operatorname{sinc}^2(B\tau) \\
&\quad + \frac{c_v c_R}{2} G_v^2 \left\{ \frac{g}{4} \left(T_3^2 - T_4^2 \right) - T_{sys,v}^2 + \sqrt{g} T_{sys,v} T_4 \right\} \operatorname{sinc}^2(B\tau) \cos(4\pi f_c \tau) \qquad \text{(A2.5f)} \\
&\quad + \frac{c_v c_R}{2} G_v^2 \left\{ -\frac{g}{2} T_3 T_4 + \sqrt{g} T_{sys,v} T_3 \right\} \operatorname{sinc}^2(B\tau) \sin(4\pi f_c \tau)
\end{aligned}
$$

$$
\begin{aligned}
R_{wP,wP}(\tau) &= \left\langle w_P(t) w_P(t-\tau) \right\rangle = \frac{c_P^2}{4} \left\langle \left[v_v(t) + v_h(t) \right]^2 \left[v_v(t-\tau) + v_h(t-\tau) \right]^2 \right\rangle \\
&= \frac{c_P^2}{4} \left\langle \left[v_v^2(t) + v_h^2(t) + 2 v_v(t) \cdot v_h(t) \right] \cdot \left[v_v^2(t-\tau) + v_h^2(t-\tau) + 2 v_v(t-\tau) \cdot v_h(t-\tau) \right] \right\rangle \\
&= \frac{c_P^2}{4} \left\{ R_{v,v}^2(0) + 2 R_{v,v}(0) R_{h,h}(0) + R_{h,h}^2(0) + 4 R_{v,v}(0) R_{v,h}(0) + 4 R_{h,h}(0) R_{v,h}(0) + 4 R_{v,h}^2(0) \right\} \\
&\quad + \frac{c_P^2}{4} \left\{ 2 R_{v,v}^2(\tau) + 2 R_{v,h}^2(\tau) + 2 R_{h,v}^2(\tau) + 2 R_{h,h}^2(\tau) \right\} \\
&\quad + \frac{c_P^2}{4} \left\{ 4 R_{v,v}(\tau) R_{v,h}(\tau) + 4 R_{v,v}(\tau) R_{h,v}(\tau) + 4 R_{v,v}(\tau) R_{h,h}(\tau) \right\} \\
&\quad + \frac{c_P^2}{4} \left\{ 4 R_{h,h}(\tau) R_{v,h}(\tau) + 4 R_{h,h}(\tau) R_{h,v}(\tau) + 4 R_{v,h}(\tau) R_{h,v}(\tau) \right\} \\
&= \frac{c_P^2}{4} G_v^2 \left\{ T_{sys,v} + g T_{sys,h} + \sqrt{g} T_3 \right\}^2 \\
&\quad + \frac{c_P^2}{4} G_v^2 \left\{ T_{sys,v} + g T_{sys,h} + \sqrt{g} T_3 \right\}^2 \operatorname{sinc}^2(B\tau) \\
&\quad + \frac{c_P^2}{4} G_v^2 \left\{ T_{sys,v} + g T_{sys,h} + \sqrt{g} T_3 \right\}^2 \operatorname{sinc}^2(B\tau) \cos(4\pi f_c \tau)
\end{aligned}
\tag{A2.5g}
$$

$$R_{wP,wM}(\tau) = R_{wM,wP}(-\tau) = \langle w_P(t) w_M(t-\tau) \rangle = \frac{c_P c_M}{4} \left\langle \left[v_v(t) + v_h(t) \right]^2 \left[v_v(t-\tau) - v_h(t-\tau) \right]^2 \right\rangle$$

$$= \frac{c_P c_M}{4} \left\langle \left[v_v^2(t) + v_h^2(t) + 2 v_v(t) \cdot v_h(t) \right] \cdot \left[v_v^2(t-\tau) + v_h^2(t-\tau) - 2 v_v(t-\tau) \cdot v_h(t-\tau) \right] \right\rangle$$

$$= \frac{c_P c_M}{4} \left\{ R_{v,v}^2(0) + 2 R_{v,v}(0) R_{h,h}(0) + R_{h,h}^2(0) - 4 R_{v,h}^2(0) \right\}$$

$$+ \frac{c_P c_M}{4} \left\{ 2 R_{v,v}^2(\tau) + 2 R_{v,h}^2(\tau) + 2 R_{h,v}^2(\tau) + 2 R_{h,h}^2(\tau) \right\}$$

$$+ \frac{c_P c_M}{4} \left\{ -4 R_{v,v}(\tau) R_{v,h}(\tau) + 4 R_{v,v}(\tau) R_{h,v}(\tau) - 4 R_{v,v}(\tau) R_{h,h}(\tau) \right\}$$

$$+ \frac{c_P c_M}{4} \left\{ -4 R_{h,h}(\tau) R_{h,v}(\tau) + 4 R_{h,h}(\tau) R_{v,h}(\tau) - 4 R_{v,h}(\tau) R_{h,v}(\tau) \right\}$$

$$= \frac{c_P c_M}{4} G_v^2 \left\{ \left(T_{sys,v} + g T_{sys,h} \right)^2 - g T_3^2 \right\}$$

$$+ \frac{c_P c_M}{4} G_v^2 \left\{ \left(T_{sys,v} - g T_{sys,h} \right)^2 + g T_4^2 \right\} \mathrm{sinc}^2(B\tau)$$

$$+ \frac{c_P c_M}{4} G_v^2 \left\{ \left(T_{sys,v} - g T_{sys,h} \right)^2 - g T_4^2 \right\} \mathrm{sinc}^2(B\tau) \cos(4\pi f_c \tau)$$

$$+ \frac{c_P c_M}{4} G_v^2 \sqrt{g} \left\{ T_{sys,v} - g T_{sys,h} \right\} T_4 \mathrm{sinc}^2(B\tau) \sin(4\pi f_c \tau)$$

(A2.5h)

$$R_{wP,wh}(\tau) = R_{wh,wP}(-\tau) = \langle w_P(t) w_h(t-\tau) \rangle = \frac{c_P c_h}{2} \left\langle \left[v_v(t) + v_h(t) \right]^2 v_h^2(t-\tau) \right\rangle$$

$$= \frac{c_P c_h}{2} \left\langle v_v^2(t) v_h^2(t-\tau) + v_h^2(t) v_h^2(t-\tau) + 2 v_v(t) \cdot v_h(t) v_h^2(t-\tau) \right\rangle$$

$$= \frac{c_P c_h}{2} \left\{ 2 R_{v,v}(0) R_{h,h}(0) + 4 R_{v,h}^2(\tau) + 2 R_{h,h}^2(0) \right\}$$

$$+ \frac{c_P c_h}{2} \left\{ 4 R_{h,h}^2(\tau) + 4 R_{h,h}(0) R_{v,h}(0) + 8 R_{h,h}(\tau) R_{v,h}(\tau) \right\}$$

$$= \frac{c_P c_h}{2} G_v^2 g T_{sys,h} \left\{ T_{sys,v} + g T_{sys,h} + \sqrt{g} T_3 \right\}$$

$$+ \frac{c_P c_h}{2} G_v^2 \left\{ \left(g T_{sys,h} + \frac{\sqrt{g}}{2} T_3 \right)^2 + \frac{g}{4} T_4^2 \right\} \mathrm{sinc}^2(B\tau)$$

$$+ \frac{c_P c_h}{2} G_v^2 \left\{ \left(g T_{sys,h} + \frac{\sqrt{g}}{2} T_3 \right)^2 - \frac{g}{4} T_4^2 \right\} \mathrm{sinc}^2(B\tau) \cos(4\pi f_c \tau)$$

$$+ \frac{c_P c_h}{2} G_v^2 g \left\{ -\frac{T_3}{2} - \sqrt{g} T_{sys,h} \right\} T_4 \mathrm{sinc}^2(B\tau) \sin(4\pi f_c \tau)$$

(A2.5i)

$$
\begin{aligned}
R_{wP,wL}(\tau) = R_{wL,wP}(-\tau) &= \left\langle w_P(t) w_L(t-\tau) \right\rangle \\
&= \frac{c_P c_L}{4} \left\langle \left[v_v(t) + v_h(t) \right]^2 \left[v_h(t-\tau) + v_v(t-\tau-\frac{1}{4f_c}) \right]^2 \right\rangle \\
&= \frac{c_P c_L}{4} \left\langle \left[v_v(t) + v_h(t) \right]^2 v_h^2(t-\tau) + \left[v_v(t) + v_h(t) \right]^2 v_v^2(t-\tau-\frac{1}{4f_c}) \right\rangle \\
&\quad + \frac{c_P c_L}{4} \left\langle 2\left[v_v(t) + v_h(t) \right]^2 v_h(t-\tau) v_v(t-\tau-\frac{1}{4f_c}) \right\rangle \\
&= \frac{c_P c_L}{4} G_v^2 \left(T_{sys,v} + g T_{sys,h} + \sqrt{g} T_3 \right) \left(T_{sys,v} + g T_{sys,h} + \sqrt{g} T_4 \right) \\
&\quad + \frac{c_P c_L}{4} G_v^2 \left\{ \left[T_{sys,v} + \frac{\sqrt{g}}{2} \left(T_3 + T_4 \right) \right]^2 + \left[g T_{sys,h} + \frac{\sqrt{g}}{2} \left(T_3 + T_4 \right) \right]^2 \right\} \operatorname{sinc}^2(B\tau) \\
&\quad + \frac{c_P c_L}{4} G_v^2 \left\{ \left(g T_{sys,h} + \frac{\sqrt{g}}{2} T_3 \right)^2 - \left(T_{sys,v} + \frac{\sqrt{g}}{2} T_3 \right)^2 \right\} \operatorname{sinc}^2(B\tau) \cos(4\pi f_c \tau) \\
&\quad + \frac{c_P c_L}{4} G_v^2 \left\{ -\sqrt{g} T_4 \left(T_{sys,v} - g T_{sys,h} \right) \right\} \operatorname{sinc}^2(B\tau) \cos(4\pi f_c \tau) \\
&\quad + \frac{c_P c_L}{4} G_v^2 \left\{ -g T_3 T_4 - \sqrt{g} \left(T_3 + T_4 \right) \left(T_{sys,v} + g T_{sys,h} \right) \right\} \operatorname{sinc}^2(B\tau) \sin(4\pi f_c \tau) \\
&\quad + \frac{c_P c_L}{4} G_v^2 \left\{ -2 g T_{sys,v} T_{sys,h} - \frac{g}{2} \left(T_3^2 + T_4^2 \right) \right\} \operatorname{sinc}^2(B\tau) \sin(4\pi f_c \tau)
\end{aligned}
\qquad \text{(A2.5j)}
$$

$$
\begin{aligned}
R_{wP,wR}(\tau) = R_{wR,wP}(-\tau) &= \left\langle w_P(t) w_R(t-\tau) \right\rangle \\
&= \frac{c_P c_R}{4} \left\langle \left[v_v(t) + v_h(t) \right]^2 \left[v_h(t) - v_v(t - \frac{1}{4 f_c}) \right]^2 \right\rangle \\
&= \frac{c_P c_R}{4} \left\langle \left[v_v(t) + v_h(t) \right]^2 v_h^2(t-\tau) + \left[v_v(t) + v_h(t) \right]^2 v_v^2(t - \tau - \frac{1}{4 f_c}) \right\rangle \\
&\quad + \frac{c_P c_R}{4} \left\langle -2 \left[v_v(t) + v_h(t) \right]^2 v_h(t-\tau) v_v(t - \tau - \frac{1}{4 f_c}) \right\rangle \\
&= \frac{c_P c_R}{4} G_v^2 \left(T_{sys,v} + g T_{sys,h} + \sqrt{g} T_3 \right) \cdot \left(T_{sys,v} + g T_{sys,h} - \sqrt{g} T_4 \right) \\
&\quad + \frac{c_P c_R}{4} G_v^2 \left\{ \left[T_{sys,v} + \frac{\sqrt{g}}{2} \left(T_3 - T_4 \right) \right]^2 + \left[g T_{sys,h} + \frac{\sqrt{g}}{2} \left(T_3 - T_4 \right) \right]^2 \right\} \operatorname{sinc}^2(B\tau) \\
&\quad + \frac{c_P c_R}{4} G_v^2 \left\{ \left(g T_{sys,h} + \frac{\sqrt{g}}{2} T_3 \right)^2 - \left(T_{sys,v} + \frac{\sqrt{g}}{2} T_3 \right)^2 \right\} \operatorname{sinc}^2(B\tau) \cos(4\pi f_c \tau) \\
&\quad + \frac{c_P c_R}{4} G_v^2 \left\{ \sqrt{g} T_4 \left(T_{sys,v} - g T_{sys,h} \right) \right\} \operatorname{sinc}^2(B\tau) \cos(4\pi f_c \tau) \\
&\quad + \frac{c_P c_R}{4} G_v^2 \left\{ -g T_3 T_4 + \sqrt{g} \left(T_3 - T_4 \right) \left(T_{sys,v} + g T_{sys,h} \right) \right\} \operatorname{sinc}^2(B\tau) \sin(4\pi f_c \tau) \\
&\quad + \frac{c_P c_R}{4} G_v^2 \left\{ 2 g T_{sys,v} T_{sys,h} + \frac{g}{2} \left(T_3^2 + T_4^2 \right) \right\} \operatorname{sinc}^2(B\tau) \sin(4\pi f_c \tau)
\end{aligned}
\tag{A2.5k}
$$

$$
\begin{aligned}
R_{wM,wM}(\tau) = \left\langle w_M(t) w_M(t-\tau) \right\rangle &= \frac{c_M^2}{4} \left\langle \left[v_v(t) - v_h(t) \right]^2 \left[v_v(t-\tau) - v_h(t-\tau) \right]^2 \right\rangle \\
&= \frac{c_M^2}{4} \left\langle \left[v_v^2(t) + v_h^2(t) - 2 v_v(t) \cdot v_h(t) \right] \cdot \left[v_v^2(t-\tau) + v_v^2(t-\tau) - 2 v_v(t-\tau) \cdot v_h(t-\tau) \right] \right\rangle \\
&= \frac{c_M^2}{4} \left\{ R_{v,v}^2(0) + 2 R_{v,v}(0) R_{h,h}(0) + R_{h,h}^2(0) - 4 R_{v,v}(0) R_{v,h}(0) - 4 R_{h,h}(0) R_{v,h}(0) + 4 R_{v,h}^2(0) \right\} \\
&\quad + \frac{c_M^2}{4} \left\{ 2 R_{v,v}^2(\tau) + 2 R_{v,h}^2(\tau) + 2 R_{h,v}^2(\tau) + 2 R_{h,h}^2(\tau) \right\} \\
&\quad + \frac{c_M^2}{4} \left\{ -4 R_{v,v}(\tau) R_{v,h}(\tau) - 4 R_{v,v}(\tau) R_{h,v}(\tau) + 4 R_{v,v}(\tau) R_{h,h}(\tau) \right\} \\
&\quad + \frac{c_M^2}{4} \left\{ -4 R_{h,h}(\tau) R_{v,h}(\tau) - 4 R_{h,h}(\tau) R_{h,v}(\tau) + 4 R_{v,h}(\tau) R_{h,v}(\tau) \right\} \\
&= \frac{c_M^2}{4} G_v^2 \left\{ T_{sys,v} + g T_{sys,h} - \sqrt{g} T_3 \right\}^2 \\
&\quad + \frac{c_M^2}{4} G_v^2 \left\{ T_{sys,v} + g T_{sys,h} - \sqrt{g} T_3 \right\}^2 \operatorname{sinc}^2(B\tau) \\
&\quad + \frac{c_M^2}{4} G_v^2 \left\{ T_{sys,v} + g T_{sys,h} - \sqrt{g} T_3 \right\}^2 \operatorname{sinc}^2(B\tau) \cos(4\pi f_c \tau)
\end{aligned}
\tag{A2.5l}
$$

$$
\begin{aligned}
R_{wM,wh}(\tau) = R_{wh,wM}(-\tau) &= \langle w_M(t) w_h(t-\tau) \rangle = \frac{c_M c_h}{2} \left\langle \left[v_v(t) - v_h(t) \right]^2 v_h^2(t-\tau) \right\rangle \\
&= \frac{c_M c_h}{2} \left\langle v_v^2(t) v_h^2(t-\tau) + v_h^2(t) v_h^2(t-\tau) - 2 v_v(t) \cdot v_h(t) v_h^2(t-\tau) \right\rangle \\
&= \frac{c_M c_h}{2} \left\{ R_{v,v}(0) R_{h,h}(0) + 2R_{v,h}^2(\tau) + R_{h,h}^2(0) + 2R_{h,h}^2(\tau) - 2R_{h,h}(0) R_{v,h}(0) - 4R_{h,h}(\tau) R_{v,h}(\tau) \right\} \\
&= \frac{c_M c_h}{2} G_v^2 g T_{sys,h} \left\{ T_{sys,v} + g T_{sys,h} - \sqrt{g} T_3 \right\} \\
&\quad + \frac{c_M c_h}{2} G_v^2 \left\{ \left(g T_{sys,h} - \frac{\sqrt{g}}{2} T_3 \right)^2 + \frac{g}{4} T_4^2 \right\} \operatorname{sinc}^2(B\tau) \\
&\quad + \frac{c_M c_h}{2} G_v^2 \left\{ \left(g T_{sys,h} - \frac{\sqrt{g}}{2} T_3 \right)^2 - \frac{g}{4} T_4^2 \right\} \operatorname{sinc}^2(B\tau) \cos(4\pi f_c \tau) \\
&\quad + \frac{c_M c_h}{2} G_v^2 g \left\{ -\frac{T_3}{2} + \sqrt{g} T_{sys,h} \right\} T_4 \operatorname{sinc}^2(B\tau) \sin(4\pi f_c \tau)
\end{aligned}
\tag{A2.5m}
$$

$$
\begin{aligned}
R_{wM,wL}(\tau) = R_{wL,wM}(-\tau) &= \langle w_M(t) w_L(t-\tau) \rangle \\
&= \frac{c_M c_L}{4} \left\langle \left[v_v(t) - v_h(t) \right]^2 \left[v_h(t-\tau) + v_v(t-\tau - \frac{1}{4f_c}) \right]^2 \right\rangle \\
&= \frac{c_M c_L}{4} \left\langle \left[v_v(t) - v_h(t) \right]^2 v_h^2(t-\tau) + \left[v_v(t) - v_h(t) \right]^2 v_v^2(t-\tau - \frac{1}{4f_c}) \right\rangle \\
&\quad + \frac{c_M c_L}{4} \left\langle 2 \left[v_v(t) - v_h(t) \right]^2 v_h(t-\tau) v_v(t-\tau - \frac{1}{4f_c}) \right\rangle \\
&= \frac{c_M c_L}{4} G_v^2 \left(T_{sys,v} + g T_{sys,h} - \sqrt{g} T_3 \right) \cdot \left(T_{sys,v} + g T_{sys,h} + \sqrt{g} T_4 \right) \\
&\quad + \frac{c_M c_L}{4} G_v^2 \left\{ \left[T_{sys,v} - \frac{\sqrt{g}}{2} \left(T_3 - T_4 \right) \right]^2 + \left[g T_{sys,h} - \frac{\sqrt{g}}{2} \left(T_3 - T_4 \right) \right]^2 \right\} \operatorname{sinc}^2(B\tau) \\
&\quad + \frac{c_M c_L}{4} G_v^2 \left\{ -\left(T_{sys,v} - \frac{\sqrt{g}}{2} T_3 \right)^2 + \left(g T_{sys,h} - \frac{\sqrt{g}}{2} T_3 \right)^2 \right\} \operatorname{sinc}^2(B\tau) \cos(4\pi f_c \tau) \\
&\quad + \frac{c_M c_L}{4} G_v^2 \left\{ -\frac{g}{2} T_4^2 - \sqrt{g} T_4 \left(T_{sys,v} - g T_{sys,h} \right) \right\} \operatorname{sinc}^2(B\tau) \cos(4\pi f_c \tau) \\
&\quad + \frac{c_M c_L}{4} G_v^2 \left\{ \sqrt{g} \left(T_4 - T_3 \right) \left(T_{sys,v} + g T_{sys,h} \right) - g T_3 T_4 \right\} \operatorname{sinc}^2(B\tau) \sin(4\pi f_c \tau) \\
&\quad + \frac{c_M c_L}{4} G_v^2 \left\{ 2 g T_{sys,v} T_{sys,h} + \frac{g}{2} \left(T_3^2 + T_4^2 \right) \right\} \operatorname{sinc}^2(B\tau) \sin(4\pi f_c \tau)
\end{aligned}
\tag{A2.5n}
$$

$$
\begin{aligned}
R_{wM,wR}(\tau) &= R_{wR,wM}(-\tau) = \langle w_M(t) w_R(t-\tau) \rangle \\
&= \frac{c_M c_R}{4} \left\langle [v_v(t) - v_h(t)]^2 \left[v_h(t) - v_v(t - \frac{1}{4f_c}) \right]^2 \right\rangle \\
&= \frac{c_M c_R}{4} \left\langle [v_v(t) - v_h(t)]^2 v_h^2(t-\tau) + [v_v(t) - v_h(t)]^2 v_v^2(t - \tau - \frac{1}{4f_c}) \right\rangle \\
&\quad + \frac{c_M c_R}{4} \left\langle -2[v_v(t) - v_h(t)]^2 v_h(t-\tau) v_v(t - \tau - \frac{1}{4f_c}) \right\rangle \\
&= \frac{c_M c_R}{4} G_v^2 \left(T_{sys,v} + g T_{sys,h} - \sqrt{g} T_3 \right) \cdot \left(T_{sys,v} + g T_{sys,h} - \sqrt{g} T_4 \right) \\
&\quad + \frac{c_M c_R}{4} G_v^2 \left\{ \left[g T_{sys,h} - \frac{\sqrt{g}}{2} (T_3 + T_4) \right]^2 + \left[T_{sys,v} - \frac{\sqrt{g}}{2} (T_3 + T_4) \right]^2 \right\} \operatorname{sinc}^2(B\tau) \\
&\quad + \frac{c_M c_R}{4} G_v^2 \left\{ -\left(T_{sys,v} - \frac{\sqrt{g}}{2} T_3 \right)^2 + \left(g T_{sys,h} - \frac{\sqrt{g}}{2} T_3 \right)^2 \right\} \operatorname{sinc}^2(B\tau) \cos(4\pi f_c \tau) \\
&\quad + \frac{c_M c_R}{4} G_v^2 \left\{ -\frac{g}{2} T_4^2 + \sqrt{g} T_4 \left(T_{sys,v} - g T_{sys,h} \right) \right\} \operatorname{sinc}^2(B\tau) \cos(4\pi f_c \tau) \\
&\quad + \frac{c_M c_R}{4} G_v^2 \left\{ \sqrt{g} (T_3 + T_4) \left(T_{sys,v} + g T_{sys,h} \right) - g T_3 T_4 \right\} \operatorname{sinc}^2(B\tau) \sin(4\pi f_c \tau) \\
&\quad + \frac{c_M c_R}{4} G_v^2 \left\{ -2 g T_{sys,v} T_{sys,h} - \frac{g}{2} \left(T_3^2 + T_4^2 \right) \right\} \operatorname{sinc}^2(B\tau) \sin(4\pi f_c \tau)
\end{aligned}
\tag{A2.5o}
$$

$$
\begin{aligned}
R_{wh,wh}(\tau) &= \langle w_h(t) w_h(t-\tau) \rangle \\
&= c_h^2 \left\langle v_h^2(t) v_h^2(t-\tau) \right\rangle \\
&= c_h^2 \left\{ R_{h,h}^2(0) + 2 R_{h,h}^2(\tau) \right\} \\
&= c_h^2 G_v^2 g^2 T_{sys,h}^2 \left[1 + \operatorname{sinc}^2(B\tau) \right] + c_h^2 G_v^2 g^2 T_{sys,h}^2 \operatorname{sinc}^2(B\tau) \cos(4\pi f_c \tau)
\end{aligned}
\tag{A2.5p}
$$

$$
\begin{aligned}
R_{wh,wL}(\tau) = R_{wL,wh}(-\tau) &= \langle w_h(t) w_L(t-\tau) \rangle \\
&= \frac{c_h c_L}{2} \left\langle v_4^2(t) \left[v_h(t-\tau) + v_v(t-\tau-\frac{1}{4f_c}) \right]^2 \right\rangle \\
&= \frac{c_h c_L}{2} \left\langle v_h^2(t) v_h^2(t-\tau) + v_h^2(t) v_v^2(t-\tau-\frac{1}{4f_c}) + 2 v_h^2(t) v_h(t-\tau) v_v(t-\tau-\frac{1}{4f_c}) \right\rangle \\
&= \frac{c_h c_L}{2} G_v^2 g T_{sys,h} \left\{ T_{sys,v} + g T_{sys,h} + \sqrt{g} T_4 \right\} \\
&\quad + \frac{c_h c_L}{2} G_v^2 \left\{ g^2 T_{sys,h}^2 + \frac{1}{4} g \left(T_3^2 + T_4^2 \right) + \sqrt{g} T_4 g T_{sys,h} \right\} \mathrm{sinc}^2(B\tau) \\
&\quad + \frac{c_h c_L}{2} G_v^2 \left\{ g^2 T_{sys,h}^2 - \frac{1}{4} g \left(T_3^2 - T_4^2 \right) + \sqrt{g} T_4 g T_{sys,h} \right\} \mathrm{sinc}^2(B\tau) \cos(4\pi f_c \tau) \\
&\quad + \frac{c_h c_L}{2} G_v^2 \left\{ -\frac{1}{2} g T_3 T_4 - \sqrt{g} T_3 g T_{sys,h} \right\} \mathrm{sinc}^2(B\tau) \sin(4\pi f_c \tau)
\end{aligned}
$$

(A2.5q)

$$
\begin{aligned}
R_{wh,wR}(\tau) = R_{wR,wh}(-\tau) &= \langle w_h(t) w_R(t-\tau) \rangle \\
&= \frac{c_h c_R}{2} \left\langle v_h^2(t) \left[v_h(t-\tau) - v_v(t-\tau-\frac{1}{4f_c}) \right]^2 \right\rangle \\
&= \frac{c_h c_R}{2} \left\langle v_h^2(t) v_h^2(t-\tau) + v_h^2(t) v_v^2(t-\tau-\frac{1}{4f_c}) - 2 v_h^2(t) v_h(t-\tau) v_v(t-\tau-\frac{1}{4f_c}) \right\rangle \\
&= \frac{c_h c_R}{2} G_v^2 g T_{sys,h} \left\{ T_{sys,v} + g T_{sys,h} - \sqrt{g} T_4 \right\} \\
&\quad + \frac{c_h c_R}{2} G_v^2 \left\{ g^2 T_{sys,h}^2 + \frac{1}{4} g \left(T_3^2 + T_4^2 \right) - \sqrt{g} T_4 g T_{sys,h} \right\} \mathrm{sinc}^2(B\tau) \\
&\quad + \frac{c_h c_R}{2} G_v^2 \left\{ g^2 T_{sys,h}^2 - \frac{1}{4} g \left(T_3^2 - T_4^2 \right) - \sqrt{g} T_4 g T_{sys,h} \right\} \mathrm{sinc}^2(B\tau) \cos(4\pi f_c \tau) \\
&\quad + \frac{c_h c_R}{2} G_v^2 \left\{ -\frac{1}{2} g T_3 T_4 + \sqrt{g} T_3 g T_{sys,h} \right\} \mathrm{sinc}^2(B\tau) \sin(4\pi f_c \tau)
\end{aligned}
$$

(A2.5r)

$$R_{wL,wL}(\tau)=\langle w_L(t)w_L(t-\tau)\rangle=\frac{c_L^2}{4}\left\langle\left[v_h(t)+v_v(t-\frac{1}{4f_c})\right]^2\left[v_h(t-\tau)+v_v(t-\tau-\frac{1}{4f_c})\right]^2\right\rangle$$

$$=\frac{c_L^2}{4}\left\{\left[R_{h,h}(0)+R_{v,v}(0)+2R_{h,v}(\frac{1}{4f_c})\right]^2+2\left[R_{h,h}(\tau)+R_{v,v}(\tau)+R_{h,v}(\tau+\frac{1}{4f_c})+R_{v,h}(\tau-\frac{1}{4f_c})\right]^2\right\}$$

$$=\frac{c_L^2}{4}G_v^2\left(T_{sys,v}+gT_{sys,h}+\sqrt{g}T_4\right)^2$$

$$+\frac{c_L^2}{4}G_v^2\left(T_{sys,v}+gT_{sys,h}+\sqrt{g}T_4\right)^2\mathrm{sinc}^2(B\tau)$$

$$+\frac{c_L^2}{4}G_v^2\left(T_{sys,v}+gT_{sys,h}+\sqrt{g}T_4\right)^2\mathrm{sinc}^2(B\tau)\cos(4\pi f_c\tau)$$

(A2.5s)

$$R_{wL,wR}(\tau)=R_{wR,wL}(-\tau)=\langle w_L(t)w_R(t-\tau)\rangle$$

$$=\frac{c_Lc_R}{4}\left\langle\left[v_h(t)+v_v(t-\frac{1}{4f_c})\right]^2\cdot\left[v_h(t-\tau)-v_v(t-\tau-\frac{1}{4f_c})\right]^2\right\rangle$$

$$=\frac{c_Lc_R}{4}\left\{\left[R_{h,h}(0)+R_{v,v}(0)\right]^2-4R_{h,v}^2(\frac{1}{4f_c})+2\left[R_{v,v}(\tau)-R_{h,h}(\tau)+R_{h,v}(\tau+\frac{1}{4f_c})-R_{v,h}(\tau-\frac{1}{4f_c})\right]^2\right\}$$

$$=\frac{c_Lc_R}{4}G_v^2\left\{\left(T_{sys,v}+gT_{sys,h}\right)^2-gT_4^2\right\}$$

$$+\frac{c_Lc_R}{4}G_v^2\left\{\left(T_{sys,v}-gT_{sys,h}\right)^2+gT_3^2\right\}\mathrm{sinc}^2(B\tau)$$

$$+\frac{c_Lc_R}{4}G_v^2\left\{\left(T_{sys,v}-gT_{sys,h}\right)^2-gT_3^2\right\}\mathrm{sinc}^2(B\tau)\cos(4\pi f_c\tau)$$

$$-\frac{c_Lc_R}{4}G_v^2\sqrt{g}T_3\left(T_{sys,v}-gT_{sys,h}\right)\mathrm{sinc}^2(B\tau)\sin(4\pi f_c\tau)$$

(A2.5t)

$$
\begin{aligned}
R_{wR,wR}(\tau) &= \langle w_R(t) w_R(t-\tau) \rangle \\
&= \frac{c_R^2}{4} \left\langle \left[v_h(t) - v_v(t - \frac{1}{4f_c}) \right]^2 \cdot \left[v_h(t-\tau) - v_v(t-\tau - \frac{1}{4f_c}) \right]^2 \right\rangle \\
&= \frac{c_R^2}{4} \left\{ \left[R_{h,h}(0) + R_{v,v}(0) - 2R_{h,v}(\frac{1}{4f_c}) \right]^2 + 2 \left[R_{h,h}(\tau) + R_{v,v}(\tau) - R_{h,v}(\tau + \frac{1}{4f_c}) - R_{v,h}(\tau - \frac{1}{4f_c}) \right]^2 \right\} \\
&= \frac{c_R^2}{4} G_v^2 \left\{ T_{sys,v} + gT_{sys,h} - \sqrt{g} T_4 \right\}^2 \\
&\quad + \frac{c_R^2}{4} G_v^2 \left\{ T_{sys,v} + gT_{sys,h} - \sqrt{g} T_4 \right\}^2 \operatorname{sinc}^2(B\tau) \\
&\quad + \frac{c_R^2}{4} G_v^2 \left\{ T_{sys,v} + gT_{sys,h} - \sqrt{g} T_4 \right\} \operatorname{sinc}^2(B\tau) \cos(4\pi f_c \tau)
\end{aligned}
\tag{A2.5u}
$$

Spectra And Cross Spectra

The power spectra and cross spectra of the radiometer signals are found as Fourier transforms of their auto correlations and lag cross correlations. For signals $w_v(t)$, $w_P(t)$, $w_M(t)$, $w_h(t)$, $w_L(t)$ and $w_R(t)$, the power spectra and cross spectra are given by

$$
S_{wv,wv}(f) = c_v^2 G_v^2 T_{sys,v}^2 \delta(f) + c_v^2 G_v^2 T_{sys,v}^2 H(f) \tag{A2.6a}
$$

$$
\begin{aligned}
S_{wv,wP}(f) &= \frac{c_v c_P}{2} G_v^2 T_{sys,v} \left\{ T_{sys,v} + gT_{sys,h} + \sqrt{g} T_3 \right\} \delta(f) \\
&\quad + \frac{c_v c_P}{2} G_v^2 \left\{ \left[T_{sys,v} + \frac{\sqrt{g}}{2} T_3 \right]^2 + \frac{g}{4} T_4^2 \right\} H(f)
\end{aligned}
\tag{A2.6b}
$$

$$
\begin{aligned}
S_{wv,wM}(f) &= \frac{c_v c_M}{2} G_v^2 T_{sys,v} \left\{ T_{sys,v} + gT_{sys,h} - \sqrt{g} T_3 \right\} \delta(f) \\
&\quad + \frac{c_v c_M}{2} G_v^2 \left\{ \left(T_{sys,v} - \frac{\sqrt{g}}{2} T_3 \right)^2 + \frac{g}{4} T_4^2 \right\} H(f)
\end{aligned}
\tag{A2.6c}
$$

$$
S_{wv,wh}(f) = c_v c_h G_v^2 g T_{sys,v} T_{sys,h} \delta(f) + \frac{c_v c_h}{4} G_v^2 g \left\{ T_3^2 + T_4^2 \right\} H(f) \tag{A2.6d}
$$

$$S_{wv,wL}(f)=\frac{c_v c_L}{2}G_v^2 T_{sys,v}\left\{T_{sys,v}+gT_{sys,h}+\sqrt{g}T_4\right\}\delta(f)$$
$$+\frac{c_v c_L}{2}G_v^2\left\{\frac{g}{4}\left(T_3^2+T_4^2\right)+T_{sys,v}^2+\sqrt{g}T_{sys,v}T_4\right\}H(f) \quad \text{(A2.6e)}$$

$$S_{wv,wR}(f)=\frac{c_v c_R}{2}G_v^2 T_{sys,v}\left\{T_{sys,v}+gT_{sys,h}-\sqrt{g}T_4\right\}\delta(f)$$
$$+\frac{c_v c_R}{2}G_v^2\left\{\frac{g}{4}\left(T_3^2+T_4^2\right)+T_{sys,v}^2-\sqrt{g}T_{sys,v}T_4\right\}H(f) \quad \text{(A2.6f)}$$

$$S_{wP,wP}(f)=\frac{c_P^2}{4}G_v^2\left\{T_{sys,v}+gT_{sys,h}+\sqrt{g}T_3\right\}^2\delta(f)$$
$$+\frac{c_P^2}{4}G_v^2\left\{T_{sys,v}+gT_{sys,h}+\sqrt{g}T_3\right\}^2 H(f) \quad \text{(A2.6g)}$$

$$S_{wP,wM}(f)=\frac{c_P c_M}{4}G_v^2\left\{\left(T_{sys,v}+gT_{sys,h}\right)^2-gT_3^2\right\}\delta(f)$$
$$+\frac{c_P c_M}{4}G_v^2\left\{\left(T_{sys,v}-gT_{sys,h}\right)^2+gT_4^2\right\}H(f) \quad \text{(A2.6h)}$$

$$S_{wP,wh}(f)=\frac{c_P c_h}{2}G_v^2 gT_{sys,h}\left\{T_{sys,v}+gT_{sys,h}+\sqrt{g}T_3\right\}\delta(f)$$
$$+\frac{c_P c_h}{2}G_v^2\left\{\left[gT_{sys,h}+\frac{\sqrt{g}}{2}T_3\right]^2+\frac{g}{4}T_4^2\right\}H(f) \quad \text{(A2.6i)}$$

$$S_{wP,wL}(f)=\frac{c_P c_L}{4}G_v^2\left(T_{sys,v}+gT_{sys,h}+\sqrt{g}T_3\right)\left(T_{sys,v}+gT_{sys,h}+\sqrt{g}T_4\right)\delta(f)$$
$$+\frac{c_P c_L}{4}G_v^2\left\{\left[T_{sys,v}+\frac{\sqrt{g}}{2}\left(T_3+T_4\right)\right]^2+\left[gT_{sys,h}+\frac{\sqrt{g}}{2}\left(T_3+T_4\right)\right]^2\right\}H(f) \quad \text{(A2.6j)}$$

$$S_{wP,wR}(f)=\frac{c_P c_R}{4}G_v^2\left(T_{sys,v}+gT_{sys,h}+\sqrt{g}T_3\right)\cdot\left(T_{sys,v}+gT_{sys,h}-\sqrt{g}T_4\right)\delta(f)$$
$$+\frac{c_P c_R}{4}G_v^2\left\{\left[T_{sys,v}+\frac{\sqrt{g}}{2}\left(T_3-T_4\right)\right]^2+\left[gT_{sys,h}+\frac{\sqrt{g}}{2}\left(T_3-T_4\right)\right]^2\right\}H(f) \quad \text{(A2.6k)}$$

$$S_{wM,wM}(f)=\frac{c_M^2}{4}G_v^2\left\{T_{sys,v}+gT_{sys,h}-\sqrt{g}T_3\right\}^2\delta(f)$$
$$+\frac{c_M^2}{4}G_v^2\left\{T_{sys,v}+gT_{sys,h}-\sqrt{g}T_3\right\}^2 H(f) \quad \text{(A2.6l)}$$

$$S_{wM,wh}(f)=\frac{c_M c_h}{2}G_v^2 gT_{sys,h}\left\{T_{sys,v}+gT_{sys,h}-\sqrt{g}T_3\right\}\delta(f)$$
$$+\frac{c_M c_h}{2}G_v^2\left\{\left(gT_{sys,h}-\frac{\sqrt{g}}{2}T_3\right)^2+\frac{g}{4}T_4^2\right\}H(f) \quad \text{(A2.6m)}$$

$$S_{wM,wL}(f)=\frac{c_M c_L}{4}G_v^2\left(T_{sys,v}+gT_{sys,h}-\sqrt{g}T_3\right)\cdot\left(T_{sys,v}+gT_{sys,h}+\sqrt{g}T_4\right)\delta(f)$$
$$+\frac{c_M c_L}{4}G_v^2\left\{\left[T_{sys,v}-\frac{\sqrt{g}}{2}(T_3-T_4)\right]^2+\left[gT_{sys,h}-\frac{\sqrt{g}}{2}(T_3-T_4)\right]^2\right\}H(f) \quad \text{(A2.6n)}$$

$$S_{wM,wR}(f)=\frac{c_M c_R}{4}G_v^2\left(T_{sys,v}+gT_{sys,h}-\sqrt{g}T_3\right)\cdot\left(T_{sys,v}+gT_{sys,h}-\sqrt{g}T_4\right)\delta(f)$$
$$+\frac{c_M c_R}{4}G_v^2\left\{\left[gT_{sys,h}-\frac{\sqrt{g}}{2}(T_3+T_4)\right]^2+\left[T_{sys,v}-\frac{\sqrt{g}}{2}(T_3+T_4)\right]^2\right\}H(f) \quad \text{(A2.6o)}$$

$$S_{wh,wh}(f)=c_h^2G_v^2g^2T_{sys,h}^2\delta(f)+c_h^2G_v^2g^2T_{sys,h}^2H(f) \quad \text{(A2.6p)}$$

$$S_{wh,wL}(f)=\frac{c_h c_L}{2}G_v^2 gT_{sys,h}\left\{T_{sys,v}+gT_{sys,h}+\sqrt{g}T_4\right\}\delta(f)$$
$$+\frac{c_h c_L}{2}G_v^2\left\{g^2T_{sys,h}^2+\frac{1}{4}g\left(T_3^2+T_4^2\right)+\sqrt{g}T_4gT_{sys,h}\right\}H(f) \quad \text{(A2.6q)}$$

$$S_{wh,wR}(f)=\frac{c_h c_R}{2}G_v^2 gT_{sys,h}\left\{T_{sys,v}+gT_{sys,h}-\sqrt{g}T_4\right\}\delta(f)$$
$$+\frac{c_h c_R}{2}G_v^2\left\{g^2T_{sys,h}^2+\frac{1}{4}g\left(T_3^2+T_4^2\right)-\sqrt{g}T_4gT_{sys,h}\right\}H(f) \quad \text{(A2.6r)}$$

$$S_{wL,wL}(f)=\frac{c_L^2}{4}G_v^2\left(T_{sys,v}+gT_{sys,h}+\sqrt{g}T_4\right)^2\delta(f)+\frac{c_L^2}{4}G_v^2\left(T_{sys,v}+gT_{sys,h}+\sqrt{g}T_4\right)^2H(f) \quad \text{(A2.6s)}$$

$$S_{wL,wR}(f)=\frac{c_L c_R}{4}G_v^2\left\{\left(T_{sys,v}+gT_{sys,h}\right)^2-gT_4^2\right\}\delta(f)+\frac{c_L c_R}{4}G_v^2\left\{\left(T_{sys,v}-gT_{sys,h}\right)^2+gT_3^2\right\}H(f) \quad \text{(A2.6t)}$$

$$S_{wR,wR}(f)=\frac{c_R^2}{4}G_v^2\left\{T_{sys,v}+gT_{sys,h}-\sqrt{g}T_4\right\}^2\delta(f)+\frac{c_R^2}{4}G_v^2\left\{T_{sys,v}+gT_{sys,h}-\sqrt{g}T_4\right\}^2H(f) \quad \text{(A2.6u)}$$

where the Fourier transforms of the terms modulated by $\sin(4\pi f_c\tau)$ and $\cos(4\pi f_c\tau)$ in the expressions for auto correlation and lag cross correlation given in (A2.5) are not included

here because they will be removed by the subsequent low pass filters. In (A2.6), $g=G_h/G_v$ is the gain imbalance between *v*- and *h*-pol channels; $S_{wa,wa}(f)$ is the spectrum of $w_a(t)$ and $S_{wa,wb}(f)$ is the cross spectrum of $w_a(t)$ and $w_b(t)$. The "hat" function, *H(f)* in (A2.6), is given by

$$\begin{aligned} H(f) &= \frac{1}{B}\left(1-\left|\frac{f}{B}\right|\right) && for\,|f|<B \\ &= 0 && otherwise \end{aligned} \tag{A2.7}$$

The power spectra and cross spectra of signals $x_v(t)$, $x_P(t)$, $x_M(t)$, $x_h(t)$, $x_L(t)$ and $x_R(t)$ at the output of the low pass filters can be found from (A2.6) by

$$S_{a,b}(f) = S_{wa,wb}(f)\cdot|L(f)|^2 \tag{A2.8}$$

where *a* = *v*, *P, M, h*, *L* and *R* and where *L(f)* is the transfer function of the low pass filter, defined as zero for $|f| \geq \frac{1}{2\tau}$ and one otherwise, where τ is integration time,. Near DC, the hat function, *H(f)*, can be approximated by its value at *f=0*. The power spectra at $|f| < \frac{1}{2\tau}$ are given by

$$S_{v,v}(f) = c_v^2 G_v^2 T_{sys,v}^2 \delta(f) + \frac{c_v^2}{B} G_v^2 T_{sys,v}^2 \tag{A2.9a}$$

$$\begin{aligned} S_{v,P}(f) = {} & \frac{c_v c_P}{2} G_v^2 T_{sys,v} \left\{ T_{sys,v} + g T_{sys,h} + \sqrt{g} T_3 \right\} \delta(f) \\ & + \frac{c_v c_P}{2B} G_v^2 \left\{ \left(T_{sys,v} + \frac{\sqrt{g}}{2} T_3 \right)^2 + \frac{g}{4} T_4^2 \right\} \end{aligned} \tag{A2.9b}$$

$$S_{v,M}(f) = \frac{c_v c_M}{2} G_v^2 T_{sys,v} \left\{ T_{sys,v} + gT_{sys,h} - \sqrt{g} T_3 \right\} \delta(f) + \frac{c_v c_M}{2B} G_v^2 \left\{ \left(T_{sys,v} - \frac{\sqrt{g}}{2} T_3 \right)^2 + \frac{g}{4} T_4^2 \right\} \quad \text{(A2.9c)}$$

$$S_{v,h}(f) = c_v c_h G_v^2 g T_{sys,v} T_{sys,h} \delta(f) + \frac{c_v c_h}{4B} G_v^2 g \left\{ T_3^2 + T_4^2 \right\} \quad \text{(A2.9d)}$$

$$S_{v,L}(f) = \frac{c_v c_L}{2} G_v^2 T_{sys,v} \left\{ T_{sys,v} + gT_{sys,h} + \sqrt{g} T_4 \right\} \delta(f) + \frac{c_v c_L}{2B} G_v^2 \left\{ \frac{g}{4} \left(T_3^2 + T_4^2 \right) + T_{sys,v}^2 + \sqrt{g} T_{sys,v} T_4 \right\} \quad \text{(A2.9e)}$$

$$S_{v,R}(f) = \frac{c_v c_R}{2} G_v^2 T_{sys,v} \left\{ T_{sys,v} + gT_{sys,h} - \sqrt{g} T_4 \right\} \delta(f) + \frac{c_v c_R}{2B} G_v^2 \left\{ \frac{g}{4} \left(T_3^2 + T_4^2 \right) + T_{sys,v}^2 - \sqrt{g} T_{sys,v} T_4 \right\} \quad \text{(A2.9f)}$$

$$S_{P,P}(f) = \frac{c_P^2}{4} G_v^2 \left\{ T_{sys,v} + gT_{sys,h} + \sqrt{g} T_3 \right\}^2 \delta(f) + \frac{c_P^2}{4B} G_v^2 \left\{ T_{sys,v} + gT_{sys,h} + \sqrt{g} T_3 \right\}^2 \quad \text{(A2.9g)}$$

$$S_{P,M}(f) = \frac{c_P c_M}{4} G_v^2 \left\{ \left(T_{sys,v} + gT_{sys,h} \right)^2 - gT_3^2 \right\} \delta(f) + \frac{c_P c_M}{4B} G_v^2 \left\{ \left(T_{sys,v} - gT_{sys,h} \right)^2 + gT_4^2 \right\} \quad \text{(A2.9h)}$$

$$S_{P,h}(f) = \frac{c_P c_h}{2} G_v^2 g T_{sys,h} \left\{ T_{sys,v} + gT_{sys,h} + \sqrt{g} T_3 \right\} \delta(f) + \frac{c_P c_h}{2B} G_v^2 \left\{ \left(gT_{sys,h} + \frac{\sqrt{g}}{2} T_3 \right)^2 + \frac{g}{4} T_4^2 \right\} \quad \text{(A2.9i)}$$

$$S_{P,L}(f) = \frac{c_P c_L}{4} G_v^2 \left(T_{sys,v} + gT_{sys,h} + \sqrt{g}T_3\right)\left(T_{sys,v} + gT_{sys,h} + \sqrt{g}T_4\right)\delta(f) + \frac{c_P c_L}{4B} G_v^2 \left\{\left[T_{sys,v} + \frac{\sqrt{g}}{2}\left(T_3 + T_4\right)\right]^2 + \left[gT_{sys,h} + \frac{\sqrt{g}}{2}\left(T_3 + T_4\right)\right]^2\right\} \quad \text{(A2.9j)}$$

$$S_{P,R}(f) = \frac{c_P c_R}{4} G_v^2 \left(T_{sys,v} + gT_{sys,h} + \sqrt{g}T_3\right)\cdot\left(T_{sys,v} + gT_{sys,h} - \sqrt{g}T_4\right)\delta(f) + \frac{c_P c_R}{4B} G_v^2 \left\{\left[T_{sys,v} + \frac{\sqrt{g}}{2}\left(T_3 - T_4\right)\right]^2 + \left[gT_{sys,h} + \frac{\sqrt{g}}{2}\left(T_3 - T_4\right)\right]^2\right\} \quad \text{(A2.9k)}$$

$$S_{M,M}(f) = \frac{c_M^2}{4} G_v^2 \left\{T_{sys,v} + gT_{sys,h} - \sqrt{g}T_3\right\}^2 \delta(f) + \frac{c_M^2}{4B} G_v^2 \left\{T_{sys,v} + gT_{sys,h} - \sqrt{g}T_3\right\}^2 \quad \text{(A2.9l)}$$

$$S_{M,h}(f) = \frac{c_M c_h}{2} G_v^2 gT_{sys,h} \left\{T_{sys,v} + gT_{sys,h} - \sqrt{g}T_3\right\}\delta(f) + \frac{c_M c_h}{2B} G_v^2 \left\{\left[gT_{sys,h} - \frac{\sqrt{g}}{2}T_3\right]^2 + \frac{g}{4}T_4^2\right\} \quad \text{(A2.9m)}$$

$$S_{M,L}(f) = \frac{c_M c_L}{4} G_v^2 \left(T_{sys,v} + gT_{sys,h} - \sqrt{g}T_3\right)\cdot\left(T_{sys,v} + gT_{sys,h} + \sqrt{g}T_4\right)\delta(f) + \frac{c_M c_L}{4B} G_v^2 \left\{\left[T_{sys,v} - \frac{\sqrt{g}}{2}\left(T_3 - T_4\right)\right]^2 + \left[gT_{sys,h} - \frac{\sqrt{g}}{2}\left(T_3 - T_4\right)\right]^2\right\} \quad \text{(A2.9n)}$$

$$S_{M,R}(f) = \frac{c_M c_R}{4} G_v^2 \left(T_{sys,v} + gT_{sys,h} - \sqrt{g}T_3\right)\cdot\left(T_{sys,v} + gT_{sys,h} - \sqrt{g}T_4\right)\delta(f) + \frac{c_M c_R}{4B} G_v^2 \left\{\left[gT_{sys,h} - \frac{\sqrt{g}}{2}\left(T_3 + T_4\right)\right]^2 + \left[T_{sys,v} - \frac{\sqrt{g}}{2}\left(T_3 + T_4\right)\right]^2\right\} \quad \text{(A2.9o)}$$

$$S_{h,h}(f) = c_h^2 G_v^2 g^2 T_{sys,h}^2 \delta(f) + \frac{c_h^2}{B} G_v^2 g^2 T_{sys,h}^2 \quad \text{(A2.9p)}$$

$$S_{h,L}(f) = \frac{c_h c_L}{2} G_v^2 g T_{sys,h} \left\{ T_{sys,v} + g T_{sys,h} + \sqrt{g} T_4 \right\} \delta(f) + \frac{c_h c_L}{2B} G_v^2 \left\{ g^2 T_{sys,h}^2 + \frac{1}{4} g \left(T_3^2 + T_4^2 \right) + \sqrt{g} T_4 g T_{sys,h} \right\} \tag{A2.9q}$$

$$S_{h,R}(f) = \frac{c_h c_R}{2} G_v^2 g T_{sys,h} \left\{ T_{sys,v} + g T_{sys,h} - \sqrt{g} T_4 \right\} \delta(f) + \frac{c_h c_R}{2B} G_v^2 \left\{ g^2 T_{sys,h}^2 + \frac{1}{4} g \left(T_3^2 + T_4^2 \right) - \sqrt{g} T_4 g T_{sys,h} \right\} \tag{A2.9r}$$

$$S_{L,L}(f) = \frac{c_L^2}{4} G_v^2 \left(T_{sys,v} + g T_{sys,h} + \sqrt{g} T_4 \right)^2 \delta(f) + \frac{c_L^2}{4B} G_v^2 \left(T_{sys,v} + g T_{sys,h} + \sqrt{g} T_4 \right)^2 \tag{A2.9s}$$

$$S_{L,R}(f) = \frac{c_L c_R}{4} G_v^2 \left\{ \left(T_{sys,v} + g T_{sys,h} \right)^2 - g T_4^2 \right\} \delta(f) + \frac{c_L c_R}{4B} G_v^2 \left\{ \left(T_{sys,v} - g T_{sys,h} \right)^2 + g T_3^2 \right\} \tag{A2.9t}$$

$$S_{R,R}(f) = \frac{c_R^2}{4} G_v^2 \left\{ T_{sys,v} + g T_{sys,h} - \sqrt{g} T_4 \right\}^2 \delta(f) + \frac{c_R^2}{4B} G_v^2 \left\{ T_{sys,v} + g T_{sys,h} - \sqrt{g} T_4 \right\}^2 \tag{A2.9u}$$

In the above expressions, the terms on the right hand side that involve the Dirac delta function, $\delta(f)$, are the DC components of the spectrum. The others terms are the AC components.

The power contained in the DC and AC frequency components of $x_v(t)$, $x_P(t)$, $x_M(t)$, $x_h(t)$, $x_L(t)$ and $x_R(t)$ are obtained by integrating over the appropriate portions of their spectra. The expected values of these signals (*i.e.* the DC component of their spectra) are proportional to the four associated brightness temperatures. The variance of the signals (*i.e.* the integral over all AC components of the spectra) is due to the additive noise present in the measurements. The expected value (DC) and variance (AC) are given separately as

$$R_{v,v}^{DC}(0) = c_v^2 G_v^2 T_{sys,v}^2$$

$$\text{and } R_{v,v}^{AC}(0) = \frac{c_v^2}{B\tau} G_v^2 T_{sys,v}^2 \tag{A2.10a}$$

$$R_{v,P}^{DC}(0) = \frac{c_v c_P}{2} G_v^2 T_{sys,v} \left\{ T_{sys,v} + g T_{sys,h} + \sqrt{g} T_3 \right\}$$

$$\text{and } R_{v,P}^{AC}(0) = \frac{c_v c_P}{2B\tau} G_v^2 \left\{ \left(T_{sys,v} + \frac{\sqrt{g}}{2} T_3 \right)^2 + \frac{g}{4} T_4^2 \right\} \quad \text{(A2.10b)}$$

$$R_{v,M}^{DC}(0) = \frac{c_v c_M}{2} G_v^2 T_{sys,v} \left\{ T_{sys,v} + g T_{sys,h} - \sqrt{g} T_3 \right\}$$

$$\text{and } R_{v,M}^{AC}(0) = \frac{c_v c_M}{2B\tau} G_v^2 \left\{ \left(T_{sys,v} - \frac{\sqrt{g}}{2} T_3 \right)^2 + \frac{g}{4} T_4^2 \right\} \quad \text{(A2.10c)}$$

$$R_{v,h}^{DC}(0) = c_v c_h G_v^2 g T_{sys,v} T_{sys,h}$$

$$\text{and } R_{v,h}^{AC}(0) = \frac{c_v c_h}{4B\tau} G_v^2 g \left\{ T_3^2 + T_4^2 \right\} \quad \text{(A2.10d)}$$

$$R_{v,L}^{DC}(0) = \frac{c_v c_L}{2} G_v^2 T_{sys,v} \left\{ T_{sys,v} + g T_{sys,h} + \sqrt{g} T_4 \right\}$$

$$\text{and } R_{v,L}^{AC}(0) = \frac{c_v c_L}{2B\tau} G_v^2 \left\{ \frac{g}{4} \left(T_3^2 + T_4^2 \right) + T_{sys,v}^2 + \sqrt{g} T_{sys,v} T_4 \right\} \quad \text{(A2.10e)}$$

$$R_{v,R}^{DC}(0) = \frac{c_v c_R}{2} G_v^2 T_{sys,v} \left\{ T_{sys,v} + g T_{sys,h} - \sqrt{g} T_4 \right\}$$

$$\text{and } R_{v,R}^{AC}(0) = \frac{c_v c_R}{2B\tau} G_v^2 \left\{ \frac{g}{4} \left(T_3^2 + T_4^2 \right) + T_{sys,v}^2 - \sqrt{g} T_{sys,v} T_4 \right\} \quad \text{(A2.10f)}$$

$$R_{P,P}^{DC}(0) = \frac{c_P^2}{4} G_v^2 \left\{ T_{sys,v} + g T_{sys,h} + \sqrt{g} T_3 \right\}^2$$

$$\text{and } R_{P,P}^{AC}(0) = \frac{c_P^2}{4B\tau} G_v^2 \left\{ T_{sys,v} + g T_{sys,h} + \sqrt{g} T_3 \right\}^2 \quad \text{(A2.10g)}$$

$$R_{P,M}^{DC}(0) = \frac{c_P c_M}{4} G_v^2 \left\{ \left(T_{sys,v} + g T_{sys,h} \right)^2 - g T_3^2 \right\}$$

$$\text{and } R_{P,M}^{AC}(0) = \frac{c_P c_M}{4B\tau} G_v^2 \left\{ \left(T_{sys,v} - g T_{sys,h} \right)^2 + g T_4^2 \right\} \quad \text{(A2.10h)}$$

$$R_{P,h}^{DC}(0) = \frac{c_P c_h}{2} G_v^2 g T_{sys,h} \left\{ T_{sys,v} + g T_{sys,h} + \sqrt{g} T_3 \right\}$$

$$\text{and } R_{P,h}^{AC}(0) = \frac{c_P c_h}{2B\tau} G_v^2 \left\{ \left(g T_{sys,h} + \frac{\sqrt{g}}{2} T_3 \right)^2 + \frac{g}{4} T_4^2 \right\} \quad \text{(A2.10i)}$$

$$R_{P,L}^{DC}(0) = \frac{c_P c_L}{4} G_v^2 \left(T_{sys,v} + g T_{sys,h} + \sqrt{g} T_3 \right) \left(T_{sys,v} + g T_{sys,h} + \sqrt{g} T_4 \right)$$

$$\text{and } R_{P,L}^{AC}(0) = \frac{c_P c_L}{4B\tau} G_v^2 \left\{ \left[T_{sys,v} + \frac{\sqrt{g}}{2} \left(T_3 + T_4 \right) \right]^2 + \left[g T_{sys,h} + \frac{\sqrt{g}}{2} \left(T_3 + T_4 \right) \right]^2 \right\} \quad \text{(A2.10j)}$$

$$R_{P,R}^{DC}(0) = \frac{c_P c_R}{4} G_v^2 \left(T_{sys,v} + g T_{sys,h} + \sqrt{g} T_3 \right) \cdot \left(T_{sys,v} + g T_{sys,h} - \sqrt{g} T_4 \right)$$

$$\text{and } R_{P,R}^{AC}(0) = \frac{c_P c_R}{4B\tau} G_v^2 \left\{ \left[T_{sys,v} + \frac{\sqrt{g}}{2} \left(T_3 - T_4 \right) \right]^2 + \left[g T_{sys,h} + \frac{\sqrt{g}}{2} \left(T_3 - T_4 \right) \right]^2 \right\} \quad \text{(A2.10k)}$$

$$R_{M,M}^{DC}(0) = \frac{c_M^2}{4} G_v^2 \left\{ T_{sys,v} + g T_{sys,h} - \sqrt{g} T_3 \right\}^2$$

$$\text{and } R_{M,M}^{AC}(0) = \frac{c_M^2}{4B\tau} G_v^2 \left\{ T_{sys,v} + g T_{sys,h} - \sqrt{g} T_3 \right\}^2 \quad \text{(A2.10l)}$$

$$R_{M,h}^{DC}(0) = \frac{c_M c_h}{2} G_v^2 g T_{sys,h} \left\{ T_{sys,v} + g T_{sys,h} - \sqrt{g} T_3 \right\}$$

$$\text{and } R_{M,h}^{AC}(0) = \frac{c_M c_h}{2B\tau} G_v^2 \left\{ \left(g T_{sys,h} - \frac{\sqrt{g}}{2} T_3 \right)^2 + \frac{g}{4} T_4^2 \right\} \quad \text{(A2.10m)}$$

$$R_{M,L}^{DC}(0) = \frac{c_M c_L}{4} G_v^2 \left(T_{sys,v} + g T_{sys,h} - \sqrt{g} T_3 \right) \cdot \left(T_{sys,v} + g T_{sys,h} + \sqrt{g} T_4 \right)$$

and $R_{M,L}^{AC}(0) = \frac{c_M c_L}{4B\tau} G_v^2 \left\{ \left[T_{sys,v} - \frac{\sqrt{g}}{2}\left(T_3 - T_4\right) \right]^2 + \left[gT_{sys,h} - \frac{\sqrt{g}}{2}\left(T_3 - T_4\right) \right]^2 \right\}$ (A2.10n)

$$R_{M,R}^{DC}(0) = \frac{c_M c_R}{4} G_v^2 \left(T_{sys,v} + gT_{sys,h} - \sqrt{g}T_3\right) \cdot \left(T_{sys,v} + gT_{sys,h} - \sqrt{g}T_4\right)$$

and $R_{M,R}^{AC}(0) = \frac{c_M c_R}{4B\tau} G_v^2 \left\{ \left[gT_{sys,h} - \frac{\sqrt{g}}{2}\left(T_3 + T_4\right) \right]^2 + \left[T_{sys,v} - \frac{\sqrt{g}}{2}\left(T_3 + T_4\right) \right]^2 \right\}$ (A2.10o)

$$R_{h,h}^{DC}(0) = c_h^2 G_v^2 g^2 T_{sys,h}^2$$

and $R_{h,h}^{AC}(0) = \frac{c_h^2}{B\tau} G_v^2 g^2 T_{sys,h}^2$ (A2.10p)

$$R_{h,L}^{DC}(0) = \frac{c_h c_L}{2} G_v^2 g T_{sys,h} \left\{ T_{sys,v} + gT_{sys,h} + \sqrt{g}T_4 \right\}$$

and $R_{h,L}^{AC}(0) = \frac{c_h c_L}{2B\tau} G_v^2 \left\{ g^2 T_{sys,h}^2 + \frac{1}{4} g\left(T_3^2 + T_4^2\right) + \sqrt{g} T_4 g T_{sys,h} \right\}$ (A2.10q)

$$R_{h,R}^{DC}(0) = \frac{c_h c_R}{2} G_v^2 g T_{sys,h} \left\{ T_{sys,v} + gT_{sys,h} - \sqrt{g}T_4 \right\}$$

and $R_{h,R}^{AC}(0) = \frac{c_h c_R}{2B\tau} G_v^2 \left\{ g^2 T_{sys,h}^2 + \frac{1}{4} g\left(T_3^2 + T_4^2\right) - \sqrt{g} T_4 g T_{sys,h} \right\}$ (A2.10r)

$$R_{L,L}^{DC}(0) = \frac{c_L^2}{4} G_v^2 \left(T_{sys,v} + gT_{sys,h} + \sqrt{g}T_4\right)^2$$

and $R_{L,L}^{AC}(0) = \frac{c_L^2}{4B\tau} G_v^2 \left(T_{sys,v} + gT_{sys,h} + \sqrt{g}T_4\right)^2$ (A2.10s)

$$R_{L,R}^{DC}(0) = \frac{c_L c_R}{4} G_v^2 \left\{ \left(T_{sys,v} + gT_{sys,h}\right)^2 - gT_4^2 \right\}$$

and $R_{L,R}^{AC}(0) = \frac{c_L c_R}{4B\tau} G_v^2 \left\{ \left(T_{sys,v} - gT_{sys,h}\right)^2 + gT_3^2 \right\}$ (A2.10t)

$$R_{R,R}^{DC}(0) = \frac{c_R^2}{4} G_v^2 \left\{ T_{sys,v} + gT_{sys,h} - \sqrt{g}T_4 \right\}^2$$

$$\text{and} \quad R_{R,R}^{AC}(0) = \frac{c_R^2}{4B\tau} G_v^2 \left\{ T_{sys,v} + gT_{sys,h} - \sqrt{g}T_4 \right\}^2 \tag{A2.10u}$$

where $R_{X,Y}^{DC}(0) = \langle X(t) \rangle \cdot \langle Y(t) \rangle$ and $R_{X,Y}^{AC}(0)$ denotes the variance of *X(t)* if *X(t)=Y(t)* or the covariance of X(t) and Y(t) if *X(t)≠Y(t)*.

Appendix 3

Covariance of Correlating Polarimetric Radiometer Signals

The signals $v_v(t)-v_6(t)$, $n_v(t)$, $n_h(t)$, $b_v(t)$ and $b_h(t)$ and their statistical properties are identical to those associated with Appendix 2. The signals in the cross-correlating channels of the radiometer, prior to low pass filtering, are given by

$$w_3(t) = v_v(t) \cdot v_h(t) \tag{A3.1a}$$

$$w_4(t) = v_v(t - \frac{1}{4f_c}) \cdot v_h(t) \tag{A3.1b}$$

After the low pass filter, the correlating channel signals become $x_3(t)$ and $x_4(t)$ respectively.

The procedure followed to derive the covariance relationships between the three low pass filtered signals is similar to that for the hybrid combining radiometer, as described in Appendix 2. The auto correlations and lag cross correlations between signals $w_v(t)$, $w_3(t)$, $w_4(t)$ and $w_h(t)$ can be expanded as

$$\begin{aligned} R_{wv,wv}(\tau) &= \langle w_v(t) w_v(t-\tau) \rangle \\ &= \langle v_v^2(t) v_v^2(t-\tau) \rangle \\ &= R_{v,v}^2(0) + 2R_{v,v}^2(\tau) \\ &= G_v^2 T_{sys,v}^2 + G_v^2 T_{sys,v}^2 \text{sinc}^2(B\tau)\{1 + \cos(4\pi f_c \tau)\} \end{aligned} \tag{A3.2a}$$

$$
\begin{aligned}
R_{wv,w3}(\tau) &= R_{w3,wv}(-\tau) = \langle w_v(t) w_3(t-\tau) \rangle \\
&= \langle v_v^2(t) v_v(t-\tau) \cdot v_h(t-\tau) \rangle \\
&= R_{v,v}(0) R_{v,h}(0) + 2 R_{v,v}(\tau) R_{v,h}(\tau) \\
&= \frac{\sqrt{g}}{2} G_v^2 T_{sys,v} T_3 + \frac{\sqrt{g}}{2} G_v^2 T_{sys,v} T_3 \mathrm{sinc}^2(B\tau) \\
&\quad + \frac{\sqrt{g}}{2} G_v^2 T_{sys,v} \mathrm{sinc}^2(B\tau) \{ T_3 \cos(4\pi f_c \tau) - T_4 \sin(4\pi f_c \tau) \}
\end{aligned}
\tag{A3.2b}
$$

$$
\begin{aligned}
R_{wv,w4}(\tau) &= R_{w4,wv}(-\tau) = \langle w_v(t) w_4(t-\tau) \rangle \\
&= \left\langle v_v^2(t) v_v(t-\tau-\frac{1}{4f_c}) \cdot v_h(t-\tau) \right\rangle \\
&= R_{v,v}(0) R_{v,h}(-\frac{1}{4f_c}) + 2 R_{v,v}(\tau+\frac{1}{4f_c}) R_{v,h}(\tau) \\
&= \frac{G_v \sqrt{G_v G_h}}{2} T_{sys,v} T_4 + \frac{G_v \sqrt{G_v G_h}}{2} T_{sys,v} T_4 \mathrm{sinc}^2(B\tau) \\
&\quad - G_v \sqrt{G_v G_h} T_{sys,v} \left\{ \frac{T_3}{2} \sin(4\pi f_c \tau) + \frac{T_4}{2} \cos(4\pi f_c \tau) \right\} \mathrm{sinc}^2(B\tau)
\end{aligned}
\tag{A3.2c}
$$

$$
\begin{aligned}
R_{wv,wh}(\tau) &= R_{wh,wv}(-\tau) = \langle w_v(t) w_h(t-\tau) \rangle \\
&= \langle v_v^2(t) v_h^2(t-\tau) \rangle \\
&= R_{v,v}(0) R_{h,h}(0) + 2 R_{v,h}^2(\tau) \\
&= g G_v^2 T_{sys,v} T_{sys,h} + \frac{g}{4} G_v^2 \{ T_3^2 + T_4^2 \} \mathrm{sinc}^2(B\tau) \\
&\quad + \frac{g}{4} G_v^2 \mathrm{sinc}^2(B\tau) \{ (T_3^2 - T_4^2) \cos(4\pi f_c \tau) - 2 T_3 T_4 \sin(4\pi f_c \tau) \}
\end{aligned}
\tag{A3.2d}
$$

$$
\begin{aligned}
R_{w3,w3}(\tau) &= \langle w_3(t) w_3(t-\tau) \rangle = \langle v_v(t) \cdot v_h(t) v_v(t-\tau) \cdot v_h(t-\tau) \rangle \\
&= R_{v,h}^2(0) + R_{v,v}(\tau) R_{h,h}(\tau) + R_{v,h}(\tau) R_{h,v}(\tau) \\
&= \frac{g}{4} G_v^2 T_3^2 + 0.5 g G_v^2 T_{sys,v} T_{sys,h} \mathrm{sinc}^2(B\tau) \{ 1 + \cos(4\pi f_c \tau) \} \\
&\quad + \frac{g}{8} G_v^2 \mathrm{sinc}^2(B\tau) \{ T_3^2 - T_4^2 + (T_3^2 + T_4^2) \cos(4\pi f_c \tau) \}
\end{aligned}
\tag{A3.2e}
$$

$$
\begin{aligned}
R_{w3,w4}(\tau) &= \langle w_3(t)w_4(t-\tau)\rangle \\
&= \left\langle v_v(t)\cdot v_h(t)v_v(t-\tau-\frac{1}{4f_c})\cdot v_h(t-\tau)\right\rangle \\
&= R_{v,h}(0)R_{v,h}(-\frac{1}{4f_c}) + R_{v,v}(\tau+\frac{1}{4f_c})R_{h,h}(\tau) + R_{v,h}(\tau)R_{h,v}(\tau+\frac{1}{4f_c}) \qquad \text{(A3.2f)} \\
&= \frac{G_vG_h}{4}T_3T_4 + \frac{G_vG_h}{4}T_3T_4\mathrm{sinc}^2(B\tau) \\
&\quad -\frac{G_vG_h}{4}\left\{2T_{sys,v}T_{sys,h} + \frac{T_3^2+T_4^2}{2}\right\}\sin(4\pi f_c\tau)\mathrm{sinc}^2(B\tau)
\end{aligned}
$$

$$
\begin{aligned}
R_{w3,wh}(\tau) = R_{wh,w3}(-\tau) &= \langle w_3(t)w_h(t-\tau)\rangle = \left\langle v_v(t)\cdot v_h(t)v_h^2(t-\tau)\right\rangle \\
&= R_{v,h}(0)R_{h,h}(0) + 2R_{v,h}(\tau)R_{h,h}(\tau) \\
&= \frac{\sqrt{g^3}}{2}G_v^2T_{sys,h}T_3 \qquad \text{(A3.2g)} \\
&\quad + \frac{\sqrt{g^3}}{2}G_v^2T_{sys,h}\mathrm{sinc}^2(B\tau)\{T_3 + T_3\cos(4\pi f_c\tau) - T_4\sin(4\pi f_c\tau)\}
\end{aligned}
$$

$$
\begin{aligned}
R_{w4,w4}(\tau) &= \langle w_4(t)w_4(t-\tau)\rangle \\
&= \left\langle v_v(t-\frac{1}{4f_c})\cdot v_h(t)v_v(t-\tau-\frac{1}{4f_c})\cdot v_h(t-\tau)\right\rangle \\
&= R_{v,h}^2(-\frac{1}{4f_c}) + R_{v,v}(\tau)R_{h,h}(\tau) + R_{v,h}(\tau-\frac{1}{4f_c})R_{h,v}(\tau+\frac{1}{4f_c}) \qquad \text{(A3.2h)} \\
&= \frac{G_vG_h}{4}T_4^2 + \frac{G_vG_h}{4}\left\{2T_{sys,v}T_{sys,h} + \frac{T_4^2-T_3^2}{2}\right\}\mathrm{sinc}^2(B\tau) \\
&\quad + \frac{G_vG_h}{4}\left\{2T_{sys,v}T_{sys,h} + \frac{T_3^2+T_4^2}{2}\right\}\mathrm{sinc}^2(B\tau)\cos(4\pi f_c\tau)
\end{aligned}
$$

$$
\begin{aligned}
R_{w4,wh}(\tau) = R_{wh,w4}(-\tau) &= \langle w_4(t)w_h(t-\tau)\rangle \\
&= \left\langle v_v(t-\frac{1}{4f_c})\cdot v_h(t)v_h^2(t-\tau)\right\rangle \\
&= R_{v,h}(-\frac{1}{4f_c})R_{h,h}(0) + 2R_{v,h}(\tau-\frac{1}{4f_c})R_{h,h}(\tau) \qquad \text{(A3.2i)} \\
&= \frac{\sqrt{G_vG_h}G_h}{2}T_{sys,h}T_4 + \frac{\sqrt{G_vG_h}G_h}{2}T_{sys,h}T_4\mathrm{sinc}^2(B\tau) \\
&\quad + \frac{\sqrt{G_vG_h}G_h}{2}T_{sys,h}\{T_3\sin(4\pi f_c\tau) + T_4\cos(4\pi f_c\tau)\}\mathrm{sinc}^2(B\tau)
\end{aligned}
$$

$$R_{wh,wh}(\tau) = \langle w_h(t)w_h(t-\tau)\rangle = \langle v_h^2(t)v_h^2(t-\tau)\rangle$$
$$= R_{h,h}^2(0) + 2R_{h,h}^2(\tau) \tag{A3.2j}$$
$$= g^2G_v^2T_{sys,h}^2 + g^2G_v^2T_{sys,h}^2\mathrm{sinc}^2(B\tau)\{1+\cos(4\pi f_c\tau)\}$$

The power spectra and cross spectra of the radiometer signals are the Fourier transforms of their auto correlations and lag cross correlations, respectively. For signals $w_v(t)$, $w_3(t)$, $w_4(t)$ and $w_h(t)$, the power spectra and cross spectra are given by

$$S_{wv,wv}(f) = G_v^2T_{sys,v}^2\delta(f) + G_v^2T_{sys,v}^2H(f) \tag{A3.3a}$$

$$S_{wv,w3}(f) = \frac{\sqrt{g}}{2}G_v^2T_{sys,v}T_3\delta(f) + \frac{\sqrt{g}}{2}G_v^2T_{sys,v}T_3H(f) \tag{A3.3b}$$

$$S_{wv,w4}(f) = \frac{G_v\sqrt{G_vG_h}}{2}T_{sys,v}T_4\delta(f) + \frac{G_v\sqrt{G_vG_h}}{2}T_{sys,v}T_4H(f) \tag{A3.3c}$$

$$S_{wv,wh}(f) = gG_v^2T_{sys,v}T_{sys,h}\delta(f) + \frac{g}{4}G_v^2\{T_3^2+T_4^2\}H(f) \tag{A3.3d}$$

$$S_{w3,w3}(f) = \frac{g}{4}G_v^2T_3^2\delta(f) + \frac{g}{2}G_v^2T_{sys,v}T_{sys,h}H(f) + \frac{g}{8}G_v^2\{T_3^2-T_4^2\}H(f) \tag{A3.3e}$$

$$S_{w3,w4}(f) = \frac{G_vG_h}{4}T_3T_4\delta(f) + \frac{G_vG_h}{4}T_3T_4H(f) \tag{A3.3f}$$

$$S_{w3,wh}(f) = \frac{\sqrt{g^3}}{2}G_v^2T_{sys,h}T_3\delta(f) + \frac{\sqrt{g^3}}{2}G_v^2T_{sys,h}T_3H(f) \tag{A3.3g}$$

$$S_{w4,w4}(f) = \frac{G_vG_h}{4}T_4^2\delta(f) + \frac{G_vG_h}{4}\left\{2T_{sys,v}T_{sys,h} + \frac{T_4^2-T_3^2}{2}\right\}H(f) \tag{A3.3h}$$

$$S_{w4,wh}(f) = \frac{\sqrt{G_vG_h}G_h}{2}T_{sys,h}T_4\delta(f) + \frac{\sqrt{G_vG_h}G_h}{2}T_{sys,h}T_4H(f) \tag{A3.3i}$$

$$S_{wh,wh}(f) = g^2G_v^2T_{sys,h}^2\delta(f) + g^2G_v^2T_{sys,h}^2H(f) \tag{A3.3f}$$

where the Fourier transform of the terms modulated by either $\cos(4\pi f_c \tau)$ or $\sin(4\pi f_c \tau)$ in the expressions for auto correlations and lag cross correlations in (A3.3) are not included here because they will be filtered out by the subsequent low pass filters. In (A3.3), $g=G_h/G_v$ is the gain imbalance between *v*-pol and *h*-pol channels; $S_{wa,wa}(f)$ is the spectrum of $w_a(t)$, and $S_{wa,wb}(f)$ is the cross-spectrum of $w_a(t)$ and $w_b(t)$. The "hat" function, *H(f)* in (A3.3), is given by

$$\begin{aligned} H(f) &= \frac{1}{B}\left(1-\left|\frac{f}{B}\right|\right) \qquad & for\,|f|\langle B \\ &= 0 \qquad & otherwise \end{aligned} \tag{A3.4}$$

The power spectra and cross spectra of the signals $x_v(t)$, $x_h(t)$ and $x_3(t)$ at the output of the low pass filters can be founded from (A3.3) by

$$S_{a,b}(f) = S_{wa,wb}(f)\cdot|L(f)|^2 \tag{A3.5}$$

where *a* = *v*, *h*, and *3* and where *L(f)* is the transfer function of the low pass filter, defined as zero for $|f| \geq \frac{1}{2\tau}$ and one otherwise, where τ is integration time,. Near DC, the hat function, *H(f)*, can be approximated by its value at *f=0*. The power spectra at $|f| < \frac{1}{2\tau}$ are given by

$$S_{v,v}(f) = G_v^2 T_{sys,v}^2 \delta(f) + \frac{1}{B} G_v^2 T_{sys,v}^2 \tag{A3.6a}$$

$$S_{v,3}(f) = \frac{\sqrt{g}}{2} G_v^2 T_{sys,v} T_3 \delta(f) + \frac{\sqrt{g}}{2B} G_v^2 T_{sys,v} T_3 \tag{A3.6b}$$

$$S_{v,4}(f) = \frac{\sqrt{g}}{2} G_v^2 T_{sys,v} T_4 \delta(f) + \frac{\sqrt{g}}{2B} G_v^2 T_{sys,v} T_4 \tag{A3.6c}$$

$$S_{v,h}(f) = g G_v^2 T_{sys,v} T_{sys,h} \delta(f) + \frac{g}{4B} G_v^2 \left\{ T_3^2 + T_4^2 \right\} \tag{A3.6d}$$

$$S_{3,3}(f) = \frac{g}{4} G_v^2 T_3^2 \delta(f) + \frac{g}{2B} G_v^2 T_{sys,v} T_{sys,h} + \frac{g}{8B} G_v^2 \left\{ T_3^2 - T_4^2 \right\} \tag{A3.6e}$$

$$S_{3,4}(f) = \frac{g}{4} G_v^2 T_3 T_4 \delta(f) + \frac{g}{4B} G_v^2 T_3 T_4 \tag{A3.6f}$$

$$S_{3,h}(f) = \frac{\sqrt{g^3}}{2} G_v^2 T_{sys,h} T_3 \delta(f) + \frac{\sqrt{g^3}}{2B} G_v^2 T_{sys,h} T_3 \tag{A3.6g}$$

$$S_{4,4}(f) = \frac{g}{4} G_v^2 T_4^2 \delta(f) + \frac{g}{4B} G_v^2 \left\{ 2 T_{sys,v} T_{sys,h} + \frac{T_4^2 - T_3^2}{2} \right\} \tag{A3.6h}$$

$$S_{4,h}(f) = \frac{\sqrt{g^3}}{2} G_v^2 T_{sys,h} T_4 \delta(f) + \frac{\sqrt{g^3}}{2B} G_v^2 T_{sys,h} T_4 \tag{A3.6i}$$

$$S_{h,h}(f) = g^2 G_v^2 T_{sys,h}^2 \delta(f) + \frac{g^2}{B} G_v^2 T_{sys,h}^2 \tag{A3.6j}$$

In the above expressions, the terms on the right hand side that involve the Dirac delta funcgtion, $\delta(f)$, are the DC components of the spectra. The others are the AC components.

The power contained in the DC and AC frequency components of $x_v(t)$, $x_3(t)$, $x_4(t)$ and $x_h(t)$ are obtained by integrating over the appropriate portions of their spectra. The expected value of these signals (*i.e.* the DC component of their spectra) is proportional to the four associated brightness temperatures. The variance of the signals (*i.e.* the integral over the AC component of their spectra) is due to the additive noise

present in the measurements. The expected value (DC) and variance (AC) are given separately as

$$R_{v,v}^{DC}(0) = G_v^2 T_{sys,v}^2$$

$$\text{and} \qquad R_{v,v}^{AC}(0) = \frac{1}{B\tau} G_v^2 T_{sys,v}^2 \tag{A3.7a}$$

$$R_{v,3}^{DC}(0) = \frac{\sqrt{g}}{2} G_v^2 T_{sys,v} T_3$$

$$\text{and} \qquad R_{v,3}^{AC}(0) = \frac{\sqrt{g}}{2B\tau} G_v^2 T_{sys,v} T_3 \tag{A3.7b}$$

$$R_{v,4}^{DC}(0) = \frac{\sqrt{g}}{2} G_v^2 T_{sys,v} T_4$$

$$\text{and} \qquad R_{v,4}^{AC}(0) = \frac{\sqrt{g}}{2B\tau} G_v^2 T_{sys,v} T_4 \tag{A3.7c}$$

$$R_{v,h}^{DC}(0) = g G_v^2 T_{sys,v} T_{sys,h}$$

$$\text{and} \qquad R_{v,h}^{AC}(0) = \frac{g}{4B\tau} G_v^2 \left\{ T_3^2 + T_4^2 \right\} \tag{A3.7d}$$

$$R_{3,3}^{DC}(0) = \frac{g}{4} G_v^2 T_3^2$$

$$\text{and} \qquad R_{3,3}^{AC}(0) = \frac{g}{4B\tau} G_v^2 \left\{ 2T_{sys,v} T_{sys,h} + \frac{T_3^2 - T_4^2}{2} \right\} \tag{A3.7e}$$

$$R_{3,4}^{DC}(0) = \frac{g}{4} G_v^2 T_3 T_4$$

$$\text{and} \qquad R_{3,4}^{AC}(0) = \frac{g}{4B\tau} G_v^2 T_3 T_4 \tag{A3.7f}$$

$$R_{3,h}^{DC}(0) = \frac{\sqrt{g^3}}{2} G_v^2 T_{sys,h} T_3$$

and $$R_{3,h}^{AC}(0) = \frac{\sqrt{g^3}}{2B\tau} G_v^2 T_{sys,h} T_3 \tag{A3.7g}$$

$$R_{4,4}^{DC}(0) = \frac{g}{4} G_v^2 T_4^2$$

and $$R_{4,4}^{AC}(0) = \frac{g}{4B\tau} G_v^2 \left\{ 2T_{sys,v} T_{sys,h} + \frac{T_4^2 - T_3^2}{2} \right\} \tag{A3.7h}$$

$$R_{4,h}^{DC}(0) = \frac{\sqrt{g^3}}{2} G_v^2 T_{sys,h} T_4$$

and $$R_{4,h}^{AC}(0) = \frac{\sqrt{g^3}}{2B\tau} G_v^2 T_{sys,h} T_4 \tag{A3.7i}$$

$$R_{h,h}^{DC}(0) = g^2 G_v^2 T_{sys,h}^2$$

and $$R_{h,h}^{AC}(0) = \frac{1}{B\tau} g^2 G_v^2 T_{sys,h}^2 \tag{A3.7j}$$

Appendix 4

Correction for Impedance Mismatches at the Radiometer Input Port

A model for impedance mismatches between a radiometer receiver and its antenna has been developed by Corbella *et al*. [57-59]. Their approach is adopted here. The brightness temperature of the CNCS active cold load is determined by a two-point calibration using an ambient temperature coaxial termination and one immersed in LN_2. The digital counts measured by the RUT while connected to each of the LN_2 reference load, ambient reference load, and CNCS active cold load are, respectively, given by

$$C_{LN2} = g\left\{\left|\Lambda_{LN2}\right|^2 T_{LN2} + \left|\Lambda_{LN2}\right|^2 \left|\Gamma_{LN2}\right|^2 T_r + 2\,\mathrm{Re}\left[\Lambda_{LN2}\Gamma_{LN2}T_c\right] + T_R\right\} \quad \text{(A4.1a)}$$

$$C_{ref} = g\left\{\left|\Lambda_{CNCS}\right|^2 T_{ref} + \left|\Lambda_{CNCS}\right|^2 \left|\Gamma_{CNCS}\right|^2 T_r + 2\,\mathrm{Re}\left[\Lambda_{CNCS}\Gamma_{CNCS}T_c\right] + T_R\right\} \quad \text{(A4.1b)}$$

$$C_{Cold} = g\left\{\left|\Lambda_{CNCS}\right|^2 T_{Cold} + \left|\Lambda_{CNCS}\right|^2 \left|\Gamma_{CNCS}\right|^2 T_r + 2\,\mathrm{Re}\left[\Lambda_{CNCS}\Gamma_{CNCS}T_c\right] + T_R\right\} \quad \text{(A4.1c)}$$

where g is the radiometer gain, T_{LN2}, T_{ref} and T_{Cold} are the brightness temperatures of the LN_2 reference load, ambient reference load, and CNCS active cold load that would be measued by a radiometer with a perfect impedance match, Γ_{LN2} and Γ_{CNCS} are the voltage reflection coefficients when viewing the LN_2 reference load and the CNCS active cold load, and $\Lambda_y = (1 - S_{11,rad}\Gamma_y)^{-1}$ (for $y = LN2$ and $CNCS$), where $S_{11,rad}$ is the input reflection coefficient of the radiometer receiver. In (A4.1), T_r is the noise temperature

exiting the receiver toward the antenna, T_R is the traditional receiver noise temperature, and T_c is the component of T_r and T_R that is correlated. For cases of high isolation at the radiometer input port, T_c is given by [58]

$$T_c = -T_{phy}\left(S_{11,FE} + \frac{S_{12,FE}S^*_{22,FE}}{S^*_{21,FE}}\right) \tag{A4.2}$$

where T_{phy} is the physical temperature of the radiometer front end components preceding the first gain stage and $S_{xy,FE}$ for x,y=1,2 are the S-parameters for the radiometer front end **(**see [57-59] for detailed definitions of these noise temperatures**)**. Port 1 for these S-parameters is the input to the radiometer and port 2 is the output from the first gain stage of the receiver (*i.e.* the point after which internally generated noise ceases to have a significant effect on the overall receiver noise temperature). The fact that the radiometer includes an isolator at its input port with a good (~25 dB) level of isolation insures that T_r is approximately equal to T_{phy}.

All of the reflection coefficients and other *S*-parameters in (A1)-(A3) can be measured directly using a network analyzer. The warm and cold reference brightness temperatures, T_{ref} and T_{LN2}, are also known. The remaining 3 unknown variables (g, T_R and T_{Cold}), can be solved algebraically from the three simultaneous equations (A4.1). The value for T_{Cold} determined in this way is the brightness temperature that would be presented by the CNCS active cold load to a radiometer with a perfect impedance match. For the L-Band CNCS, T_{Cold} is found to be approximately 2 K different than its value would have been had the effects of impedance mismatches been ignored.

The effect on the measured Stokes parameters in brightness temperature of impedance mismatches between a radiometer's antenna and its receiver, and of cross-talk

between the orthogonal polarimetric channels of a radiometer's antenna, has also been considered previously by Corbella *et al*. [58]. Their approach is again adopted here, replacing the antenna by the CNCS and using the impedance mismatch and isolation characteristics of the CNCS. The modified Stokes parameters are related to the true values by

$$\begin{bmatrix} T_v' \\ T_h' \\ T_3' \\ T_4' \end{bmatrix} = \begin{bmatrix} 1 & 0 & 0 & 0 & T_{ex,v} \\ 0 & 1 & 0 & 0 & T_{ex,h} \\ 2\,\mathrm{Re}\left\{S_{hv}^* S_{11,rad,v}^*\right\} & 2\,\mathrm{Re}\left\{S_{vh} S_{11,rad,h}\right\} & 1 & 0 & T_{ex,3} \\ 2\,\mathrm{Im}\left\{S_{hv}^* S_{11,rad,v}^*\right\} & 2\,\mathrm{Im}\left\{S_{vh} S_{11,rad,h}\right\} & 0 & 1 & T_{ex,4} \end{bmatrix} \cdot \begin{bmatrix} T_v \\ T_h \\ T_3 \\ T_4 \\ 1 \end{bmatrix} \tag{A4.3}$$

where T_y' are the modified brightness temperatures and T_y are the values that would have been measured if the impedance match was perfect and there was no polarization cross-talk ($y = v$, h, *3* and *4*), S_{xy} (x,y=v,h) are the S-parameters of the CNCS, $S_{11,rad,x}$ (x=v,h) is the reflection coefficient at the input ports of the RUT, and the subscripts v and h denote the vertically and horizontally polarized channels of the CNCS and RUT. The offset brightness temperatures, $T_{ex,y}$ ($y = v$, h, *3* and *4*) are defined by

$$T_{ex,v} = \left|S_{vv}\right|^2 T_{r,v} + \left|S_{vh}\right|^2 T_{r,h} + 2\,\mathrm{Re}\left\{S_{vv} T_{c,v}\right\} \tag{A4.4a}$$

$$T_{ex,h} = \left|S_{hh}\right|^2 T_{r,h} + \left|S_{hv}\right|^2 T_{r,v} + 2\,\mathrm{Re}\left\{S_{hh} T_{c,h}\right\} \tag{A4.4b}$$

$$T_{ex,3} = 2\,\mathrm{Re}\left\{S_{vv} S_{hv}^* T_{r,v} + S_{vh} S_{hh}^* T_{r,h} + S_{hv}^* T_{c,v}^* + S_{vh} T_{c,h}\right\} \tag{A4.4c}$$

$$T_{ex,4} = 2\,\mathrm{Im}\left\{S_{vv} S_{hv}^* T_{r,v} + S_{vh} S_{hh}^* T_{r,h} + S_{hv}^* T_{c,v}^* + S_{vh} T_{c,h}\right\} \tag{A4.4d}$$

See [58] for detailed descriptions of these correction algorithms.

The corrections to the Stokes parameters given by (A4.3)-(A4.4) can be incorporated directly into the elements of the polarimetric gain matrix and offset vectors.

Define G and O as the gain matrix and offset vector of the RUT prior to correction, and G' and O' as the same after correction. Using (A4.3), they are related by

$$[G \mid O] = [G' \mid O'] \cdot \begin{bmatrix} 1 & 0 & 0 & 0 & T_{ex,v} \\ 0 & 1 & 0 & 0 & T_{ex,h} \\ 2\,\mathrm{Re}\{S_{hv}^* S_{11,rad,v}^*\} & 2\,\mathrm{Re}\{S_{vh} S_{11,rad,h}\} & 1 & 0 & T_{ex,3} \\ 2\,\mathrm{Im}\{S_{hv}^* S_{11,rad,v}^*\} & 2\,\mathrm{Im}\{S_{vh} S_{11,rad,h}\} & 0 & 1 & T_{ex,4} \\ 0 & 0 & 0 & 0 & 1 \end{bmatrix} \tag{A4.5}$$

Solving for the corrected values, G' and O', gives

$$[G' \mid O'] = [G \mid O] \cdot \begin{bmatrix} 1 & 0 & 0 & 0 & T_{ex,v} \\ 0 & 1 & 0 & 0 & T_{ex,h} \\ 2\,\mathrm{Re}\{S_{hv}^* S_{11,rad,v}^*\} & 2\,\mathrm{Re}\{S_{vh} S_{11,rad,h}\} & 1 & 0 & T_{ex,3} \\ 2\,\mathrm{Im}\{S_{hv}^* S_{11,rad,v}^*\} & 2\,\mathrm{Im}\{S_{vh} S_{11,rad,h}\} & 0 & 1 & T_{ex,4} \\ 0 & 0 & 0 & 0 & 1 \end{bmatrix}^{-1} \tag{A4.6}$$

Eqn. (A4.6) is the general expression for corrections to the gain matrix and offset vector. A simplified special case applies for the CNCS because the isolation between its v- and h-pol channels is extremely high (~ 75 dB). In this case, S_{hv} and S_{vh} can be assumed equal to zero. The corrections given in (A4.6) then simplify to

$$[G' \mid O'] = [G \mid O] \cdot \begin{bmatrix} 1 & 0 & 0 & 0 & -|S_{vv}|^2 T_{r,v} - 2\,\mathrm{Re}\{S_{vv} T_{c,v}\} \\ 0 & 1 & 0 & 0 & -|S_{hh}|^2 T_{r,h} - 2\,\mathrm{Re}\{S_{hh} T_{c,h}\} \\ 0 & 0 & 1 & 0 & 0 \\ 0 & 0 & 0 & 1 & 0 \\ 0 & 0 & 0 & 0 & 1 \end{bmatrix} \tag{A4.7}$$

Eqn. (A4.7) demonstrates that the RUT polarimetric gain matrix is unaffected by impedance mismatches, provided isolation between the v- and h-pol channels is high. Only the offset vector is affected. Note that the gain matrix and offset vector would need to be corrected again using the impedance and cross-talk characteristics of the antenna when it is attached to the RUT instead.

References

[1] W. D. Hart, S. P. Palm, D. L. Hlavka, and J. D. Spinhirne, "Global and polar cloud cover from the Geoscience Laser Altimeter System, observations and implications," in *12th Conference on Atmospheric Radiation, AMS*. Madison, 2006.

[2] A. P. Cracknell and L. W. B. Hayes, *Introduction to remote sensing*. New York: Taylor & Francis, 1991.

[3] F. T. Ulaby, R. K. Moore, and A. K. Fung, *Microwave remote sensing: active and passive. Volumn I, Microwave Remote Sensing Fundamentals and Radiometry*. Reading, Mass.: Addison-Wesley Pub. Co., Advanced Book Program/World Science Division, 1981.

[4] F. J. Wentz, "Measurement of oceanic wind vector using satellite microwave radiometers," *Geoscience and Remote Sensing, IEEE Transactions on*, vol. 30, no. 5, pp. 960, 1992.

[5] S. T. Brown, C. S. Ruf, and D. R. Lyzenga, "An emissivity-based wind vector retrieval algorithm for the WindSat polarimetric radiometer," *Geoscience and Remote Sensing, IEEE Transactions on*, vol. 44, no. 3, pp. 611, 2006.

[6] G. W. Petty, *A First Course in Atmoshpheric Radiation*. Madison, Wisconsin: Sundog Publishing, 2004.

[7] F. T. Ulaby, *Fundamentals of applied electromagnetics*, 1999 ed. Upper Saddle River, N.J.: Prentice Hall, 1999.

[8] J. A. Kong, *Electromagnetic wave theory*. Cambridge, MA: EMW Pub., 2000.

[9] A. Stogryn, "The microwave permittivity of sea and fresh water," *1995, GenCorp Aerojet: Azusa, CA*, no.

[10] W. H. Peake, "Interaction of Electromagnetic Waves with Some Natural Surfaces," *IRE Trans.*, vol. AP-7, pp. 5342, 1959.

[11] J. D. Kraus, *Radio Astronomy*. Powell, Ohio: Cygnus-Quasar, 1982.

[12] L. Tsang, J. A. Kong, and R. T. Shin, *Theory of Microwave Remote Sensing*: John Wiley & Sons, 1985.

[13] A. Stogryn, "The emissivity of sea foam at microwave frequencies," presented at Antennas and Propagation Society International Symposium, 1971.

[14] P. M. Smith, "The emissivity of sea foam at 19 and 37 GHz," *IEEE Transactions on Geoscience and Remote Sensing*, vol. 26, no. 5, pp. 541, 1988.

[15] S. H. Yueh, W. J. Wilson, F. K. Li, S. V. Nghiem, and W. B. Ricketts, "Polarimetric brightness temperatures of sea surfaces measured with aircraft K- and Ka-band radiometers," *Geoscience and Remote Sensing, IEEE Transactions on*, vol. 35, no. 5, pp. 1177-1187, 1997.

[16] S. H. Yueh, W. J. Wilson, F. K. Li, S. V. Nghiem, and W. B. Ricketts, "Polarimetric measurements of sea surface brightness temperatures using an aircraft K-band radiometer," *Geoscience and Remote Sensing, IEEE Transactions on*, vol. 33, no. 1, pp. 85-92, 1995.

[17] S. H. Yueh, W. J. Wilson, S. J. Dinardo, and F. K. Li, "Polarimetric microwave brightness signatures of ocean wind directions," *Geoscience and Remote Sensing, IEEE Transactions on*, vol. 37, no. 2, pp. 949-959, 1999.

[18] S. H. Yueh, R. Kwok, F. K. Li, S. V. Nghiem, and W. J. Wilson, "Polarimetric passive remote sensing of ocean wind vectors," *Radio Science*, vol. 29, no. 4, pp. 799-814, 1994.

[19] S. H. Yueh, "Estimates of Faraday rotation with passive microwave polarimetry for microwave remote sensing of Earth surfaces," *Geoscience and Remote Sensing, IEEE Transactions on*, vol. 38, no. 5, pp. 2434, 2000.

[20] "www.adlerplanetarium.org/cyberspace/planets/earth/images/atmosphere01.jpg."

[21] M. Tiuri, "Radio astronomy receivers," *Antennas and Propagation, IEEE Transactions on*, vol. 12, no. 7, pp. 930, 1964.

[22] M. A. Fischman and A. W. England, "An L-band direct sampling digital radiometer for STAR technology sensors," presented at 2000 IEEE Aerospace Conference Proceedings, Big Sky, MT, 2000.

[23] A. Brown and B. Wolt, "Digital L-band receiver architecture with direct RF sampling," Las Vegas, NV, USA, 1994.

[24] A. Parssinen, R. Magoon, S. I. Long, and V. Porra, "A 2-GHz subharmonic sampler for signal downconversion," *IEEE Transactions on Microwave Theory and Techniques*, vol. 45, no. 12 pt 2, pp. 2344, 1997.

[25] E. Njoku, J. Stacey, and F. Barath, "The Seasat scanning multichannel microwave radiometer (SMMR): Instrument description and performance," *Oceanic Engineering, IEEE Journal of*, vol. 5, no. 2, pp. 100-115, 1980.

[26] C. S. Ruf and C. T. Swift, "Atmospheric profiling of water vapor density with a 20.5-23.5 GHz autocorrelation radiometer," *Journal of Atmospheric and Oceanic Technology*, vol. 5, no. 4, pp. 539-546, Aug. 1988.

[27] P. W. Gaiser, "WindSat-satellite-based polarimetric microwave radiometer," 1999.

[28] A. Ishimaru, *Electromagnetic Wave Propagation, Radiation, and Scattering*: Prentice-Hall, Englewood Cliffs, NJ, 1991.

[29] C. S. Ruf, "Constraints on the polarization purity of a Stokes microwave radiometer," *Radio Science*, vol. 33, no. 6, pp. 1617-1639, 1998.

[30] J. Lahtinen, J. Pihlflyckt, I. Mononen, S. J. Tauriainen, M. Kemppinen, and M. T. Hallikainen, "Fully polarimetric microwave radiometer for remote sensing," *Geoscience and Remote Sensing, IEEE Transactions on*, vol. 41, no. 8, pp. 1869, 2003.

[31] J. R. Piepmeier, "Calibration of passive microwave polarimeters that use hybrid coupler-based correlators," *Geoscience and Remote Sensing, IEEE Transactions on*, vol. 42, no. 2, pp. 391, 2004.

[32] L. Klein and C. Swift, "An improved model for the dielectric constant of sea water at microwave frequencies," *Antennas and Propagation, IEEE Transactions on [legacy, pre - 1988]*, vol. 25, no. 1, pp. 104-111, 1977.

[33] F. T. Ulaby, R. K. Moore, and A. K. Fung, *Microwave remote sensing: active and passive. Volumn III, From Theory to Application*. Reading, Mass.: Addison-Wesley Pub. Co., Advanced Book Program/World Science Division, 1981.

[34] S. H. Yueh, R. West, W. J. Wilson, F. K. Li, E. G. Njoku, and Y. Rahmat-Samii, "Error sources and feasibility for microwave remote sensing of ocean surface salinity," *Geoscience and Remote Sensing, IEEE Transactions on*, vol. 39, no. 5, pp. 1049, 2001.

[35] C. S. Ruf, "Vicarious calibration of an ocean salinity radiometer from low earth orbit," *Journal of Atmospheric and Oceanic Technology*, vol. 20, no. 11, pp. 1656-1670, 2003.

[36] D. M. Le Vine and S. Abraham, "The effect of the ionosphere on remote sensing of sea surface salinity from space: absorption and emission at L band," *Geoscience and Remote Sensing, IEEE Transactions on*, vol. 40, no. 4, pp. 771, 2002.

[37] E. J. M. Rignot, "Effect of Faraday rotation on L-band interferometric and polarimetric synthetic-aperture radar data," *Geoscience and Remote Sensing, IEEE Transactions on*, vol. 38, no. 1, pp. 383, 2000.

[38] S. Ribo and M. Martin-Neira, "Faraday rotation correction in the polarimetric mode of MIRAS," *Geoscience and Remote Sensing, IEEE Transactions on*, vol. 42, no. 7, pp. 1405, 2004.

[39] P. Waldteufel, P. Waldteufel, N. Floury, E. P. Dinnat, and G. A. C. G. Caudal, "Ionospheric effects for L-band 2-D interferometric radiometry," *Geoscience and Remote Sensing, IEEE Transactions on*, vol. 42, no. 1, pp. 105, 2004.

[40] N. Skou, "Faraday rotation and L band oceanographic measurements," *Radio Science*, vol. 38, no. 4, pp. 8059, 2003.

[41] D. Hudson, J. R. Piepmeier, and D. G. Long, "Polarization Rotation Correction in Radiometry: An Error Analysis," *Geoscience and Remote Sensing, IEEE Transactions on*, vol. 45, no. 10, pp. 3212, 2007.

[42] A. B. Tanner, "Development of a high-stability water vapor radiometer," *Radio Science*, vol. 33, no. 2, pp. 449-462, 1998.

[43] G. Evans and C. W. McLeish, *RF Radiometer Handbook*. Dedham, MA: Artech House, 1977.

[44] S. T. Brown and C. S. Ruf, "Determination of an Amazon hot reference target for the on-orbit calibration of microwave radiometers," *Journal of Atmospheric and Oceanic Technology*, vol. 22, no. 9, pp. 1340, 2005.

[45] P. W. Gaiser, K. M. St Germain, E. M. Twarog, G. A. Poe, W. Purdy, D. Richardson, W. Grossman, W. L. Jones, D. Spencer, G. Golba, J. Cleveland, L. Choy, R. M. Bevilacqua, and P. S. Chang, "The WindSat spaceborne polarimetric microwave radiometer: sensor description and early orbit performance," *IEEE Transactions on Geoscience and Remote Sensing*, vol. 42, no. 11, pp. 2347, 2004.

[46] C. S. Ruf, Y. Hu, and S. T. Brown, "Calibration of WindSat polarimetric channels with a vicarious cold reference," *Geoscience and Remote Sensing, IEEE Transactions on*, vol. 44, no. 3, pp. 470, 2006.

[47] C. S. Ruf, "Detection of calibration drifts in spaceborne microwave radiometers using a vicarious cold reference," *IEEE Transactions on Geoscience and Remote Sensing*, vol. 38, no. 1 I, pp. 44, 2000.

[48] A. J. Gasiewski and D. B. Kunkee, "Calibration and applications of polarization-correlating radiometers," *Microwave Theory and Techniques, IEEE Transactions on*, vol. 41, no. 5, pp. 767, 1993.

[49] J. Lahtinen and M. T. Hallikainen, "HUT fully polarimetric calibration standard for microwave radiometry," *Geoscience and Remote Sensing, IEEE Transactions on*, vol. 41, no. 3, pp. 603, 2003.

[50] J. Lahtinen, A. J. Gasiewski, M. Klein, and I. S. Corbella, "A calibration method for fully polarimetric microwave radiometers," *Geoscience and Remote Sensing, IEEE Transactions on*, vol. 41, no. 3, pp. 588, 2003.

[51] C. S. Ruf and J. Li, "A correlated noise calibration standard for interferometric, polarimetric, and autocorrelation microwave radiometers," *Geoscience and Remote Sensing, IEEE Transactions on*, vol. 41, no. 10, pp. 2187, 2003.

[52] C. S. Ruf and J. Li, "Evaluation of Correlation Radiometers using Programmable Correlated Noise," presented at Proc. of the Second International Microwave Radiometer Calibration Workshop, Barcelona, Spain, 2002.

[53] C. Ruf, C. Principe, T. Dod, B. Gosselin, B. Monosmith, S. Musko, S. Rogacki, A. Stewart, and Z. Zhaonan, "Lightweight rainfall radiometer STAR aircraft sensor," presented at Geoscience and Remote Sensing Symposium, 2002. IGARSS '02. 2002 IEEE International, 2002.

[54] F. Pellerano, J. Piepmeier, M. Triesky, K. Horgan, J. Forgione, J. Caldwell, W. Wilson, S. Yueh, M. Spencer, D. McWatters, and A. Freedman, "The Aquarius Ocean Salinity Mission High Stability L-band Radiometer," presented at IEEE International Conf. Geosci. Remote Sens. Symposium, Denver, 2006.

[55] C. S. Ruf, S. T. Brown, Y. Hu, and H. Kawakubo, "WindSat calibration and geophysical parameter estimation," presented at IEEE International Geosci. Remote Sens. Symposium, Anchorage, AK, 2004.

[56] T. Y. Otoshi, "The Effect of Mismatched Components on Microwave Noise-Temperature Calibrations," *Microwave Theory and Techniques, IEEE Transactions on*, vol. 16, no. 9, pp. 675, 1968.

[57] I. Corbella, A. Camps, F. Torres, and J. Bara, "Analysis of noise-injection networks for interferometric-radiometer calibration," *Microwave Theory and Techniques, IEEE Transactions on*, vol. 48, no. 4, pp. 545-552, 2000.

[58] I. Corbella, F. Torres, A. Camps, N. Duffo, M. Vall-llossera, K. Rautiainen, M. Martin-Neira, and A. Colliander, "Analysis of correlation and total power radiometer front-ends using noise waves," *Geoscience and Remote Sensing, IEEE Transactions on*, vol. 43, no. 11, pp. 2452, 2005.

[59] I. Corbella, F. Torres, A. Camps, N. Duffo, M. Vall-llossera, K. Rautiainen, and A. Colliander, "Systematic noise analysis of a correlation radiometer front-end," 2004.

[60] V. S. Reinhardt, Y. C. Shih, P. A. Toth, S. C. Reynolds, and A. L. Berman, "Methods for measuring the power linearity of microwave detectors for radiometric applications," *IEEE Transactions on Microwave Theory and Techniques*, vol. 43, no. 4 pt 1, pp. 715, 1995.

[61] N. Skou, "Microwave radiometer linearity measured by simple means," presented at Geoscience and Remote Sensing Symposium, 2002. IGARSS '02. 2002 IEEE International, 2002.

[62] F. A. Pellerano, W. J. Wilson, and A. B. Tanner, "Development of a high stability L-band radiometer for the Aquarius ocean salinity mission," *Proceedings of the SPIE*, vol. 5978, pp. 143-150, 2005.

[63] C. S. Ruf, C. T. Swift, A. B. Tanner, and D. M. Le Vine, "Interferometric synthetic aperture microwave radiometry for the remote sensing of the Earth," *Geoscience and Remote Sensing, IEEE Transactions on*, vol. 26, no. 5, pp. 597-611, 1988.

[64] J. Peng and C. Ruf, "Covariance Statistics of Polarimetric Brightness Temperature Measurements," *IEEE Transactions on Geoscience and Remote Sensing*, vol. In press, no., 2007.

[65] J. R. Piepmeier and A. J. Gasiewski, "Digital correlation microwave polarimetry: analysis and demonstration," *Geoscience and Remote Sensing, IEEE Transactions on*, vol. 39, no. 11, pp. 2392-2410, 2001.

[66] R. D. De Roo, C. S. Ruf, and K. Sabet, "An L-band Radio Frequency Interference (RFI) detection and mitigation testbed for microwave radiometry," presented at P2007 IEEE International Geoscience and Remote Sensing Symposium, Barcelona, Spain, 2008.

[67] R. De Roo, C. Ruf, B. Lim, L. van Nieuwstadt, C. Wineland, and R. Gandhi, "L-band and K-band Correlated Noise Calibration System (CNCS) Architecture," *2006 Specialist Meeting on Microwave Radiometry*, San Juan, PR, 2006.

[68] B. Lim and C. Ruf, "Calibration of a Fully Polarimetric Microwave Radiometer Using a Digital Polarimeric Noise Source," presented at Proc. 2006 IEEE International Geoscience and Remote Sensing Symposium, Denver, CO, 2006.

[69] J. Peng and C. Ruf, "Calibration Method for Fully Polarimetric Microwave Radiometers Using the Correlated Noise Calibration Standard," *IEEE Transactions on Geoscience and Remote Sensing*, accepted 46(10), 2008.

[70] C. Ruf and J. Peng, "Digital Noise Calibration Standard," presented at Juno MWR Science Team Meeting, Southwest Research Institute, San Antonio, TX 2 Oct 2006.

[71] J. Peng, C. Ruf, S. Brown, and J. Piepmeier, "Characterization of the Aquarius and Juno Radiometers Using a Programmable Digital Noise Source," presented at Proc. 2007 IEEE International Geoscience and Remote Sensing Symposium, Barcelona, SPAIN, 2007.

[72] R. H. Frater and D. R. Williams, "An Active "Cold" Noise Source," *Microwave Theory and Techniques, IEEE Transactions on*, vol. 29, no. 4, pp. 344, 1981.

[73] C. S. Ruf, S. M. Gross, and S. Misra, "RFI detection and mitigation for microwave radiometry with an agile digital detector," *IEEE Transactions on Geoscience and Remote Sensing*, vol. 44, no. 3, pp. 694, 2006.

[74] R. Schieder, G. Rau, and B. Vowinkel, "Characterization and measurement of radiometer stability," presented at Proc. 14 thEuropean Microwave Conference, 1984.

[75] R. Grammier, "An Overview of the Juno Mission to Jupiter," ISTS 2006-o-2-06V, 2006.

[76] C. A. Balanis, *Antenna theory: analysis and design*, 2nd ed. New York: Wiley, 1997.